

Anisotropic Reinforcement Following Myocardial Infarction

A Dissertation

Presented to
the faculty of the School of Engineering and Applied Science
University of Virginia

in partial fulfillment
of the requirements for the degree

Doctor of Philosophy

by

Samantha Ann Clarke

August

2015

APPROVAL SHEET

The dissertation
is submitted in partial fulfillments of the requirements
for the degree of

Doctor of Philosophy



AUTHOR

The dissertation has been read and approved by the examining committee:

Jeffrey Holmes

Advisor

Frederick Epstein

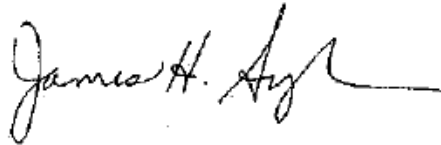
Silvia Blemker

Jeffrey Saucerman

Gorav Ailawadi

Ravi Ghanta

Accepted for the School of Engineering and Applied Science:



Dean, School of Engineering and Applied Science

August
2015

Abstract

Every 34 seconds, an American has a heart attack, or myocardial infarction (MI). Acutely, loss of muscle contraction leads to passive stretching of the infarct throughout the entire cardiac cycle, reducing the pumping capacity of the ventricle. In the long term, chronic hemodynamic changes can lead to pathological ventricular remodeling and heart failure, especially after a large MI. In an effort to prevent remodeling and progression to heart failure, numerous studies have explored the utility of mechanical restraint of the infarct or ventricle to limit post-MI ventricular dilation. Studies of both local and global reinforcement approaches have found that isotropic restraint (stiffening the infarct or ventricle similarly in all directions) can be used to reduce post-MI ventricular remodeling. However, both experimental and computational studies have failed to show improvements in acute, post-MI ventricular function with reinforcement. This dissertation explores the use of an optimized, local reinforcement strategy to determine its effects on both acute post-MI function and chronic ventricular remodeling.

A finite element model of the canine heart was used to predict the reinforcement approach that optimized acute, post-MI function: selective, anisotropic reinforcement in the longitudinal (apex-base) direction. We tested this model prediction in a canine model of acute MI, using an epicardial patch to generate longitudinal restraint of the infarct region. Unlike isotropic strategies, anisotropic reinforcement of the acute infarct led to immediate recovery of over 50% of the functional deficit in cardiac output caused by infarction. Using the same animal model and reinforcement approach, we then conducted a chronic trial to determine whether these acute improvements in function would translate into improvement in chronic function or attenuation of left ventricular (LV) dilation. Somewhat surprisingly, we did not observe any differences in global LV function, LV remodeling, or infarct scar structure at the conclusion of our 8-week chronic study. We hypothesized that dramatic compaction of the infarct scar during healing mechanically unloaded the tension in the epicardial patch, so that scars were no longer experiencing any restraint by 8 weeks post-MI.

We constructed a new finite element model of the canine left ventricle to examine the relationship between infarct restraint, scar compaction, and left ventricular function. We incorporated infarct remodeling by simulating varying degrees of longitudinal compaction, along with isotropic stiffening of the scar. Higher degrees of longitudinal scar compaction produced larger decreases in end-diastolic and end-systolic volume, although predicted stroke volumes across all chronic reinforcement models were similar. Consistent with our experimental hypothesis, end-systolic longitudinal stresses in the center of the patch transitioned from tensile to compressive with increasing magnitudes of scar compaction. This model forms a new foundation for the *in silico* evaluation of both acute and chronic effects of post-MI restraint therapies.

Acknowledgements

I would like to start by thanking my thesis advisor, Dr. Jeff Holmes, for his seemingly limitless patience over the last five years. I couldn't have asked for a better teacher or more dedicated mentor. Thank you for your guidance and encouragement through stressful days, and for not letting me give up when I wanted to. Thank you for your frequent troubleshooting, thoughtful advice, and research wisdom, which helped make this project possible. Your expertise and enthusiasm for research have been an inspiration, and I will always be grateful for being given the opportunity to work in your lab. Thank you also to Dr. Eric Kennedy, who first taught me about research and how to have fun while doing it.

Thank you to my dissertation committee, Dr. Fred Epstein, Dr. Gorav Ailawadi, Dr. Silvia Blemker, Dr. Jeff Saucerman, and Dr. Ravi Ghanta for your thoughtful feedback and advice throughout the duration of this project. A special thank you to Dr. Ailawadi, for his dedication to the patch project and attendance at every patch surgery.

Thank you to the surgery team, Craig Goodman, Jeremy Gatesman, and Emily Downs. Your expertise made the experiments go smoothly, and your companionship made them go quickly. Thank you for all of the laughs, advice, baked goods, and musical education.

A special thank you to all past and present members of the UVA Cardiac Biomechanics Group, especially Dr. Will Richardson, Dr. Colleen Witzenburg, Ana Estrada, Kellen Chen, Laura Caggiano, TK Phung, Dr. Katy Parker, Dr. Christian Moyer, Dr. Beth Ames, Dr. Andrew Rouillard, Tracy Burcin, and Dr. Greg Fomovsky. Your thoughtful ideas and suggestions at every step of the way have contributed significantly to improving the quality of this work. Even more importantly, your conversation and friendship through the years have been a source of optimism and joy through the ups and downs of research. I would also like to thank the undergraduate students Kevin Foley, Kaila Grenier, Wade Zhang, and Jesse Macadangdang whose work contributed to the completion of this dissertation.

Finally, I would like to thank my friends and family for their unwavering love and support. To my parents, John and Ann Marie, for encouraging my determination since the day I learned to walk, and my sister, Nicole, for tolerating that stubbornness later. You have been my best cheerleaders through twenty-two years of school. To my husband Andrew, for celebrating with me, commiserating with me, and drinking with me. Thank you for the daily encouragement and all of the coffee dates, which fueled most of this dissertation. Finally, to my daughter, Annemarie, for giving me perspective on what it means to be successful, inspiring me to do my best, and teaching me how to get more work done on less sleep than ever before.

Table of Contents

Abstract.....	i
Acknowledgements	iii
List of Tables	ix
List of Figures	xi
List of Abbreviations	xx

Chapter 1

The Mechanics of Myocardial Infarction and Postinfarction Restraint	1
The cardiac cycle.....	2
Mechanics of myocardial infarction	3
Metrics for measuring changes in LV function.....	6
Mechanical reinforcement of the infarcted left ventricle.....	8
Bi-ventricular restraint.....	10
Acorn CorCap.....	10
Paracor HeartNet	13
Left ventricular restraint	14
Myocor Coapsys (Myosplint).....	14
CardioClasp	15
Optimized global restraint.....	16
Global restraint limits dilation	19
Limitations of whole ventricle restraint.....	21
Local restraint	21

Synthetic patches.....	22
Cell seeded and tissue engineered patches	27
Local restraint limits dilation.....	30
Limitations of patch restraint	33
Conclusion.....	33
References.....	34

Chapter 2

Acute, Anisotropic Reinforcement of Left Ventricular Infarcts	40
Finite element modeling of infarct stiffening.....	41
Optimizing local restraint	44
Methods to test acute longitudinal infarct reinforcement <i>in vivo</i>	46
Methods to analyze hemodynamics.....	50
Methods to analyze regional deformation.....	51
Results	52
Discussion.....	60
Conclusion.....	61
References.....	62

Chapter 3

Chronic, Anisotropic Reinforcement of Left Ventricular Infarcts	63
Post-MI function and remodeling.....	64
Methods to test chronic, longitudinal infarct reinforcement <i>in vivo</i>	64
Methods to measure myocyte size in the remote myocardium	66
Methods to measure collagen content and alignment in scar	68
Methods to analyze magnetic resonance images.....	68
Methods to analyze LV hemodynamics.....	72
Methods to analyze myocyte size and scar structure	72
Results	75
Discussion.....	86
Conclusion.....	91
References.....	92

Chapter 4

Effects of Sample Heterogeneity on Biaxially Measured Material Properties	96
Theory of plane stress analysis in biaxial testing	97
Sample preparation and biaxial test setup	98
Model geometry & material properties.....	103
Loading & boundary conditions	103
Mesh refinement study.....	107
Models to examine the effects of scar distribution	109
Models to examine the effects of scar size	111
Results: Scar distribution.....	113
Results: Scar size.....	115
Discussion.....	120
Conclusion.....	122
References.....	124

Chapter 5

Finite Element Model of Left Ventricular Infarct Restraint	125
Left ventricular geometry	126
Muscle material properties	129
Mesh refinement study.....	132
Acute infarct & patch material properties	136
Chronic scar material properties.....	140
Scar compaction.....	143
Boundary conditions & loading.....	144
Results: Local deformation	144
Results: Global function	147
Discussion.....	150
Conclusion.....	151
References.....	152

Chapter 6

Acute, Anisotropic Reinforcement for Acute Right Ventricular Failure	153
Right ventricular failure	154
Methods for generating right ventricular failure	155

Methods for data analysis	161
Results: Local deformation	161
Results: Global function	166
Discussion.....	168
References.....	169

Chapter 7

Implications & Future Directions	170
Summary of main contributions	170
Interplay between scar compaction and restraint efficacy	171
Effect of mechanical environment on scar remodeling	172
Finite element simulation of infarct remodeling	174
Multiscale modeling of infarct healing	175
References.....	177

List of Tables

Table 1.1 Summary of ventricular restraint device studies

HF = heart failure, EDV = end-diastolic volume, ESV = end-systolic volume, EF = ejection fraction, SV = stroke volume, CO = cardiac output, FS = fractional shortening, FAS = fractional area shortening, FAC = fractional area of contraction, WT = wall thickening, RS = radial strain, dP/dt = rate of systolic pressure generation, ESPVR (ESPAR, ESPSLR) = slope of the end-systolic pressure-volume (pressure-area, pressure-segment length) relationship, BZ = borderzone, CSA = cross-sectional area, LAD = left anterior descending coronary artery, FEM = finite element model, QVR = quantitative ventricular restraint, AMVR = adjustable and measureable ventricular restraint 20

Table 1.2 Summary of local reinforcement studies

LCx = left circumflex coronary artery, EDD = end-diastolic diameter, ESD = end-systolic diameter, PP = polypropylene, PEUU = polyester urethane urea, PTFE = polytetrafluoroethylene, MSC = mesenchymal stem cells, PLGA = poly(lactic-co-glycolic) acid, EHTG = engineered heart tissue graft, PGCL = poly(glycolide-co-caprolactone), PU = polyurethane, MyoB = myoblasts, See Table 1 caption for list of other relevant abbreviations. * indicates a significant difference from control in the seeded patch or viable construct group only, no symbol indicates a significant difference from control in all patch groups (seeded + unseeded/viable + non-viable)..... 32

Table 2.1 Hemodynamics

Hemodynamic data from 10 dogs that showed a shift in cardiac output curve 45 minutes after coronary ligation. Dogs were pretreated with propranolol and atropine to prevent reflex changes in heart rate and intrinsic myocardial contractility and LAD occlusion; by design, end-systolic pressure (ESP), heart rate (HR), and maximum dP/dt did not vary significantly during the experiment. During Ischemia, animals compensated for reduced systolic function via the Frank-Starling mechanism, increasing end-diastolic pressure (EDP) and volume (EDV) to maintain stroke volume (SV) and cardiac output (CO) despite increased end-systolic volume (ESV). Anisotropic surgical reinforcement significantly reduced EDV and ESV. *Midwall volumes include cavity volume and approximately half the LV wall volume. †P<0.001 vs. baseline; ‡P<0.001 vs. ischemia 53

Table 3.1 Summary of Experimental Groups

Experimental group size and average weight at surgery were similar between patch and control groups. Most importantly, initial infarct size did not differ between the two groups, ensuring that any differences observed between groups were not due to differences in the initial infarct size. Final body, LV, and heart mass were all similar between groups as well, suggesting there were no dramatic differences in LV remodeling (p=NS for all comparisons)..... 77

List of Figures

- Figure 1.1** A myocardial infarction (MI) occurs when a coronary artery, here the left anterior descending (LAD) artery (marked by the black arrow), becomes occluded, leaving the myocardium normally perfused by that vessel (shaded in light gray) without blood supply. Adapted from Sobotta 1907 4
- Figure 1.2** Changes in (A) end-diastolic and (B) end-systolic LV volumes following post-infarction CorCap reinforcement. Volumes at the final time point for the CorCap (CSD) and control groups are represented as the percent increase from the pre-MI baseline value. Created with data from Blom et al. 2005, 2007 and Pilla et al. 2005 12
- Figure 1.3** Acute hemodynamic changes with increasing levels of passive restraint. Created with data from Ghanta et al. 2007..... 18
- Figure 1.4** Changes in LV (A) end-diastolic and (B) end-systolic volumes following local patch reinforcement. Dotted lines indicate changes in the control group, solid lines indicate changes in the patch reinforcement group. Created with data from Kelley et al. 1999, Moainie et al. 2002, and Liao et al. 2010 24
- Figure 1.5** Effects of local infarct reinforcement in rats. Comparison of compliance in normal myocardium, polyester urethane urea patched infarcts, and unpatched infarcts

in the **(A)** circumferential and **(B)** longitudinal directions (replotted from Fujimoto et al. 2007). **(C)** Pressure-volume loops following infarction and reinforcement with a viable engineered heart tissue patch (replotted from Zimmermann et al. 2006) 26

Figure 2.1 Computationally generated **(A)** LV function curves and **(B)** pressure-volume curves for normal myocardium and three stages of infarct healing. P-V analysis shows dramatic shifts in the ESPVRs of immediate and acute infarcts, with minimal changes in the EDPVRs. Chronic scars exhibited a leftward shift in the ESPVR accompanied by an increase in the slope of the EDPVR. These shifts led to minimal net change in LV function, as all infarct models showed similar functional depression compared to the baseline model. Normalized volumes are relative to the initial reference volume in the simulation. Recreated with data from Bogen et al. 1980 43

Figure 2.2 Predicted stroke volume from a finite element model of a canine heart. SV (in ml) in the acute LV infarct model dropped to 7.6 ml (from 15.7 ml at baseline). Plotted are predicted values of SV for varying combinations of circumferential and longitudinal infarct stiffness. SV is maximized in the area of low circumferential and high longitudinal stiffness (near the top left corner). The dotted white line represents an isotropic increase in infarct stiffness, along which minimal improvement in SV is observed. Recreated with data from Fomovsky et al. 2011 45

Figure 2.3 Schematic of infarct reinforcement. **(A)** Sonomicrometer crystals were placed on the anterior wall in the anticipated region of LAD infarction. The patch was applied to epicardium of the infarct using a running suture along all four edges. **(B)** Isotropic and **(C)** anisotropic patches were both applied under as much longitudinal tension as possible. Diagram from Fomovsky 2010..... 49

Figure 2.4 Changes in infarct segment lengths with patch reinforcement in one animal. Regardless of patch material properties, longitudinal tension resulted in a decrease in **(A)** longitudinal segment lengths with minimal effects on **(B)** circumferential segments 55

Figure 2.5 **(A)** Remodeling strains reflecting changes in end-diastolic infarct dimensions relative to baseline show acute infarct expansion in both directions.

Longitudinal restraint with both patch types reduces segment lengths in the longitudinal dimension to shorter than at baseline. **(B)** Systolic strains, calculated between ED and ES, are negative at baseline (reflecting active shortening) and become positive in ischemia (passive stretching). Patch application caused a slight increase in circumferential stretching but no change in the longitudinal direction. * $p < 0.05$ v. baseline, ** $p < 0.001$ v. baseline, † $p < 0.05$ v. ischemia, ‡ $p < 0.001$ v. ischemia 56

Figure 2.6 **(A)** The average ESPVR showed a large rightward shift between baseline and ischemia, as expected. Application of either patch shifted the active curve leftward toward the baseline curve, with minimal effects on the passive curve. **(B)** Interpolating changes in volumes at matched EDP and ESP, however, did reveal decreases in both EDV and ESV (dotted blue lines in (A)) with both patch types. * $p < 0.05$ v. baseline, † $p < 0.05$ v. ischemia 58

Figure 2.7 **(A)** Starling curves comparing LV function across states. The curve shifts right between baseline and ischemia (a higher pressure is needed to generate the same CO) and then leftward back towards baseline with reinforcement. **(B)** Interpolated CO (at the baseline EDP of each animal) decreased in ischemia and then increased in both patch conditions, although only CO with the anisotropic patch was significantly greater than ischemia. ** $p < 0.001$ v. baseline, † $p < 0.05$ v. ischemia..... 59

Figure 3.1 Sectioning planes to examine myocyte length and cross-sectional area. A sectioning plane approximately parallel to the base (orange) was used to measure cell length, and a transmural section used to measure CSA. Although myocyte orientation varies transmurally (not shown), these sectioning planes ensured that at least part of the section (near the midwall) contained myocytes either parallel or perpendicular to the plane..... 67

Figure 3.2 Cavity and wall volume adjustments made at the apex and base. “True” base (purple) and apex (orange + green) were selected on a LA image. Cavity and wall volume was added at the base by multiplying the areas of the basal slice by the thickness of the fractional slice between the base point and the top of the stack. Volume was added at the apex assuming a conical tapering of the LV, using the endocardial

distance (orange point) to adjust the cavity volume and the epicardial distance (green point) to adjust the wall volume..... 71

Figure 3.3 Analysis of scar structure. **(A)** A grid of non-overlapping imaging fields was overlaid on each section, and 10 collagenous fields were selected at random for imaging and analysis. **(B)** Circularly polarized and bright field (not shown) images were subtracted and **(C)** thresholded to isolate collagen pixels. **(D)** A modified Fiber3 algorithm was applied to the thresholded images to determine the distribution of collagen alignment..... 74

Figure 3.4 8 week survival curves in animals initially randomized to patch application or untreated control group. An apparent trend towards higher survival in the patch group was not statistically significant ($p=0.3$ by logrank test)..... 76

Figure 3.5 Left ventricular remodeling. **(A)** End-diastolic and **(B)** end-systolic volumes were significantly smaller in patch animals at 48 hours post-MI ($p<0.05$ EDV, $p<0.01$ ESV), but differences in cavity volumes faded by 8 weeks. **(C)** LV muscle volume (estimated from MRI as LV wall volume – infarct volume) was significantly greater in control animals at both time points ($p<0.05$). **(D)** Remote myocyte measurements from both groups suggested that myocytes were longer and thinner than those from an uninfarcted control animal (white bars), consistent with the observed changes in EDV. * $p<0.05$ patch v. control, † $p<0.05$, †† $p<0.001$ compared to 48 hours 79

Figure 3.6 Infarct remodeling. **(A)** Infarct volume decreased significantly in both groups over the course of the study period. **(B)** Quantification of scar compaction in each dimension revealed that scars compacted by an overall average of 39% circumferentially and 14% longitudinally; significant compaction in the radial direction was observed only in the patch group. † $p<0.01$, †† $p<0.001$ compared to 48 hour value. $p=NS$ for all comparisons between patch and control..... 81

Figure 3.7 Scar Structure. **(A)** Mean angle and **(B)** mean vector length (indicating strength of alignment, where 0=randomly oriented and 1=perfectly aligned) of collagen fibers measured at 5 transmural depths. In control animals, the mean orientation of collagen fibers mimics the transmural distribution of muscle fiber angles, and strength

of alignment is highest at the midwall. Patch animals exhibited a trend towards stronger circumferential fiber alignment at 25% depth, with apparent differences fading with increasing distance away from the epicardium. $p=NS$ between patch and control for mean angle and mean vector length at every transmural depth. **(C)** Collagen area fraction at each depth and **(D)** infarct wall thickness were also similar between groups, leading to no differences in total scar collagen volume fraction 83

Figure 3.8 Hemodynamics at 8-week terminal study compared to previously unpublished data a group of 9 non-infarcted animals. **(A)** Heart rate, **(B)** end-systolic elastance, and **(C)** maximum rate of LV pressure generation at baseline (gray bars) were all significantly decreased in both patch and control groups compared to non-infarcted. A significant response to Db (black bars) was measured in all three indices in non-infarcted animals, but was only observed in the max dPdt of infarcted animals and in the heart rate of control animals. **(D)** Cardiac output (interpolated at a matched EDP of 12mmHg) was maintained across experimental groups, and only control animals exhibited an increase in CO with Db treatment. **(E)** Stroke volume (interpolated at a matched EDP of 12mmHg) was also similar among groups and did not change with Db treatment. * $p<0.01$, paired comparison to pre-Db value 85

Figure 4.1 Two patch (left) and two control (right) infarct scar biaxial test specimens, sliced in half transmurally and displayed at the midwall 101

Figure 4.2 **(A)** Infarct specimen prepared for biaxial testing and **(B)** specimen mounted in biaxial testing device 102

Figure 4.3 Diagram of model definition. Locations of applied nodal loads (normal to the corresponding edge) are shown with open white circles. Nodes in the locations marked with a red "X" were fixed in Y, nodes marked with a blue "X" were fixed in X, and a single layer of nodes at the locations marked with a green "X" were fixed in Z. Displacements of surface markers were simulated by tracking the positions of the nodes marked with closed black circles 106

Figure 4.4 Mesh refinement study. (A) Average element displacements in the x-direction in an isotropic, equibiaxially loaded scar model. (B) Percent chance in maximum displacement with each mesh refinement..... 108

Figure 4.5 Models to examine the effects of scar distribution, with scar elements in red and muscle in blue. (A) Center Scar, (B) Mid Corner Scar, (C) Corner Scar, (D) Dispersed Scar, and (E) Parallel Strips..... 110

Figure 4.6 Models to examine the effects of scar size, with scar elements in red, muscle in blue, and the central region of scar used for average stress and strain shaded in gray. (A) The 25% scar model was identical to the Center Scar model, and symmetrical reductions in scar size produced (B) 16%, (C) 9%, (D) 4%, and (E) 1% scar models..... 112

Figure 4.7 Absolute strains in each model at an equibiaxial stress of ~40kPa. Across all models, differences in strain compared to the All Scar model were less than 1%. For the subset of models in which the four-marker grid used to calculate strains did not contain any muscle elements (Center Scar, Corner Scar, Mid Corner Scar), differences in absolute strains compared to the All Scar model were less than 0.3% 114

Figure 4.8 Stress and strain in the center region of infarcts of decreasing size, averaged across elements in (A) all five transmural layers and (B) a single transmural layer on the surface..... 116

Figure 4.9 Distribution of stress (in g/cm^2 , with a scale of -10 to $600\text{g}/\text{cm}^2$ approximately corresponding to a scale of -1 to 60 kPa) in the x-direction across in the (A) 25%, (B) 9%, and (C) 1% scar models. Stress concentrations were observed at the corners of the scar region in each model 117

Figure 4.10 Distribution of stress in the z-direction (in g/cm^2 , with a scale of -200 to $60\text{g}/\text{cm}^2$ approximately corresponding to a scale of -20 to 6 kPa) in a planar cut along an edge of the scar region in the (A) 25%, (B) 9%, and (C) 1% scar models. The maximum compressive stress at the scar corners increased with decreasing scar size..... 118

Figure 4.11 Distribution of stress in the x-direction (in g/cm^2 , with a scale of -10 to 600g/cm^2 approximately corresponding to a scale of -1 to 60 kPa) in a planar cut along an edge of the scar region in the (A) 25%, (B) 9%, and (C) 1% scar models. Tensile stress in the x-direction was highest at the scar corners, in elements on the top and bottom surfaces 119

Figure 5.1 Left ventricular mesh generation. (A&B) Endo- and epicardial contour points from the SA MR images were fitted to a 16 element prolate spheroidal mesh. (C) The resulting mesh was refined in 3 dimensions and partitioned into muscle (red) and infarct (white) regions. 128

Figure 5.2 (A) Circumferential, (B) longitudinal, and (C) radial strains in a circumferential ring of elements (where 0 is the center of the infarct) for meshes of increasing element density. In all three dimensions, the magnitudes of changes in infarct and remote strains decreased with subsequent mesh refinements. Changes in in-plane strains in each region are quantified in Figure 5.3 134

Figure 5.3 (A) Circumferential and (B) longitudinal strains at the midwall in the remote, border zone, and infarct regions in meshes containing 1280, 2880, 5120, 8000, and 18000 elements. In each region, increasing element density led to slight increases in strain, with diminishing returns for each subsequent refinement 135

Figure 5.4 Infarct remodeling strains (between baseline and 45 minutes of ischemia) from the acute patch canine study (blue). Both infarct wall thinning and isotropic infarct softening computational approaches were able to replicated the acute infarct expansion data..... 139

Figure 5.5 Estimation of scar mechanical properties at 8 weeks. (A) Biaxial test data from the CP45 endocardial section was used for fitting. (B) The “All Scar” biaxial test finite element model was used to simulate multiple loading protocols and tune the scar material coefficients to match the experimental biaxial stretch response 142

Figure 5.6 Simulation of scar compaction. (A) Variable levels of prescribed longitudinal pre-stretch in the infarct led to increasing amounts of infarct compression upon equilibration. The 50% pre-stretch model was the closest match to our 8 week scar

compaction data. (B) Longitudinal stresses at end diastole and end systole in the center of the patch were tensile in the presence of an acute infarct, tensile but greatly reduced in the 10% pre-stretch model, and were compressive in both the 25% and 50% pre-stretch models..... 146

Figure 5.7 Acute function. (A) Average pressure-volume curves from the acute canine experiment (circles) compared to the model predictions (lines). (B) Comparison of experimental and computational stroke volumes, interpolated from average PV curves between EDP = 12mmHg and ESP = 85mmHg..... 148

Figure 5.8 Chronic function. Average pressure-volume curves from the chronic canine experiment (circles) compared to the model predictions (lines). Since our chronic models simulated remodeling of the scar but not of the ventricle, all chronic predictions of global pressure-volume behavior substantially underestimated left ventricular cavity volumes 149

Figure 6.1 Porcine right ventricle instrumented for acute reinforcement study 157

Figure 6.2 Patch attached to RV epicardium. Four suture lengths (marked with black arrows) were tied at opposite corners of the patch (marked "A"), and a running stitch was placed along each edge. At the other two opposite corners (marked "B"), the free ends of each suture were passed through a small length of flexible tubing. Hemostats were used to clamp down on the suture within the tubing after selective loosening or tightening of each edge, allowing us to test all three reinforcement strategies without removing the patch from the epicardium 160

Figure 6.3 Example pressure-segment length plots for a single animal (RV11), showing changes in the lengths of a segment (A) parallel and (B) perpendicular to the RV outflow tract..... 163

Figure 6.4 Average percent change in maximum segment lengths across states, relative to baseline. No significant changes were seen in the parallel segment, regardless of patch configuration, although changes in trends in this segment across states were as expected. Both isotropic and perpendicular reinforcement led to a significant reduction in the maximum perpendicular segment length. * $p < 0.01$ compared to ischemia 165

Figure 6.5 Stroke volume interpolated at the baseline EDP of each pig and averaged across animals. We observed a significant decrease in stroke volume between the baseline and ischemic states, although there were no significant differences between ischemia and any of the patch conditions. * $p < 0.01$ compared to baseline 167

List of Abbreviations

MI	Myocardial infarction
HF	Heart failure
CSD	Cardiac support device
LV	Left ventricle
RV	Right ventricle
ED	End diastole
ES	End systole
EDV	End-diastolic volume
ESV	End-systolic volume
EDP	End-diastolic pressure
ESP	End-systolic pressure
EDPVR	End-diastolic pressure-volume relationship
ESPVR	End-systolic pressure-volume relationship
LVP	Left ventricular pressure
SV	Stroke volume
CO	Cardiac output
EF	Ejection fraction
WT	Wall thickening
FAC	Fractional area of contraction
FS	Fractional shortening

dP/dt	Rate of left ventricular systolic pressure generation
Ees	End-systolic elastance
LAD	Left anterior descending coronary artery
LCx	Circumflex branch of left coronary artery
IVC	Inferior vena cava
Db	Dobutamine
PSR	Picrosirius red
MR	Magnetic resonance
SA	Short axis
LA	Long axis
CSA	Cross sectional area
FE	Finite element

Chapter 1

The Mechanics of Myocardial Infarction and Postinfarction Restraint

Every day, the heart beats over 100,000 times and pumps over 2,000 gallons of blood. Over the course of a 70-year lifetime, the heart will beat over 2.5 billion times and pump enough blood to fill 80 Olympic-sized swimming pools. About the size of two clenched fists in an adult, this impressive organ is divided into four chambers: two atria and two ventricles. Each heart beat is initiated by an electrical impulse originating in the heart itself and consists of coordinated contractions of the atria followed by the ventricles. The right ventricle pumps blood through the pulmonary circulation of the lungs while the larger, thick-walled left ventricle is responsible for pushing blood through the entire systemic circulation. At birth, humans begin with a fixed number of heart muscle cells, called cardiomyocytes, which change in size during development (and in response to various stimuli in adulthood) but do not multiply or divide. While this protects the

heart from diseases of cell division (e.g. cancer), it also means that heart muscle cannot regenerate: damage or injury to the myocardium remains irreversible.

The cardiac cycle

The coordinated sequence of muscular contractions that moves blood through each chamber of the heart makes up the cardiac cycle. Deoxygenated blood flows from the systemic veins into the right atrium and enters the right ventricle. Blood is pumped from the right ventricle through the pulmonary circuit to be oxygenated, and then re-enters the heart through the left atrium and travels to the left ventricle. From there, forceful contractions push blood into the aorta and through the systemic arteries. Also branching from the aorta are the origins of the coronary circulatory network, which supplies oxygenated blood to the heart muscle itself.

The directional flow of blood through the heart is controlled by one-way valves between chambers and by the timing of contraction of the chambers. The electrical stimulus for contraction begins at the sinoatrial node (located in the right atrium), propagates through the atria to the atrioventricular node, and travels down the intraventricular septum to initiate contraction of the ventricles near the apex. The atrioventricular node slightly delays the conductance of the impulse between the atria and ventricles, thus allowing the atria to fully contract and finish emptying blood into the ventricles before ventricular contraction begins. The phases of the cardiac cycle are usually described based on the current state of the ventricles rather than the atria. The period of ventricular filling is referred to as diastole, while the period of ventricular activation is termed systole. Dysfunction in either phase can have devastating effects on overall heart function: preventing adequate filling or reducing the amount of active contraction each result in a net loss in the amount of blood the heart is able to pump per

beat. Therefore, rescue of both systolic and diastolic function are both crucial targets for improving heart function following myocardial injury.

Mechanics of myocardial infarction

Each year, over 1 million Americans will suffer a new or recurrent heart attack, or myocardial infarction (MI) (Roger et al., 2011). An MI most commonly occurs when a coronary artery becomes occluded, cutting off blood flow to the area of myocardium supplied by that vessel (Figure 1.1). Within minutes, the ischemic region becomes passive and non-contractile. Since the mechanical properties of the infarct still closely mirror those of normal, passive myocardium, the diastolic filling phase of the cycle remains unaffected (Bogen, Rabinowitz, Needleman, McMahan, & Abelmann, 1980). However, during systole the infarct stretches and bulges outward while the rest of the heart is contracting and moving inward. As a result, the mechanical efficiency of the heart as a pump and the volume of blood the heart is able to eject with each beat are decreased, leading to a series of short- and long-term compensatory changes (Holmes, Borg, and Covell 2005). Diastolic pressure and volume rise, leading to enhanced contractility of the viable myocardium through the Frank-Starling mechanism (Nieminen & Heikkilä, 1976). Reflex activation of the sympathetic nervous system can also help preserve cardiac output (CO) by enhancing contractility and increasing heart rate (HR). This sympathetic stimulation helps to limit the severity of functional depression acutely post-MI, but becomes problematic in the long term; prolonged sympathetic activation is frequently associated with progression of chronic heart failure (HF) (Bristow et al., 1982; Thomas & Marks, 1978).

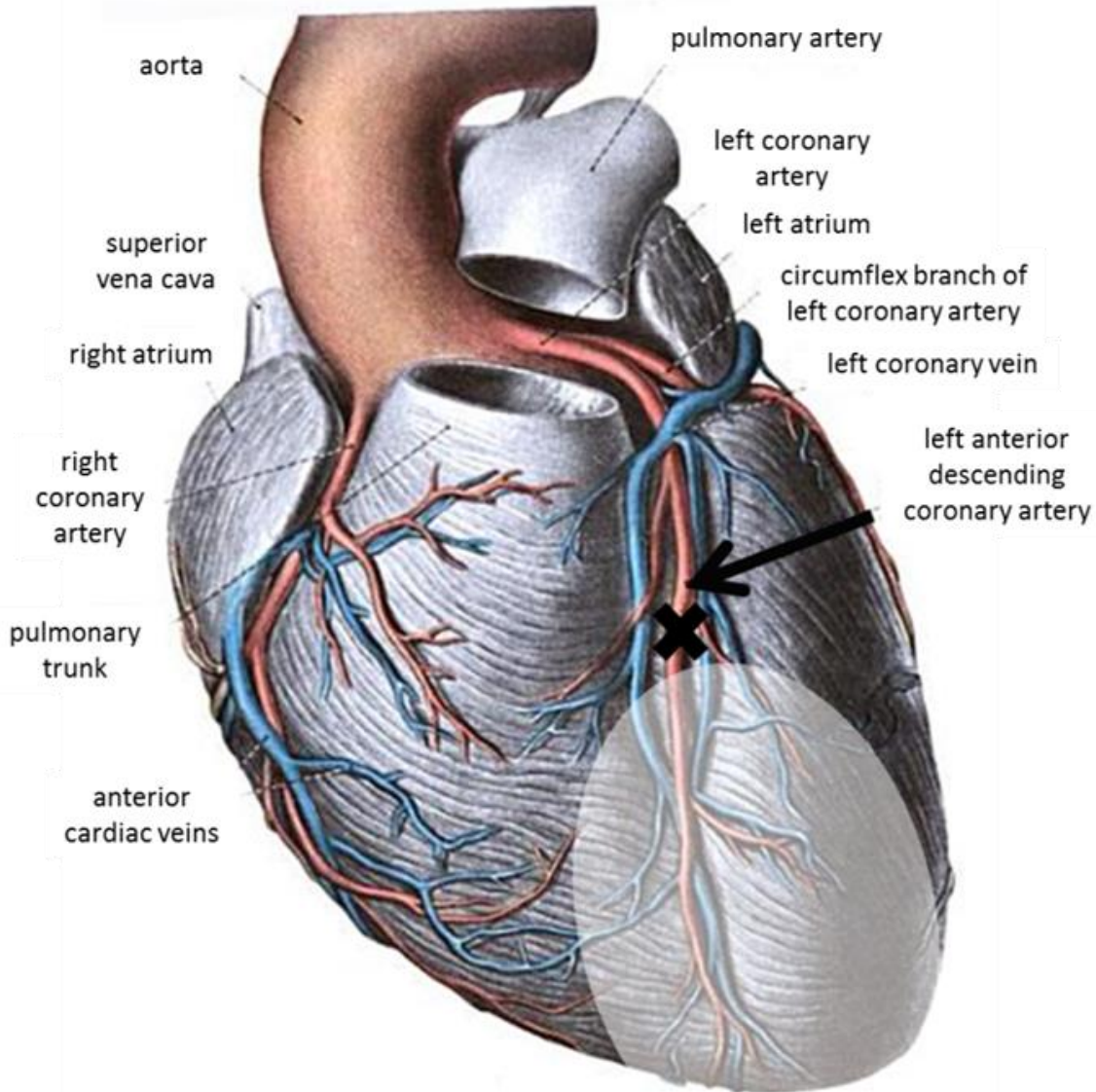


Figure 1.1 A myocardial infarction (MI) occurs when a coronary artery, here the left anterior descending (LAD) artery (marked by the black arrow), becomes occluded, leaving the myocardium normally perfused by that vessel (shaded in light gray) without blood supply. Adapted from Sobotta 1907.

After several hours of occlusion, the passive properties of the nonviable myocardium do start to change, with clear infarct stiffening by 6 hours post-occlusion (Pirzada, Ekong, Vokonas, Apstein, & Hood, 1976; Vokonas, Pirzada, & Hood, 1976). The first week following MI is dominated by processes of inflammation and necrosis, and although infarct stiffening is observed, the scar is also most prone to rupture during this time (Birnbaum et al., 2003). In this week, necrotic muscle is being degraded with limited deposition of new collagen, which in combination with the infarct expansion and thinning that is also likely to occur, leaves the infarct area mechanically compromised. However, by the end of the first week post-MI, fibroblasts rapidly infiltrate the infarct and subsequent deposition of new collagen fibers by these fibroblasts rises quickly (Fishbein, Maclean, & Maroko, 1978). Over the course of the next few weeks, infarct stiffness rises with increasing collagen content, but the mechanical behavior of the scar that forms also depends heavily on the structure of the collagen fibers that constitute it. In some infarcts, parallel collagen fibers give rise to an anisotropic scar that is much stiffer in the fiber direction, while randomly oriented collagen fibers in other infarcts result in an isotropic scar that exhibits the same stiffness in both the circumferential and longitudinal directions (Fomovsky and Holmes 2010; Gupta et al. 1994; Holmes, Nuñez, and Covell 1997). Different animal models have been shown to form different scar structures, as have different infarct locations in the same animal model; our group recently showed that patterns of stretch in the scar during healing correlate with scar structure across these animal models and proposed that mechanical guidance of scar formation could explain much of the reported variation (Fomovsky, Rouillard, & Holmes, 2012; Rouillard & Holmes, 2012).

After several weeks of healing, the infarct is stiffer than normal myocardium and remains so indefinitely. Scar compaction is observed in some animal models (especially dogs), resulting in a smaller, denser scar (Jugdutt & Amy, 1986). The left ventricle (LV)

continues to remodel for several months, and in the case of small infarcts LV function generally improves throughout the healing process (Kupper, Bleifeld, Hanrath, Mathey, & Effert, 1977). Unfortunately, the opposite is observed for large infarcts where dysfunction is too severe; compensatory mechanisms are insufficient and pathological remodeling processes dominate (Pfeffer et al. 1991; Pfeffer et al. 1979). As opposed to compacting, the infarct gradually becomes larger and thinner, compromising the mechanical integrity of the scar and exacerbating contractile dysfunction in the borderzone myocardium. In these cases, continuing dilation of the entire ventricle leads to increased wall stresses and further dilation, creating a positive feedback loop that ultimately leads to heart failure.

Metrics for measuring changes in LV function

There are many metrics that are used to compare cardiac function across treatment groups or experimental states. The slope of the end-systolic pressure-volume relationship (ESPVR), often called end-systolic elastance (Ees), and the peak rate of systolic pressure generation (max dP/dt) are fairly reliable indicators of systolic contractility, although simultaneous changes in diastolic function can potentially offset systolic improvements. By contrast, many studies of cardiac reinforcement and restraint report recovery of systolic function assessed by ejection fraction (EF), systolic wall thickening (WT), or fractional shortening (FS), all of which must be interpreted with caution in the post-MI or failing heart.

EF reflects the fraction of blood that the heart is able to eject with each beat, calculated from end-diastolic volume (EDV), end-systolic volume (ESV), and stroke volume (SV):

$$SV = EDV - ESV$$

$$EF = \frac{SV}{EDV} = \frac{EDV - ESV}{EDV}$$

Although it is the most commonly reported functional measure, EF is particularly difficult to interpret in the setting of post-infarction remodeling, for two reasons. First, because the heart compensates for infarction using the Frank-Starling mechanism, changes in SV are difficult to interpret unless ventricular pressures, end-diastolic (EDP) and end-systolic (ESP), are also measured. For example, in the setting of a large acute infarct, SV typically changes little while LV EDP increases dramatically; the combination of unchanged SV and increased EDP clearly indicate reduced pumping capacity, while the isolated fact that SV is unchanged could be easily misinterpreted. Changes in HR due to sympathetic activation can similarly confound interpretation of SV. Second, once the heart begins to dilate, changes in the denominator of the EF calculation can also be misleading. EDV can change due to growth and remodeling of the heart as well as due to changes in preload, causing changes in EF that may be unrelated to actual pump function. In order to fully understand and separate functional and geometric changes during post-infarction remodeling and therapy, it is important to assess function by comparing Starling curves (plots of CO as a function of LV EDP), or at least hemodynamics at matched pressures. A similar logic applies to the changes in LV EDV and end-systolic volume (ESV), commonly used to evaluate the degree of LV cavity dilation as the ventricle remodels. Because both remodeling and changes in hemodynamics will affect these volumes, it is important to assess diastolic and systolic volumes at matched pressures, or even better over a range of pressures (i.e., comparing pressure-volume relationships).

Local metrics used to assess function include infarct or borderzone fractional shortening, which describes the percent decrease in LV short axis diameter from end-

diastole (ED) to end-systole (ES), and systolic wall thickening, which describes the percent increase in wall thickness from ED to ES. As will be described in the CorCap restraint section, extensive mechanical coupling between the infarct and borderzone allows transmission of abnormal motion from the scar to the surrounding myocardium. Tethering to an excessively compliant or stiff scar can directly cause functional impairment of the adjacent viable and otherwise normal myocardium. Therefore, differences in systolic FS or WT may be partially reflective of changes in scar mechanical properties or in mechanical coupling between the muscle and scar. Additionally, both of these indices assume that radial wall motion implies active contraction, yet we know that both coupling to adjacent myocardium and prominent shearing can decouple WT from active shortening in healing infarcts. For example, using implanted radiopaque markers filmed with high-speed cineradiography, Holmes et al. observed apparently normal levels of WT in the center of 3-week-old porcine infarcts, despite the fact that on histology these infarcts contained >60% collagen and no apparently viable myocytes (Holmes, Nuñez, and Covell 1997). Because so few studies of infarct mechanics and post-infarction therapy have measured both regional and global function over a range of preloads, the relationship between regional shortening or thickening in the infarct and border zone and global pump function remains unclear, suggesting caution in drawing conclusions about global function from regional measures.

Mechanical reinforcement of the infarcted left ventricle

As discussed above, myocardial dysfunction in the infarct area triggers a series of compensatory mechanisms that can ultimately lead to heart failure. Patients who suffer a large MI on the anterior wall (arising from occlusion of the left anterior descending coronary artery [LAD]) are especially at risk, and exhibit HF and cardiac mortality rates

more than double those for patients with infarcts in other locations (Stone, Raabe, & Jaffe, 1988). When stratified by infarct size, 62% of hearts in the largest anterior infarct quartile developed heart failure over an average of 30.8 months post-MI (Stone et al., 1988). Therefore, preventing or slowing the development of HF is a central therapeutic goal in treating patients who survive an infarction. Current pharmacologic therapies aim to reduce both LV dilation (angiotensin converting enzyme inhibitors) and sympathetic activation (beta-adrenergic blockers).

In addition to pharmacologic treatments, a number of mechanical reinforcement strategies have been explored. Work in this area began with efforts to restrain and stimulate the failing heart by wrapping the epicardium with the latissimus dorsi muscle and stimulating the skeletal muscle wrap to contract (Chachques et al. 2008; Lee et al. 1991). However, later clinical studies showed that the passive restraint effect of the wrap was the principal source of its efficacy, and the procedure was subsequently abandoned because of its complexity (Grandjean, Austin, Chan, Terpstra, & Bourgeois, 1991). Building on the promising results of passive restraint, devices were then developed to treat end-stage HF by physically restraining the LV, and use of these devices was later extended from treatment of HF to prevention of LV dilation post-MI. Next, several groups considered whether localized mechanical restraint of the infarct could similarly limit LV dilation. More recently, a number of variants on local restraint – including tissue-engineered and cell-seeded patches and anisotropic reinforcement – aim to prevent the progression to HF by improving LV function early after infarction, instead of or in addition to physically preventing dilation.

Bi-ventricular restraint

The rationale for total ventricular restraint in HF is to limit further dilation of the ventricle, and potentially even reverse some of the dilation that has already occurred. Restraint following MI has the same objective, although if the device is applied early enough post-MI, it can also serve to prevent significant cavity dilation before it occurs.

Acorn CorCap

The Acorn Corcap cardiac support device (CSD) is a mesh-like device that surrounds the heart, covering both the left and right ventricles. The knitted polyester construction makes the device fairly compliant, although it is designed to provide diastolic support that is greater in the circumferential direction than in the apex-base direction (Oz et al., 2003). Prior to implantation, the most appropriate CSD is chosen from 6 available sizes. The CSD is first attached to the epicardium with a ring of sutures around the base of the heart. The two abutting edges of the CSD are then drawn together and sutured, creating a seam on the anterior wall. By controlling the amount of mesh drawn into the anterior seam, the surgeon can further adjust the CSD fit but can also generate substantial amounts of circumferential tension in the device (Oz et al., 2003). When properly positioned and tightened, the device is intended to bear enough of the end-diastolic load to reduce the degree of stretching and the magnitude of wall stress at ED.

Prior to exploration of the CorCap as a post-MI therapy, it showed promise as a treatment for heart failure in large animal studies using both rapid pacing and global ischemia models (Chaudhry et al., 2000; Power et al., 1999). Investigations of the device were then expanded to include studies of its ability to prevent dilation following myocardial infarction. One group has conducted several studies in sheep to examine the effects of CorCap implantation following MI (Blom et al., 2005, 2007; Pilla et al.,

2005). In each study, the infarct was created by permanently ligating all of the diagonal branches of the LAD. One week post-MI, half of the animals underwent CSD implantation while the other half served as MI-only controls. MRI data in all studies from either 8 weeks, 12 weeks, or 3 months post-MI showed smaller EDV and ESV in the CSD group compared to control, indicating attenuation of LV dilation, although in all studies the final LV volumes in the treatment groups were still significantly higher than the pre-MI baseline (Figure 1.2) (Blom et al., 2005, 2007; Pilla et al., 2005). Interestingly, inconsistent changes in infarct size were observed in two studies from the same group. Using the same final time point of 12 weeks post-MI, one of the studies found that reinforced infarcts were smaller in area than unreinforced infarcts, while the other showed infarct sizes were similar between the two groups. In both studies, the CorCap group exhibited higher EF than the control group, although SV in the two groups was similar (Blom et al., 2005, 2007). Compared to control animals, the CSD group also showed greater preservation of percent systolic WT and radial strain in the borderzone, which was defined to start at the infarct boundary and span 20° in the direction of the septum (Blom et al., 2005, 2007). This result highlights the impact of mechanical coupling between the non-contractile infarct and the surrounding, viable myocardium. The ability of the borderzone to contract normally can be inhibited by its tethering to the infarct at any stage of healing, whether by the stretching and bulging of an acute infarct or the presence of a very stiff, collagenous scar. These data suggest that mechanical reinforcement can act to ameliorate this transmitted dysfunction.

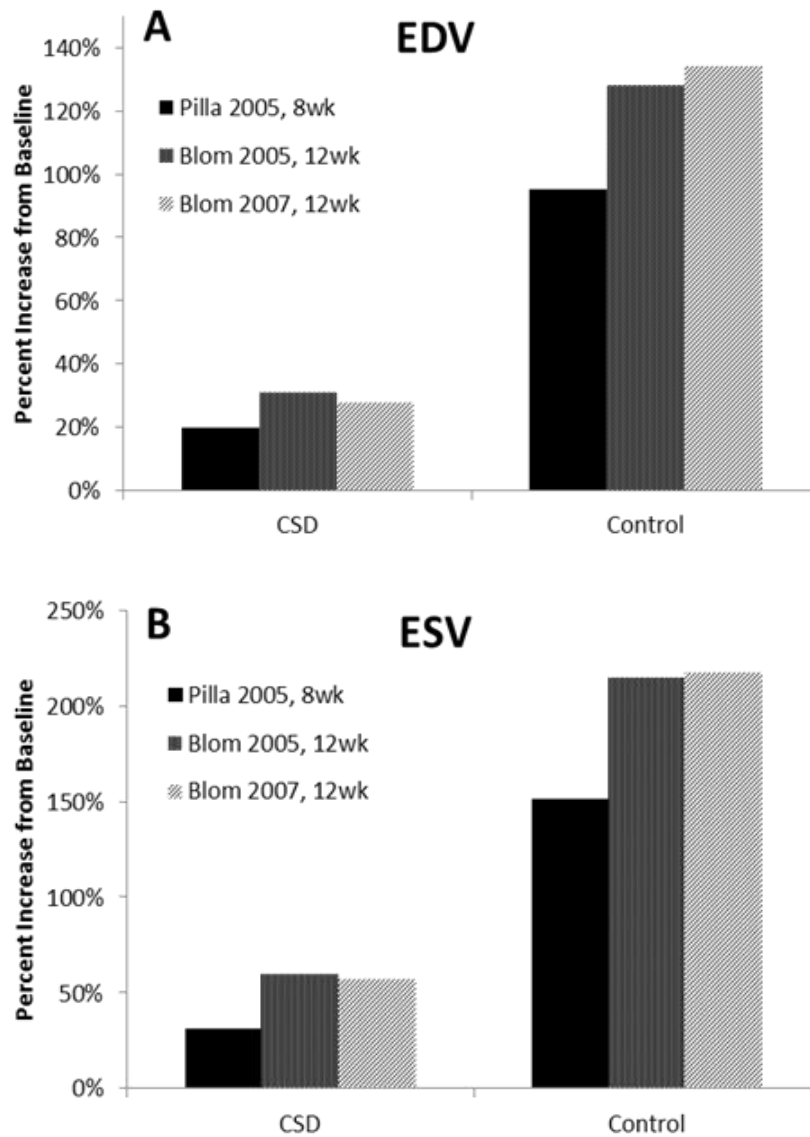


Figure 1.2 Changes in (A) end-diastolic and (B) end-systolic LV volumes following post-infarction CorCap reinforcement. Volumes at the final time point for the CorCap (CSD) and control groups are represented as the percent increase from the pre-MI baseline value. Created with data from Blom et al. 2005, 2007 and Pilla et al. 2005.

Paracor HeartNet

The Paracor HeartNet cardiac support device is another passive, bi-ventricular restraint device that wraps around the epicardium of both the left and right ventricles. The HeartNet consists of a wire mesh made of Nitinol, a nickel and titanium alloy. The device is designed to be flexible and elastic, so that a snug fit is achieved around the heart (if the appropriate device size is chosen pre-procedure) without making further adjustments. Unlike the CorCap and unlike native pericardium, stretch in the Paracor CSD has been shown to vary linearly with increasing pressure, and the HeartNet exhibits much greater compliance at high pressures than either of the other two (Gummert, Rahmel, Bossert, & Mohr, 2004). One distinguishing feature of the HeartNet is the inclusion of a delivery system that makes the implantation procedure less invasive than for other CSDs.

Similarly to the CorCap, the HeartNet has been studied in large animal models of chronic heart failure (George et al., 2007) and post-infarction remodeling. One post-MI study used an ovine model of coronary ligation similar to those in the CorCap studies, although this model employed permanent ligation of the main LAD as opposed to the diagonal branches (Magovern et al., 2006). Also unlike the studies described previously, infarction and reinforcement were performed as a single surgical procedure, with HeartNet implantation immediately following ligation in 7 of 14 animals. At 6 weeks post-MI, CSD animals exhibited smaller increases in LV mass, EDV, and ESV (all normalized to body surface area) compared to control animals. However, this apparent prevention of dilation did not seem to translate to improved function, as no differences in EF, SV or CO were found between the groups at the end of the study.

Left ventricular restraint

In contrast to the sock-like structure of the Acorn and Paracor devices, which wrap around both ventricles, the Myocor Coapsys (Myosplint) and the CardioClasp interact with the LV only and take a different approach to modifying the shape of the heart. Compared to the CorCap and HeartNet, the Coapsys and CardioClasp have not been well studied as post-MI therapies. Since implantation of both the Coapsys and CardioClasp may involve placing instrumentation directly into or over only part of the ischemic area (as opposed to reinforcing the entire infarct), it is possible that these devices have not been explored as post-MI treatments due to concerns regarding the potential for concentration of stresses within an already weakened acute infarct. Nevertheless, their efficacy as treatments for HF (both ischemic and nonischemic) has been evaluated through animal studies, clinical trials, and finite element modeling.

Myocor Coapsys (Myosplint)

The Myocor Coapsys has been referred to as the Myosplint in animal studies of the device but has been primarily called the Coapsys in human clinical trials. The Coapsys is placed on the epicardium of the LV and consists of two rigid pads connected through the cavity. The pads are first positioned on opposing surfaces of the LV, one on the anterior and the other on the posterior wall, and then drawn together by the tension member, which is fed through the LV cavity. Increasing the tension between the two epicardial pads reshapes the enlarged LV, creating a bilobular ventricle with decreased chamber radius (McCarthy et al., 2001). Typically 3 Myosplints are used, aligned in a longitudinal (apex-base) line on the LV, and tension is adjusted until the radius of each new lobe is approximately 80% of the radius of the un-reinforced LV cavity. Coapsys reinforcement was shown to significantly reduce LV dilation in a canine model of

rapid pacing heart failure, although no functional improvements were observed (McCarthy et al., 2001).

In addition to *in vivo* studies both animals and patients, some groups have used finite element (FE) models to evaluate the effects of restraint devices *in silico*. Guccione et al. used a model to simulate the changes that occur immediately following Coapsys implantation in a failing heart (Guccione et al., 2003). First, an FE model of a globally dilated heart was generated to represent the HF state. Application of 3 Myosplints was simulated by modifying the mesh assuming a 25% reduction in end-diastolic LV diameter at each attachment site. Not surprisingly, EDV and ESV were found to be reduced when the Coapsys model was inflated to the same EDP and ESP as the HF model. Starling curves for the pre- and post-operative models were almost identical, indicating that no functional improvement was generated by Coapsys restraint. However, dramatic reductions in average fiber stresses throughout the myocardium at both ED and ES were observed in the Coapsys FE model, suggesting potential for this type of reinforcement to retard or prevent further pathological remodeling in the compromised heart.

CardioClasp

The CardioClasp CSD consists of two rigid bars connected through the LV cavity by an adjustable tether. The long, thin bars are designed to mimic the natural contours of the heart, and are attached to the epicardial surface via contact pads that are flexible along their length but not across their width. The bars are aligned longitudinally on the anterior and posterior walls, in a very similar configuration to the one used for placement of Myosplints. Following implantation, the tension in the tether is adjusted to draw the anterior and posterior bars together until an approximate 30% reduction in

the end-diastolic anterior-posterior dimension is observed (Kashem et al., 2002). The CardioClasp reinforcement scheme follows the same principle as described for Coapsys restraint: use anterior-posterior tension to reshape the LV cavity and create two lobes of smaller diameter in the hopes of reducing LV wall stresses and adverse remodeling. One group has conducted several studies testing the effects of CardioClasp implantation in a canine rapid-pacing HF model and found that reinforcement reduced LV cavity dimensions and increased systolic contractility but did not improve cardiac output (Kashem, Hassan, Crabbe, Melvin, & Santamore, 2003; Kashem et al., 2002; Kashem, Santamore, et al., 2003)

Optimized global restraint

Optimization of bi-ventricular restraint has been performed using a technique called Quantitative Ventricular Restraint (QVR) (Ghanta et al., 2007). In this method, a half-ellipsoidal polyurethane balloon is implanted around both ventricles and is inflated to generate restraint. Fluid can be added to or withdrawn from the lumen to vary the inflation pressure and subsequent degree of restraint via an external access line. Ghanta et al. applied several restraint levels in an ovine coronary ligation model of ischemic HF. Investigation of the acute hemodynamic effects of each of the restraint levels revealed a monotonic decrease in both SV and CO and an increase in EDP with increasing QVR pressure (Figure 1.3). The optimum restraint level was selected to be one of the intermediate values, based on the criteria of maximizing the reductions in transmural myocardial pressure and myocardial oxygen consumption while minimizing the deleterious hemodynamic effects. After 2 months of reinforcement at this optimized level, QVR animals showed an increase in EF and decrease in EDV from the pre-treatment baseline, while control animals showed opposite changes in both parameters. Interestingly, restraint pressure was found to decrease over time as the LV

cavity reverse remodeled, to the point where there was no longer any restraint pressure being applied at the conclusion of the experiment.

In a follow-up study, the same group examined the effects of several levels of adjustable and measurable ventricular restraint (AMVR) on long-term LV remodeling (Lee et al. 2012). Both the low level and high level restraint groups showed decreases in LV volumes and an increase in EF from pre-treatment to 2 months post-treatment while control animals showed opposite changes. Changes in each metric were consistently of greater magnitude in the high restraint than in the low restraint group, and the speed of reverse remodeling was shown to be significantly accelerated in the high restraint group. In the second part of the study, the researchers used the AMVR device to compare the effects of static and adjustable restraint, in which fluid was added to the balloon lumen to maintain a constant restraint pressure over the course of the 2-month remodeling period. Although adjustable restraint enhanced reductions in LV volumes, no significant differences were observed in EF, SV or CO after 8 weeks of either static or adjustable restraint. Jhun et al. used a computational approach to study how different levels of global passive epicardial restraint affect pump function and wall stress in the dilated left ventricle (Jhun et al., 2010). In agreement with experimental studies, they found that increasing levels of pressure applied to the epicardium gradually reduced predicted SV and CO. Their model data suggest that epicardial restraint restricts filling more than it improves systolic function, depressing the Starling curve despite reducing systolic wall stress.

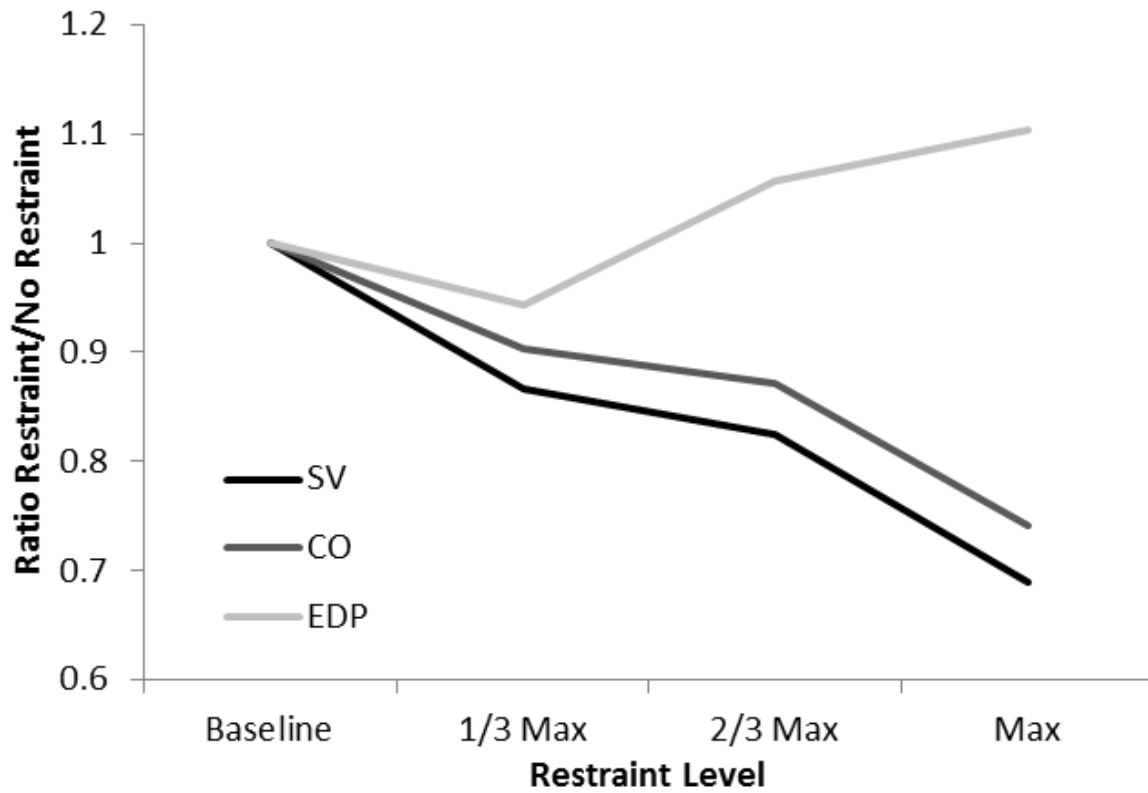


Figure 1.3 Acute hemodynamic changes with increasing levels of passive restraint. Created with data from Ghanta et al. 2007.

Global restraint limits dilation

A prominent theme that emerges from studies investigating the effects of cardiac restraint device implantation in HF or post-MI is that ventricular restraint reduces LV cavity size and decreases the severity of dilation. Therefore, these global approaches to ventricular reinforcement hold promise for preventing the development or reversing the progression of HF. However, multiple clinical trials have failed to demonstrate clear improvements in functional outcomes, and changes in functional indices employed in many animal studies are difficult to interpret (Table 1.1). Although most of the studies discussed in this chapter showed decreased LV volumes with mixed changes in functional metrics, there were some studies in which no functional differences at all were observed between the treatment and control groups. For example, Magovern et al. measured reductions in LV volume after HeartNet implantation but saw no changes in EF, SV or CO compared to control (Magovern et al., 2006). In general, studies of CorCap reinforcement showed increases in EF and systolic FS or WT, but no changes in SV, CO, or dP/dt . Therefore, it is possible that the device is producing improvements in systolic function, but as discussed in the beginning of this chapter, concurrent geometric and material changes in the heart also affect these indices (EF and FS/WT) and make it impossible to draw definitive conclusions from these values. Similar to the CorCap, mixed results were also obtained in studies of the other three ventricular restraint devices. Coapsys reinforcement increased EF without affecting SV and CO, while CardioClasp increased FAC without changing CO or dP/dt . However, studies of both devices also showed increases in the slope of the systolic curve of pressure-volume, pressure-short axis area, or pressure-segment length curves. Therefore, due to the inconsistencies in the functional changes observed in the studies discussed and the difficulty in interpreting some of the indices used, the true effects of total ventricular restraint on cardiac function remain unclear.

Table 1.1 Summary of ventricular restraint device studies

Reference	Animal	Infarct/HF Model	Restraint Device	EDV	ESV	EF	SV	CO	FS/FA S/WT	dP/dt	ESPVR
Power 1999	Sheep	Rapid Pacing	CorCap				↔	↔	↑FS	↔	
Chaudry 2000	Dog	Micro-embolization	CorCap	↓					↑FAS		
Pilla 2005	Sheep	LAD Ligation	CorCap	↓	↓				↑WT in BZ		
Blom 2005	Sheep	LAD Ligation	CorCap	↓	↓	↑	↔				
Blom 2007	Sheep	LAD Ligation	CorCap	↓	↓	↑			↑RS in BZ		
George 2007	Dog	Micro-embolization	HeartNet	↓	↓						
Magovern 2006	Sheep	LAD Ligation	HeartNet	↓	↓	↔	↔	↔			
McCarthy 2001	Dog	Rapid Pacing	Coapsys	↓	↓	↑	↔	↔			
Guccione 2003	Human	FEM	Coapsys	↓	↓			↔			↑ESPVR
Kashem 2002	Dog	Rapid Pacing	Cardio-Clasp						↑FAC		↑ESPVLR
Kashem 2003b	Dog	Rapid Pacing	Cardio-Clasp	↓ED CSA	↓ES CSA						↑ESPVR
Kashem 2003a	Dog	Rapid Pacing	Cardio-Clasp					↔		↔	↑ESPAR
Ghanta 2007	Sheep	LAD Diag. Ligation	Optimized QVR	↓		↑					
Lee 2012	Sheep	LAD Diag. Ligation	AMVR vs. Static	↓	↓	↑					

HF = heart failure, EDV = end-diastolic volume, ESV = end-systolic volume, EF = ejection fraction, SV = stroke volume, CO = cardiac output, FS = fractional shortening, FAS = fractional area shortening, FAC = fractional area of contraction, WT = wall thickening, RS = radial strain, dP/dt = rate of systolic pressure generation, ESPVR (ESPAR, ESPVLR) = slope of the end-systolic pressure-volume (pressure-area, pressure-segment length) relationship, BZ = borderzone, CSA = cross-sectional area, LAD = left anterior descending coronary artery, FEM = finite element model, QVR = quantitative ventricular restraint, AMVR = adjustable and measureable ventricular restraint

Limitations of whole ventricle restraint

Although they have been shown to limit progression toward dilated heart failure following MI, there are still significant limitations associated with CSD use. A prominent drawback is the invasiveness of the procedures that are required to implant most of the devices. The risks of performing an open chest procedure on a patient who recently had a large MI make these devices unattractive as post-infarction therapies. Another potential drawback of the total ventricular restraint approach for post-MI reinforcement is the possibility of interference with the normal myocardium. For example, implanting a globally stiff CSD may work well to reinforce a compliant infarct scar, but may also inhibit diastolic filling throughout the ventricle. Although several of the commercialized restraint devices (Acorn CorCap and Paracor HeartNet) have been shown to be much less stiff than the native pericardium that surrounds the heart, these devices have also been consistently shown to affect LV volumes. While long-term reductions in LV volumes can be indicative of attenuation of dilation, studies showing decreases in EDV during acute reinforcement suggest that global filling is immediately affected upon implantation. Local restraint approaches have attempted to address this issue by reinforcing only the nonviable infarct scar, and several variations of local restraint will be discussed in the following sections.

Local restraint

Once the idea of physically preventing post-infarction remodeling was established, it was natural to explore whether global restraint of the infarcted left ventricle is really necessary, or whether local restraint of the infarct region might be sufficient. Cardiac patches intended for local post-infarction application have taken a variety of forms, from synthetic to cell-seeded to completely tissue-engineered. Some aim to mechanically reinforce the infarct, while others are intended primarily to deliver

growth factors or cells to the damaged region. An extensive summary of materials that have been used in the construction of cardiac patches can be found in Rane and Christman 2011. Although a multitude of tissue engineered and cell-seeded patches have been fabricated and tested, not all are implanted or attached to the heart in a way that could affect mechanics. The present summary is limited to a discussion of post-MI patches that have a direct effect on infarct mechanics.

Synthetic patches

Early studies of local restraint showed that placing synthetic patches over the anticipated infarct region prior to inducing MI could reduce infarct expansion and LV dilation. Kelley et al. used the ovine MI model of permanent LAD ligation to investigate the effects of patch application pre-MI (Kelley et al., 1999). A polypropylene mesh patch was sutured onto the epicardium of the expected ischemic area (determined by temporary LAD occlusion) 10-14 days prior to ligation. By 8 weeks post-MI, patch animals exhibited lower EDV and ESV, and higher CO, SV, EF, and stroke work compared to control, although hemodynamic measurements were not compared at matched EDP (Figure 1.4). Moainie et al. used the same timeline of patch implantation and MI induction, only this time for an infarct arising from permanent ligation of the left circumflex (LCx) coronary artery instead of the LAD (Moainie et al., 2002). In contrast to the antero-apical infarcts that form in response to LAD occlusion, LCx infarcts develop on the posterior wall, closer to the base. In this study, implantation of a polypropylene patch 10-14 days prior to LCx ligation was unable to produce the hemodynamic changes observed using the same patch prior to LAD ligation. At 8 weeks post-MI, no significant differences were observed in CO, SV or EF between the patch and control groups. However, both global and local measures showed significant attenuation of infarct expansion and LV cavity dilation with reinforcement. Infarct

segment length at ED, EDV and ESV all rose substantially in control animals, while increases in patch animals were significantly less dramatic.

Because local restraint is intended to prevent infarct expansion, much of which occurs in the first few days after infarction, it seems logical to expect application of local patches to provide diminishing returns with increasing time after MI. A recent study by Liao and colleagues that showed significant geometric and hemodynamic benefits of local reinforcement 8 weeks after infarction was therefore very surprising (Liao et al., 2010). Infarction was induced through embolization of the LCx, followed by implantation of a multi-layered, polypropylene and polytetrafluoroethylene patch at 8 weeks post-MI. At the 20 week post-MI endpoint, the patch reinforcement animals had greater preservation of wall thickness, higher EF, smaller EDV and ESV, lower EDP and higher peak systolic pressure than control animals.

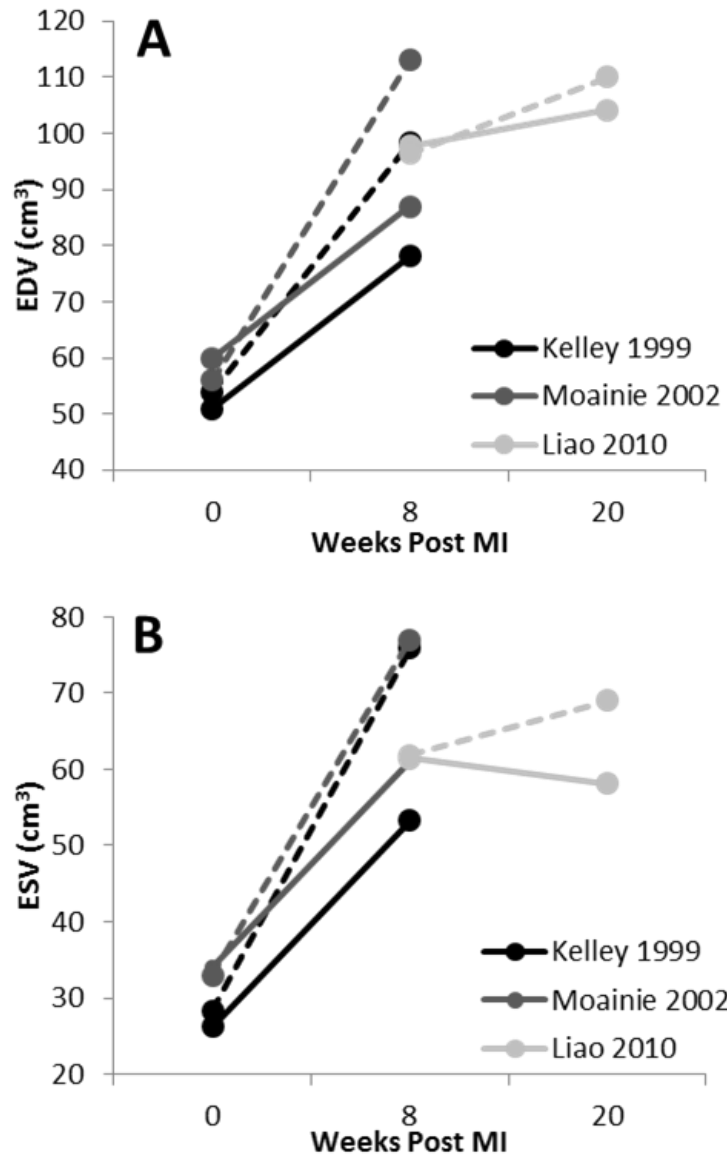


Figure 1.4 Changes in LV (A) end-diastolic and (B) end-systolic volumes following local patch reinforcement. Dotted lines indicate changes in the control group, solid lines indicate changes in the patch reinforcement group. Created with data from Kelley et al. 1999, Moainie et al. 2002, and Liao et al. 2010.

Fujimoto et al. also demonstrated remodeling benefits of post-infarction local reinforcement, suturing polyester urethane urea patches to the epicardium 2 weeks after LAD ligation in rats (Fujimoto et al., 2007). Unlike the polypropylene meshes, these patches were designed to be elastic and biodegradable, with erosion occurring over the course of several weeks. By 10 weeks post-MI, the degradable patches were observed to be significantly absorbed and well integrated with the ventricle wall, leading to better preservation of infarct wall thickness in patch animals. ED LV cavity area was maintained near its baseline value and fractional area of contraction (FAC) improved in the reinforcement group, compared to an increase in area and decrease in FAC in control animals. Infarct compliance measured during passive inflation of the LV showed that native 8 week infarct scars were stiffer than reinforced scars in both the circumferential and longitudinal directions (Figure 1.5). Overall, these results suggest that the biodegradable patches used in this study could have modulated the biology of infarct healing in addition to or instead of infarct mechanics.

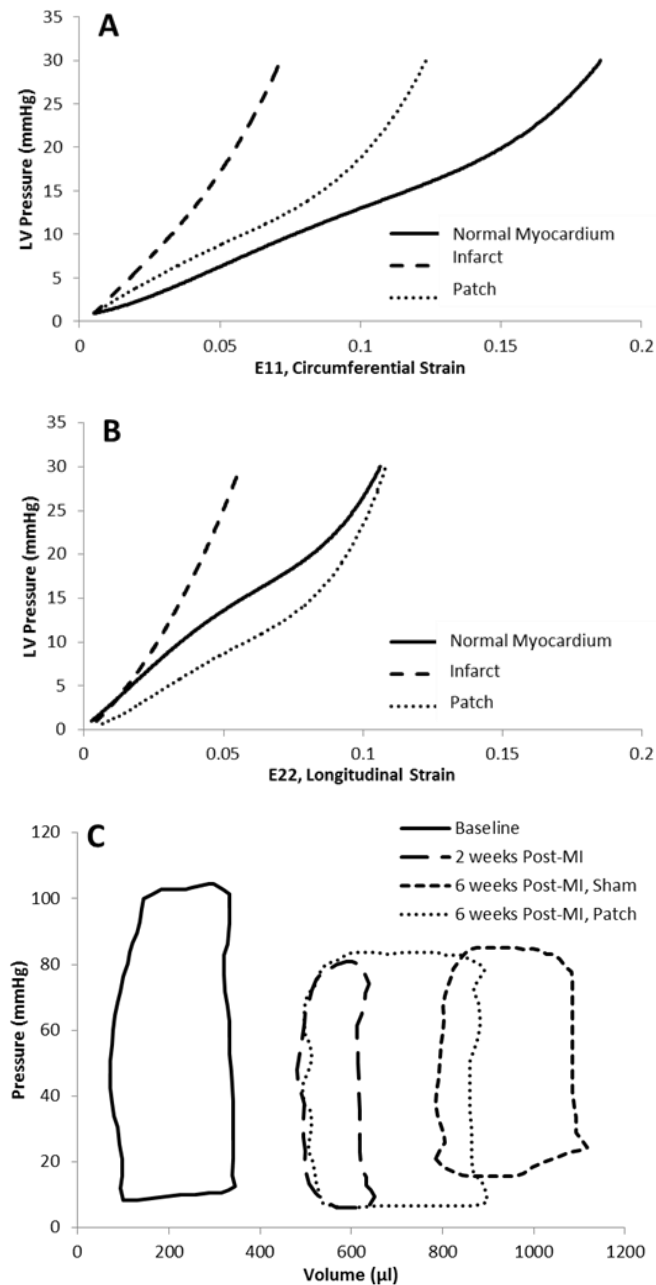


Figure 1.5 Effects of local infarct reinforcement in rats. Comparison of compliance in normal myocardium, polyester urethane urea patched infarcts, and unpatched infarcts in the **(A)** circumferential and **(B)** longitudinal directions (replotted from Fujimoto et al. 2007). **(C)** Pressure-volume loops following infarction and reinforcement with a viable engineered heart tissue patch (replotted from Zimmermann et al. 2006).

Cell seeded and tissue engineered patches

In an attempt to combine reinforcement with regeneration, numerous studies have sought to determine whether infarct restraint with tissue engineered patches, or combined therapies in which cells are seeded in a biological or synthetic matrix, offer greater benefit than synthetic reinforcement alone. Findings on functional improvement with regenerative approaches have been mixed, with some studies suggesting enhanced benefit over infarct reinforcement alone and others suggesting minimal difference in efficacy between the two approaches. In one of the studies that offered the most support for combining mechanical reinforcement with cell therapy, Liu and colleagues used a fibrin matrix seeded with autologous mesenchymal stem cells (MSC) to reinforce acute infarcts in pigs (Liu et al., 2004). After 60 minutes of LAD occlusion followed by reperfusion, a fibrin gel solution containing MSCs was placed onto the epicardium and allowed to polymerize into a semi-solid matrix. Terminal studies at 18-21 days post-MI revealed pronounced differences in systolic WT within the reperfused infarct, with active WT in seeded patch animals and passive stretching and wall thinning in both unpatched and unseeded patch animals. Kellar et al. also showed enhanced benefit using a cell-seeded patch compared to unseeded (Kellar, Shepherd, Larson, Naughton, & Williams, 2005). Permanent LAD ligation was used to infarct severe combined immunodeficient (SCID) mice, followed by immediate application of a poly(lactic-co-glycolic) acid mesh patch seeded with either viable or non-viable human dermal fibroblasts. At 2 weeks post-MI, EF and SV were higher in animals whose patches contained viable fibroblasts compared to the non-viable patch group. However, CO, EDP, ESP, EDV, and ESV were not observed to depend on cell viability and were similar between the two patch groups. Compared to control animals with unpatched infarcts, both patch groups showed improved EF, increased wall thickness, and lower EDP at 2 weeks post-MI.

Despite the evidence described above suggesting that combined reinforcement and regenerative therapies are superior to reinforcement alone, numerous other studies have shown minimal added benefit using cell seeded or tissue engineered patches when compared to the corresponding unseeded or non-viable construct. Zimmermann et al. examined implantation of heart tissue grafts made from neonatal rat cardiac cells over the infarct area 2 weeks after LAD ligation in rats (Zimmermann et al., 2006). By 6 weeks post-MI, not only were LV volumes, pressures, CO, SV, EF, FS and dP/dt all similar between the viable graft and non-cardiomyocyte graft groups, but the viable graft group also failed to show significant improvements in these metrics compared to the unpatched sham group, even though shifts in the pressure-volume behavior of the groups were observed (Figure 1.5). Using the same animal model, immediate application of a human MSC-seeded collagen scaffold to the infarct area led to improved FS and a smaller increase in ED and ES cavity dimension at 4 weeks post-MI compared to both the unseeded scaffold and the control groups (Simpson, Liu, Fan, Nerem, & Dudley, 2007). However, no differences in EDP, ESP or dP/dt were observed among the three experimental groups. In a similar study, infarcts created in rats by 5 hours of LAD occlusion were reinforced at 1 week post-MI with a poly(glycolide-co-caprolactone) scaffold seeded with bone marrow derived mononuclear cells (BMC) (Piao et al., 2007). 5 weeks post-MI, both BMC seeded and unseeded patch animals showed smaller ED and ES LV cavity dimensions, higher percentage of FS, greater preservation of wall thickness, and lower EDP than control animals. Over a much longer follow-up period, Giraud et al. used the rat LAD ligation model to compare the effects of seeded patches, unseeded patches and cell injection on long-term healing (Giraud et al., 2010). At 2 weeks post-MI, animals were randomized to receive implantation of a polyurethane patch seeded with rat skeletal myoblasts, implantation of an unseeded patch, or injection of skeletal myoblast suspension. One year after induction of MI, no differences in dP/dt or EDP were observed between the groups.

Interestingly, percent change in FS compared to pre-treatment baseline showed a delayed decrease in the seeded patch group (the first significant decrease in FS in this group was observed at 12 months compared to at 6 or 9 months in the other experimental groups), although this delayed decrease was so dramatic that the seeded patch group had the worst FS of all groups at the final time point.

Despite mixed conclusions regarding the potential of post-MI therapies that combine reinforcement with cell therapies to produce greater benefit than mechanical reinforcement alone, one fairly consistently finding across many studies is that mechanical therapy is superior to cell therapy when both are used in isolation. Several studies that have sought to compare various methods of cell delivery to an infarct have found greater remodeling benefits when cells are implanted with a scaffold or patch than when cells are injected into the infarct site. Godier-furnémont et al. used a rat LAD ligation model to show that immediate reinforcement with a decellularized human myocardium and fibrin hydrogel patch seeded with human MSCs reduced LV cavity dimensions at ED and ES and increased FS at 4 weeks post-MI to a greater degree than immediate injection of MSCs alone (Godier-Furnémont, Martens, Koeckert, Wan, & Parks, 2011). Chachques et al. examined the effects of cell injection vs. cell injection with cell seeded patch implantation in a clinical feasibility trial (Chachques et al., 2008). Out of 20 patients who presented with post-ischemic scars in the LV and indication for coronary artery bypass surgery, half received injection of autologous BMCs while the remaining half received BMC injection in conjunction with application of a BMC seeded collagen patch. At the end of the 10 month follow up period, the combined injection and patch group showed enhanced attenuation of pathological LV remodeling, exhibiting greater preservation of infarct wall thickness and larger magnitudes of reduction in EDV and ESV.

Local restraint limits dilation

Strikingly similar to the changes observed following total ventricular reinforcement with CSDs, the reports on whether a cardiac patch of any type actually improves pump function after a heart attack are mixed. As discussed in the beginning of the chapter, there are several metrics that are commonly used to quantify cardiac function with varying degrees of validity. To reiterate, evaluating shifts in CO v. LV EDP curves or calculating CO at matched values of LV EDP across different treatment conditions are the best methods to separate changes in pump function from the concurrent hemodynamic and geometric changes and make reliable conclusions about changes in cardiac function. Although EF and systolic FS or WT may reflect changes in active pumping capability, it is impossible to draw definitive conclusions from these values alone, because they are also sensitive to changes in cavity geometry, infarct mechanical properties, coupling between the infarct and the surrounding myocardium, and the amount of transmural shearing during contraction. Therefore, comparing cardiac function across unreinforced and reinforced states requires careful attention to the variety of geometric and hemodynamic changes during remodeling and cautious interpretation of the metrics used to make conclusions about functional improvements.

Although the studies discussed in this section all employ local reinforcement to restrain a large infarct, this seemingly similar mechanical intervention leads to widely varying reported changes in volume and function (Table 1.2). While a slight majority of studies do show a decrease in LV volume, diameter, or cross-sectional area, there are several cases in which patch reinforcement fails to reduce dilation, suggesting that it may be more difficult to limit LV dilation with patch restraint as opposed to ventricular restraint. In addition to the increased variability observed in volume changes, there is also slightly more variability in the reported functional changes following local vs.

global reinforcement. For example, Kelley et al. showed that patch reinforcement of an LAD infarct could reduce LV volumes and improve EF, SV, CO, and ESPVR slope, but using the same patch to reinforce an LCx infarct failed to improve any of these parameters compared to the control group (Kelley et al., 1999; Moainie et al., 2002). In addition, Zimmermann et al. found that reinforcing an LAD infarct with a different type of patch produced no changes in LV volumes, EF, SV, CO, FAS or dP/dt (Zimmermann et al., 2006). With the exception of one report of worsened dilation and FS following seeded patch application, most of the other studies discussed showed decreases in LV volumes and improvements in EF or FS.

In general, these studies show that local restraint can reduce LV volumes, while the metrics used to evaluate changes in LV function make it difficult to distinguish geometric changes from actual improvements in pumping. Across studies, consistent increases in EF and FS, FAC or WT are unaccompanied by increases in SV, CO, or dP/dt. However, as seen in Table 1.2, few studies actually measured more than one or two indices, so it is possible that there are true functional changes occurring that aren't being captured simply because they aren't being measured. Comparing the pool of local reinforcement studies described here to the global restraint studies discussed earlier, it appears that patch restraint can generate similar geometric and contractile changes to global restraint, although with slightly less consistency. However, since nearly every patch study described used a different type of patch material and attachment scheme, while global reinforcement studies employed commercialized devices with standard implantation procedures, it is not at all surprising to see significantly more variability in the results of the patch studies.

Table 1.2 Summary of local reinforcement studies

Reference	Animal	Infarct/HF Model	Patch Material	EDV	ESV	EF	S V	CO	FS/FA S/WT	dP/dt	ESPVR
Kelley 1999	Sheep	LAD Ligation	PP	↓	↓	↑	↑	↑			↑ESPVR
Moainie 2002	Sheep	LCx Ligation	PP	↔	↔	↔	↔	↔			
Fujimoto 2007	Rat	LAD Ligation	PEUU	↔ED CSA					↑FAC		
Liao 2010	Pig	LCx Embolization	PP + PTFE	↓	↓	↑					
Liu 2004	Pig	60min LAD Occlusion	Fibrin Matrix + MSC						↑WT in infarct*		
Kellar 2005	Mice	LAD Ligation	PLGA + Fibroblast		↓	↑*	↔	↔			↔ESPVR
Zimmermann 2006	Rat	LAD Ligation	EHTG	↔	↔	↔	↔	↔	↔FAS	↔	
Simpson 2007	Rat	LAD Ligation	Collagen + MSC	↓EDD*	↓ESD*				↑FS*	↔	
Piao 2007	Rat	5hr LAD Occlusion	PGCL + BMCs	↓EDD	↓ESD				↑FS		
Giraud 2010	Rat	LAD Ligation	PU + MyoB	↑EDD*					↓FS	↔	
Godierfurnemont 2011	Rat	LAD Ligation	Myocardium + Fibrin + MSC	↓EDD	↓ESD				↑FS		
Chachques 2008	Human	Post-isch. LV Scars	Collagen + BMCs	↓	↓						
Fomovsky 2012	Dog	LAD Ligation	Anisotropic Dacron		↓			↑			

LCx = left circumflex coronary artery, EDD = end-diastolic diameter, ESD = end-systolic diameter, PP = polypropylene, PEUU = polyester urethane urea, PTFE = polytetrafluoroethylene, MSC = mesenchymal stem cells, PLGA = poly(lactic-co-glycolic) acid, EHTG = engineered heart tissue graft, PGCL = poly(glycolide-co-caprolactone), PU = polyurethane, MyoB = myoblasts, See Table 1 caption for list of other relevant abbreviations. * indicates a significant difference from control in the seeded patch or viable construct group only, no symbol indicates a significant difference from control in all patch groups (seeded + unseeded/viable + non-viable)

Limitations of patch restraint

Although local restraint devices are applied to the infarct area and do not generally extend very far beyond the infarct borders, these patch approaches still hold some potential to influence contraction and affect motion in the borderzone and surrounding myocardium. However, wall motion at the infarct border, where passive scar intersects with contractile myocardium, is complex and underexplored. Locally reinforcing these tissues only increases the complexity of borderzone function, making the effects of local infarct reinforcement on the surrounding myocardium very difficult to decipher. Further investigation will be required before the effects of these local approaches on function in the borderzone and remote myocardium can be distinguished.

Conclusion

Overall, a common theme emerges from studies of both global and local infarct reinforcement: restraint therapies are consistently effective in reducing LV dilation, but the effects on post-MI LV function are unclear. The variability in functional changes between studies likely partially stems from variability in the restraint approach. However, measuring changes in function following MI and mechanical reinforcement is also often confounded by the choice of metrics that capture both changes in LV function and geometry. More comprehensive evaluation of both global and local infarct reinforcement devices may be required to isolate the effects of various mechanical restraint approaches on LV function.

References

- Birnbaum, Y., Chamoun, A. J., Anzuini, A., Lick, S. D., Ahmad, M., & Uretsky, B. F. (2003). Ventricular free wall rupture following acute myocardial infarction. *Coronary Artery Disease, 14*(6), 463–70.
- Blom, A. S., Mukherjee, R., Pilla, J. J., Lowry, A. S., Yarbrough, W. M., Mingoia, J. T., ... Spinale, F. G. (2005). Cardiac support device modifies left ventricular geometry and myocardial structure after myocardial infarction. *Circulation, 112*(9), 1274–83.
- Blom, A. S., Pilla, J. J., Arkles, J., Dougherty, L., Ryan, L. P., Gorman, J. H., ... Gorman, R. C. (2007). Ventricular restraint prevents infarct expansion and improves borderzone function after myocardial infarction: a study using magnetic resonance imaging, three-dimensional surface modeling, and myocardial tagging. *The Annals of Thoracic Surgery, 84*(6), 2004–10.
- Bogen, D. K., Rabinowitz, S. A., Needleman, A., McMahon, T. A., & Abelmann, W. H. (1980). An analysis of the mechanical disadvantage of myocardial infarction in the canine left ventricle. *Circulation Research, 47*(5), 728–41.
- Bristow, M. R., Ginsburg, R., Minobe, W., Cubicciotti, R. S., Sageman, S., Lurie, K., ... Stinson, E. B. (1982). Decreased catecholamine sensitivity and B-adrenergic-receptor density in failing human hearts. *The New England Journal of Medicine, 307*(4), 205–211.
- Chachques, J. C., Trainini, J. C., Lago, N., Cortes-Morichetti, M., Schussler, O., & Carpentier, A. (2008). Myocardial assistance by grafting a new bioartificial upgraded myocardium (MAGNUM trial): clinical feasibility study. *The Annals of Thoracic Surgery, 85*(3), 901–8.
- Chaudhry, P. A., Mishima, T., Sharov, V. G., Hawkins, J., Alferness, C., Paone, G., & Sabbah, H. N. (2000). Passive epicardial containment prevents ventricular remodeling in heart failure. *Annals of Thoracic Surgery, 70*, 1275–1280.
- Fishbein, M., Maclean, D., & Maroko, P. (1978). The histopathologic evolution of myocardial infarction. *Chest, 73*(6), 843–849.
- Fomovsky, G. M., & Holmes, J. W. (2010). Evolution of scar structure, mechanics, and ventricular function after myocardial infarction in the rat. *American Journal of Physiology, Heart and Circulatory Physiology, 298*(1), H221–8.

- Fomovsky, G. M., Rouillard, A. D., & Holmes, J. W. (2012). Regional mechanics determine collagen fiber structure in healing myocardial infarcts. *Journal of Molecular and Cellular Cardiology*, 52(5), 1083–90.
- Fujimoto, K. L., Tobita, K., Merryman, W. D., Guan, J., Momoi, N., Stolz, D. B., ... Wagner, W. R. (2007). An elastic, biodegradable cardiac patch induces contractile smooth muscle and improves cardiac remodeling and function in subacute myocardial infarction. *Journal of the American College of Cardiology*, 49(23), 2292–300.
- George, I., Cheng, Y., Yi, G.-H., He, K.-L., Li, X., Oz, M. C., ... Wang, J. (2007). Effect of passive cardiac containment on ventricular synchrony and cardiac function in awake dogs. *European Journal of Cardio-Thoracic Surgery*, 31(1), 55–64.
- Ghanta, R. K., Rangaraj, A., Umakanthan, R., Lee, L., Laurence, R. G., Fox, J. A., ... Chen, F. Y. (2007). Adjustable, physiological ventricular restraint improves left ventricular mechanics and reduces dilatation in an ovine model of chronic heart failure. *Circulation*, 115(10), 1201–10.
- Giraud, M.-N., Flueckiger, R., Cook, S., Ayuni, E., Siepe, M., Carrel, T., & Tevæarai, H. (2010). Long-term evaluation of myoblast seeded patches implanted on infarcted rat hearts. *Artificial Organs*, 34(6), E184–92.
- Godier-Furnémont, A. F. G., Martens, T. P., Koeckert, M. S., Wan, L., & Parks, J. (2011). Composite scaffold provides a cell delivery platform for cardiovascular repair. *Proceedings of the National Academy of Sciences of the United States of America*, 108(19), 7974–7979.
- Grandjean, P., Austin, L., Chan, S., Terpstra, B., & Bourgeois, I. (1991). Dynamic cardiomyoplasty: clinical follow-up results. *Journal of Cardiac Surgery*, 6, 80–88.
- Guccione, J. M., Salahieh, A., Moonly, S. M., Kortsmitt, J., Wallace, A. W., & Ratcliffe, M. B. (2003). Myosplint decreases wall stress without depressing function in the failing heart: a finite element model study. *The Annals of Thoracic Surgery*, 76(4), 1171–80; discussion 1180.
- Gummert, J. F., Rahmel, A., Bossert, T., & Mohr, F. W. (2004). Socks for the dilated heart. Does passive cardiomyoplasty have a role in long-term care for heart failure patients? *Zeitschrift Für Kardiologie*, 93(11), 849–54.

- Gupta, K. B., Ratcliffe, M. B., Fallert, M. A., Edmunds, L. H. J., & Bogen, D. K. (1994). Changes in passive mechanical stiffness of myocardial tissue with aneurysm formation. *Circulation*, *89*, 2315–2326.
- Holmes, J. W., Borg, T. K., & Covell, J. W. (2005). Structure and mechanics of healing myocardial infarcts. *Annual Review of Biomedical Engineering*, *7*, 223–53.
- Holmes, J. W., Nuñez, J. A., & Covell, J. W. (1997). Functional implications of myocardial scar structure. *The American Journal of Physiology Heart and Circulatory Physiology*, *272*(5 Pt 2), H2123–30.
- Jhun, C.-S., Wenk, J. F., Zhang, Z., Wall, S. T., Sun, K., Sabbah, H. N., ... Guccione, J. M. (2010). Effect of adjustable passive constraint on the failing left ventricle: a finite-element model study. *The Annals of Thoracic Surgery*, *89*(1), 132–7.
- Jugdutt, B. I., & Amy, R. W. M. (1986). Healing after myocardial infarction in the dog: changes in infarct hydroxyproline and topography. *Journal of the American College of Cardiology*, *7*(1), 91–102.
- Kashem, A., Hassan, S., Crabbe, D. L., Melvin, D. B., & Santamore, W. P. (2003). Left ventricular reshaping: effects on the pressure-volume relationship. *The Journal of Thoracic and Cardiovascular Surgery*, *125*(2), 391–9.
- Kashem, A., Santamore, W. P., Hassan, S., Crabbe, D. L., Margulies, K. B., & Melvin, D. B. (2002). CardioClasp: a new passive device to reshape cardiac enlargement. *American Society for Artificial Internal Organs Journal*, *48*, 253–259.
- Kashem, A., Santamore, W. P., Hassan, S., Melvin, D. B., Crabbe, D. L., Margulies, K. B., ... Lesniak, J. (2003). CardioClasp changes left ventricular shape acutely in enlarged canine heart. *Journal of Cardiac Surgery*, *18*, S49–S60.
- Kellar, R. S., Shepherd, B. R., Larson, D. F., Naughton, G. K., & Williams, S. K. (2005). Cardiac patch constructed from human fibroblasts attenuates reduction in cardiac function after acute infarct. *Tissue Engineering*, *11*(11-12), 1678–87.
- Kelley, S. T., Malekan, R., Gorman, J. H. I., Jackson, B. M., Gorman, C., Suzuki, Y., ... Edmunds, L. H. (1999). Restraining infarct expansion preserves left ventricular geometry and function after acute anteroapical infarction. *Circulation*, *99*, 135–142.
- Kupper, W., Bleifeld, W., Hanrath, P., Mathey, D., & Effert, S. (1977). Left ventricular hemodynamics and function in acute myocardial infarction: studies during the

acute phase, convalescence and late recovery. *The American Journal of Cardiology*, 40(6), 900–5.

Lee, K. F., Dignan, R. J., Parmar, J. M., Dyke, C. M., Benton, G., Yeh, T., ... Wechsler, a S. (1991). Effects of dynamic cardiomyoplasty on left ventricular performance and myocardial mechanics in dilated cardiomyopathy. *The Journal of Thoracic and Cardiovascular Surgery*, 102, 124–131.

Lee, L. S., Ghanta, R. K., Mokashi, S. A., Coelho-Filho, O., Kwong, R. Y., Kwon, M., ... Chen, F. Y. (2012). Optimized ventricular restraint therapy: adjustable restraint is superior to standard restraint in an ovine model of ischemic cardiomyopathy. *The Journal of Thoracic and Cardiovascular Surgery*, 145(3), 824–31.

Liao, S.-Y., Siu, C.-W., Liu, Y., Zhang, Y., Chan, W.-S., Wu, E. X., ... Tse, H.-F. (2010). Attenuation of left ventricular adverse remodeling with epicardial patching after myocardial infarction. *Journal of Cardiac Failure*, 16(7), 590–8.

Liu, J., Hu, Q., Wang, Z., Xu, C., Wang, X., Gong, G., ... Zhang, J. (2004). Autologous stem cell transplantation for myocardial repair. *American Journal of Physiology. Heart and Circulatory Physiology*, 287(2), H501–11.

Magovern, J. A., Teekell-Taylor, L., Mankad, S., Dasika, U., McGregor, W., Biederman, R. W. W., ... Trumble, D. R. (2006). Effect of a flexible ventricular restraint device on cardiac remodeling after acute myocardial infarction. *ASAIO Journal (American Society for Artificial Internal Organs)*, 52(2), 196–200.

McCarthy, P. M., Takagaki, M., Ochiai, Y., Young, J. B., Tabata, T., Shiota, T., ... Fukamachi, K. (2001). Device-based change in left ventricular shape: a new concept for the treatment of dilated cardiomyopathy. *The Journal of Thoracic and Cardiovascular Surgery*, 122(3), 482–90.

Moainie, S. L., Guy, T. S., Gorman, J. H. I., Plappert, T., Jackson, B. M., St John-Sutton, M. G., ... Gorman, R. C. (2002). Infarct restraint attenuates remodeling and reduces chronic ischemic mitral regurgitation after postero-lateral infarction. *The Annals of Thoracic Surgery*, 74(2), 444–9.

Nieminen, M., & Heikkilä, J. (1976). Echoventriculography in acute myocardial infarction. II: Monitoring of left ventricular performance. *British Heart Journal*, 38(3), 271–81.

- Oz, M. C., Konertz, W. F., Kleber, F. X., Mohr, F. W., Gummert, J. F., Ostermeyer, J., ... Smedira, N. (2003). Global surgical experience with the Acorn cardiac support device. *The Journal of Thoracic and Cardiovascular Surgery*, 126(4), 983–991.
- Pfeffer, J., Pfeffer, M., Fletcher, P., & Braunwald, E. (1991). Progressive ventricular remodeling in rat with myocardial infarction. *The American Journal of Physiology. Heart and Circulatory Physiology*, 260(5 Pt 2), H1406–14.
- Pfeffer, M., Pfeffer, J., Fishbein, M., Fletcher, P., Spadaro, J., Kloner, R., & Braunwald, E. (1979). Myocardial infarct size and ventricular function in rats. *Circulation Research*, 44, 503–512.
- Piao, H., Kwon, J.-S., Piao, S., Sohn, J.-H., Lee, Y.-S., Bae, J.-W., ... Cho, M.-C. (2007). Effects of cardiac patches engineered with bone marrow-derived mononuclear cells and PGCL scaffolds in a rat myocardial infarction model. *Biomaterials*, 28(4), 641–9.
- Pilla, J. J., Blom, A. S., Gorman, J. H. I., Brockman, D. J., Affuso, J., Parish, L. M., ... Gorman, R. C. (2005). Early postinfarction ventricular restraint improves borderzone wall thickening dynamics during remodeling. *The Annals of Thoracic Surgery*, 80(6), 2257–62.
- Pirzada, F. a., Ekong, E. a., Vokonas, P. S., Apstein, C. S., & Hood, W. B. (1976). Experimental myocardial infarction. XIII. Sequential changes in left ventricular pressure-length relationships in the acute phase. *Circulation*, 53(6), 970–975.
- Power, J. M., Raman, J., Dornom, A., Farish, S. J., Burrell, L. M., Tonkin, a M., ... Alferness, C. a. (1999). Passive ventricular constraint amends the course of heart failure: a study in an ovine model of dilated cardiomyopathy. *Cardiovascular Research*, 44(3), 549–55.
- Rane, A. a, & Christman, K. L. (2011). Biomaterials for the treatment of myocardial infarction: a 5-year update. *Journal of the American College of Cardiology*, 58(25), 2615–29.
- Roger, V. L., Go, A. S., Lloyd-Jones, D. M., Benjamin, E. J., Berry, J. D., Borden, W. B., ... Turner, M. B. (2011). Heart disease and stroke statistics--2012 update: a report from the American Heart Association. *Circulation*, 125, e2–e220.
- Rouillard, A. D., & Holmes, J. W. (2012). Mechanical regulation of fibroblast migration and collagen remodeling in healing myocardial infarcts. *The Journal of Physiology*, 18, 4585–4602.

- Simpson, D., Liu, H., Fan, T.-H. M., Nerem, R., & Dudley, S. C. (2007). A tissue engineering approach to progenitor cell delivery results in significant cell engraftment and improved myocardial remodeling. *Stem Cells*, 25(9), 2350–7.
- Sobotta, J. (1907). *Atlas and Text-Book of Human Anatomy: Volume III, Vascular System, Lymphatic System, Nervous System and Sense Organs*. (J. P. McMurrich, Ed.) (3rd ed.). Philadelphia: W. B. Saunders Company.
- Stone, P. H., Raabe, D. S., & Jaffe, A. S. (1988). Prognostic significance of location and type of myocardial infarction: independent adverse outcome associated with anterior location. *Journal of the American College of Cardiology*, 11(3), 453–463.
- Thomas, J. A., & Marks, B. H. (1978). Plasma norepinephrine in congestive heart failure. *The American Journal of Cardiology*, 41(2), 233–43.
- Vokonas, P. S., Pirzada, F. A., & Hood, W. B. (1976). Experimental myocardial infarction: XII. dynamic changes in segmental mechanical behavior of infarcted and non-infarcted myocardium. *The American Journal of Cardiology*, 37(6), 853–9.
- Zimmermann, W.-H., Melnychenko, I., Wasmeier, G., Didié, M., Naito, H., Nixdorff, U., ... Eschenhagen, T. (2006). Engineered heart tissue grafts improve systolic and diastolic function in infarcted rat hearts. *Nature Medicine*, 12(4), 452–8.

Chapter 2

Acute, Anisotropic Reinforcement of Left Ventricular Infarcts

Studies of both global and local post-infarction restraint therapies consistently show that ventricular or infarct reinforcement reduces post-MI LV dilation. However, these studies also fail to show sustained improvements in LV function compared to infarct-only controls. Early finite element models of infarct healing anticipated this second finding – they predicted that isotropic stiffening of infarct scars would improve active function by minimizing passive expansion of the scar during systole, but also impair passive function by limiting filling during diastole, leading to no net improvement in stroke volume. We hypothesized that anisotropic infarct restraint may be useful for finessing this trade-off. Specifically, we hypothesized that selectively stiffening an infarct scar in one direction might improve systolic function with minimal deleterious effects on passive filling. Accordingly, a prior study from our laboratory is described below, in which a finite-element model of the infarcted dog heart was used to explore

the impact of infarct anisotropy on LV function. The remainder of the chapter presents an acute animal study testing the model prediction that longitudinal reinforcement can significantly improve LV function following a large anterior infarction. Results from the animal study were published in Fomovsky et al. 2012.

Finite element modeling of infarct stiffening

Over three decades ago, Bogen et al. utilized a simplified finite element model of the infarcted canine left ventricle to simulate the functional impact of changes in infarct material properties over the time course of healing. Modeling scar formation and maturation through increases in scar stiffness, they found an interesting trade-off between the effect of scar stiffening on systolic vs. diastolic function (Bogen, Rabinowitz, Needleman, McMahan, & Abelman, 1980). Simulating acute infarcts as noncontractile regions with material properties identical to passive myocardium, these models predicted normal diastolic behavior (reflected in an unchanged end-diastolic pressure-volume relationship, EDPVR) but severely depressed systolic function (altered end-systolic function pressure volume relationship, ESPVR), in agreement with experiments. Increasing infarct stiffness in the model improved systolic function as expected, shifting the predicted ESPVR back towards baseline. However, hearts with a stiffer infarct also displayed impaired filling, reflected in a left-shifted EDPVR, and reduced filling exactly offset improved ejection, producing no overall change in predicted CO at matched pressures (Figure 2.1).

This early model made a number of simplifications, but recent modeling studies using much more sophisticated and better-validated finite-element models reached similar conclusions. Fomovsky et al. found that isotropically stiffening a large anterior infarct in a model of an infarcted dog heart reduced both systolic and diastolic volumes at

matched pressures, producing no net benefit in overall pump function (Fomovsky, Macadangdang, Ailawadi, & Holmes, 2011). Similarly, Dang et al. studied the impact of the stiffness of an isotropic patch applied in a simulated Surgical Anterior VEntricular Restoration (SAVER) operation, and found that increasing patch stiffness reduced systolic and diastolic volumes at matched pressures, but actually decreased SV – in this setting, stiffer patches impaired filling more than they improved ejection (Dang et al., 2005). Overall, these computational studies are remarkably consistent with the majority of the experimental studies of global and local infarct reinforcement. We hypothesize that stiffer patches or restraints are likely to be more effective in reducing or limiting LV size, but that isotropic therapies are unlikely to directly improve LV pump function, regardless of stiffness.

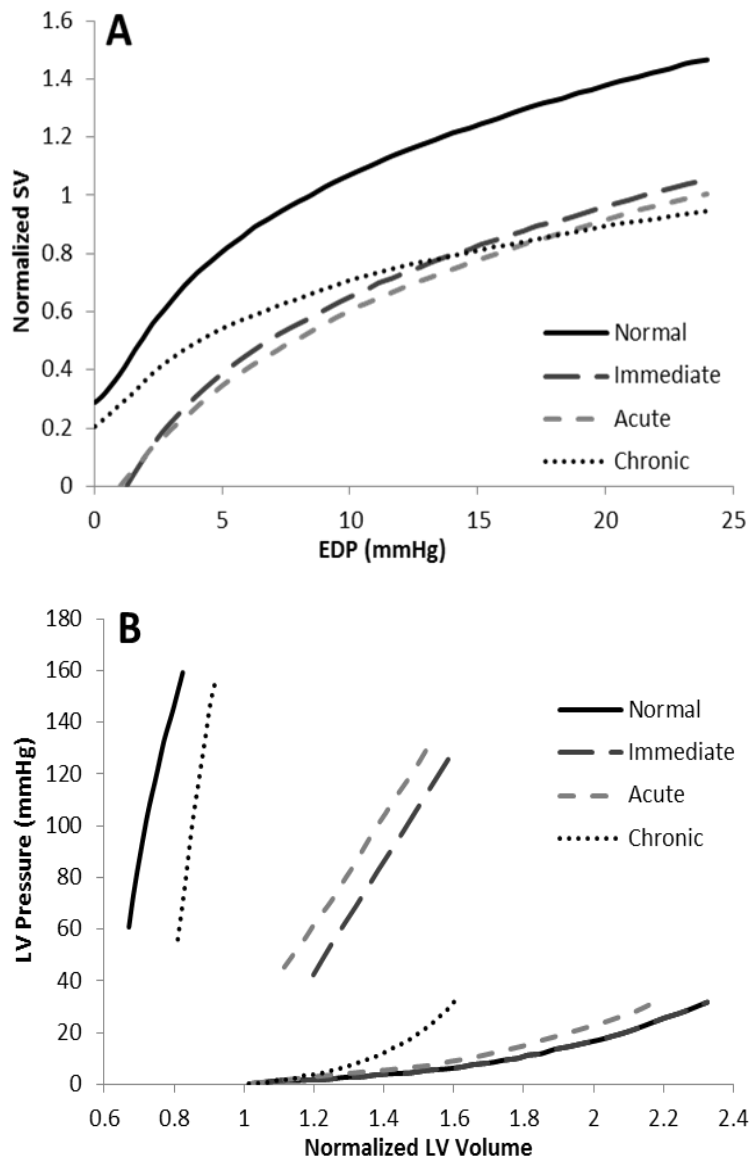


Figure 2.1 Computationally generated (A) LV function curves and (B) pressure-volume curves for normal myocardium and three stages of infarct healing. P-V analysis shows dramatic shifts in the ESPVRs of immediate and acute infarcts, with minimal changes in the EDPVRs. Chronic scars exhibited a leftward shift in the ESPVR accompanied by an increase in the slope of the EDPVR. These shifts led to minimal net change in LV function, as all infarct models showed similar functional depression compared to the baseline model. Normalized volumes are relative to the initial reference volume in the simulation. Recreated with data from Bogen et al. 1980.

Optimizing local restraint

The computational models and experiments described above provided convincing evidence that isotropic stiffening or reinforcement provides little functional benefit. Interestingly, our laboratory has found that some animal models form infarct scars with anisotropic collagen structure and material properties. We therefore considered whether anisotropy might have functional benefits. To explore the utility of anisotropic infarct stiffening as a post-MI therapy, Fomovsky et al. constructed a bi-ventricular canine finite element model (Fomovsky et al., 2011). They simulated a large infarct on the anterior wall and apex of the LV, similar to those arising from ligation of the LAD. Acute infarcts were assumed to have the same material properties as passive myocardium, followed by imposition of varying magnitudes of circumferential and longitudinal infarct reinforcement. Reinforcement was simulated by modifying the circumferential and longitudinal stiffness coefficients in the passive infarct region. The EDPVR was generated by passive inflation of the LV cavity, and the ESPVR was mapped out using several simulations of isovolumic contractions from different starting pressures. To quantify the net effects of each stiffness combination on LV function, stroke volume of each model was calculated between matched values of EDP and ESP. As seen in Figure 2.2, a combination of high longitudinal and low circumferential stiffness led to the highest predicted SV. Compared to a baseline (uninfarcted) SV of 15.7ml and an ischemic SV of 7.6ml, the maximum observed SV of 10.1ml in the longitudinally stiff scar model represents a 30% recovery of the functional deficit caused by the infarct. The results of this model were also consistent with previous finite element and experimental reports of isotropic reinforcement: isotropically stiffening the scar led to minimal or no improvement in SV.

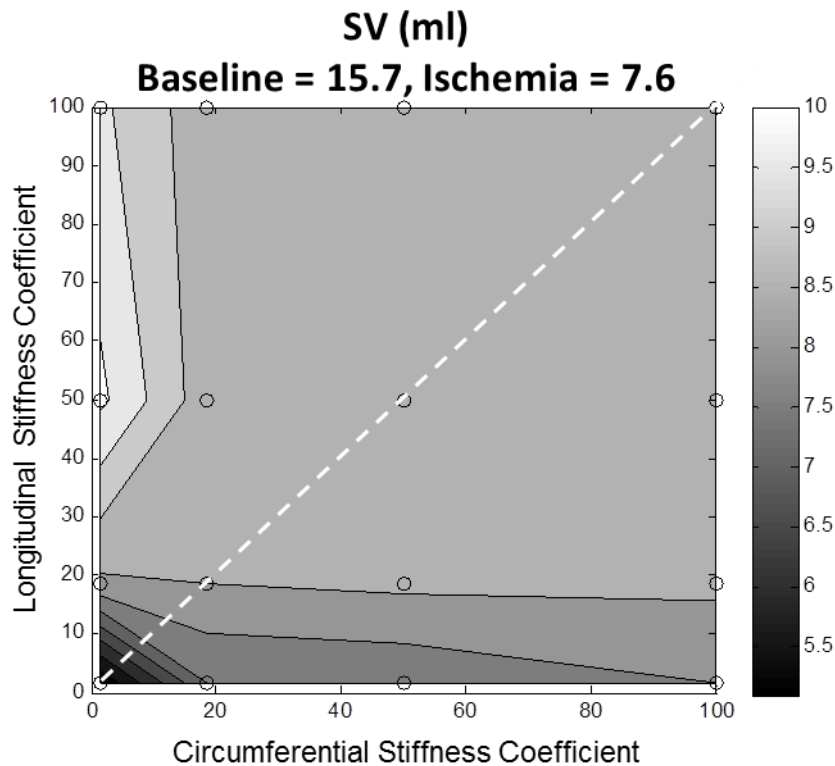


Figure 2.2 Predicted stroke volume from a finite element model of a canine heart. SV (in ml) in the acute LV infarct model dropped to 7.6 ml (from 15.7 ml at baseline). Plotted are predicted values of SV for varying combinations of circumferential and longitudinal infarct stiffness. SV is maximized in the area of low circumferential and high longitudinal stiffness (near the top left corner). The dotted white line represents an isotropic increase in infarct stiffness, along which minimal improvement in SV is observed. Recreated with data from Fomovsky et al. 2011.

Methods to test acute longitudinal infarct reinforcement *in vivo*

The functional effects of local, longitudinal infarct restraint were then tested in a canine model of acute infarction. This study was approved by the University of Virginia Animal Care and Use Committee. Twenty-two mongrel dogs were anesthetized with sodium pentobarbital, intubated, and ventilated with room air. The chest was opened with a left lateral thoracotomy, and the heart was suspended in a pericardial cradle. The left anterior descending coronary artery was dissected free for ligation between the first and second diagonal branches. Finally, a snare was placed around the inferior vena cava (IVC) to allow for temporary reductions in LV preload.

LV pressure was monitored using a Millar pressure catheter (Mikro-Tip SPC-454D; Millar Instruments, Houston, TX) inserted into the LV cavity via the left carotid artery, arterial pressure was measured using a fluid-filled manometer in the femoral artery, and ascending aortic flow velocity was measured with an ultrasonic flow probe (A20; Transonic Systems, Ithaca, NY). Sonomicrometer crystals (2T-36S-40-RS; Sonometrics, London, Ontario, Canada) were inserted into the LV midwall to measure changes in global cavity and local infarct dimensions. Three pairs of crystals were used to track the apex-base, anterior-posterior, and septal-lateral dimensions of the LV. An additional 4 crystals were placed on the anterior midwall in the region of anticipated ischemia, to quantify changes in ischemic segment lengths. LV pressure, arterial pressure, aortic flow, and sonomicrometer pair distances were all recorded in SonoSoft (Sonometrics, London, Ontario, Canada).

During the study, each set of data collected consisted of at least five consecutive normal beats, followed by a series of beats over which LV preload was gradually reduced via temporary IVC occlusion. Baseline data were recorded prior to administering a

pharmacologic blockade of reflex changes in contractility, and data from these pre-blockade baseline runs are used for comparison to infarcted animals in Chapter 3. Following baseline runs, the baseline response to temporary β -adrenergic stimulation was measured by injection of a 2.5 μ g/kg bolus of Dobutamine (Db). Once heart rate and inotropic state returned to near baseline values, a neurohumoral blockade was administered. Compensatory sympathetic and parasympathetic changes in heart rate and myocardial contractility were blocked with 2 boluses each of propranolol (2mg/kg) and atropine (0.2mg/kg). Blockade effectiveness was then confirmed through injection of a second Db bolus (2.5 μ g/kg) to verify that no increases in heart rate or myocardial contractility were observed. A second set of baseline measurements were saved post-blockade, and these data were used as the baseline reference for comparison to all other runs in the experiment.

Ischemia was induced by permanent ligation of the LAD, immediately distal to the first diagonal, in addition to ligation of any collateral vessels supplying the desired ischemic region. Development of ischemia was monitored visually during a 45 minute open-chest ischemic period, during which hemodynamic data (without IVC occlusion) were recorded every five minutes. During this period, 11 out of 22 animals were given lidocaine (10 mg) to reduce arrhythmias and 7 out of 22 animals required defibrillation. At the end of 45 minutes, a full ischemic data run was recorded to be used for analysis. To generate infarct reinforcement, a Dacron patch (Hemashield Knitted Double Velour Fabric; Maquet Cardiovascular LLC, Wayne, NJ) was trimmed to size and sutured onto the epicardial surface, directly over the infarct area. The center of the patch was modified to include 6 parallel slits, which were sutured closed prior to the beginning of the study. The patch was applied to the infarct with the slits aligned longitudinally (parallel to the apex-base axis), using a running suture around the entire patch perimeter. To generate selective longitudinal reinforcement, the patch was applied

under as much tension as possible in the longitudinal direction and no applied tension in the circumferential direction. Two patch configurations were explored: a mechanically isotropic patch applied under longitudinal tension, and a mechanically anisotropic patch applied under longitudinal tension. Upon initial patch application, the longitudinal slits were sewn shut and the patch was mechanically isotropic. Following data recordings, the patch was left in place and the slit sutures were cut, so that the patch could deform freely in the circumferential direction (perpendicular to the slits). Anisotropic patch data were collected in this configuration, in which the direction of patch stiffness was aligned with the direction of applied tension. Prior to study completion, the patch was removed for a final “patch off” data set, to verify that no significant deterioration of function occurred between the initial ischemic run and subsequent patch runs. At the end of the experiment, animals were euthanized with 10ml of Euthasol. Hearts were excised and weighed, and sonomicrometer crystal locations were photographed for strain analysis.

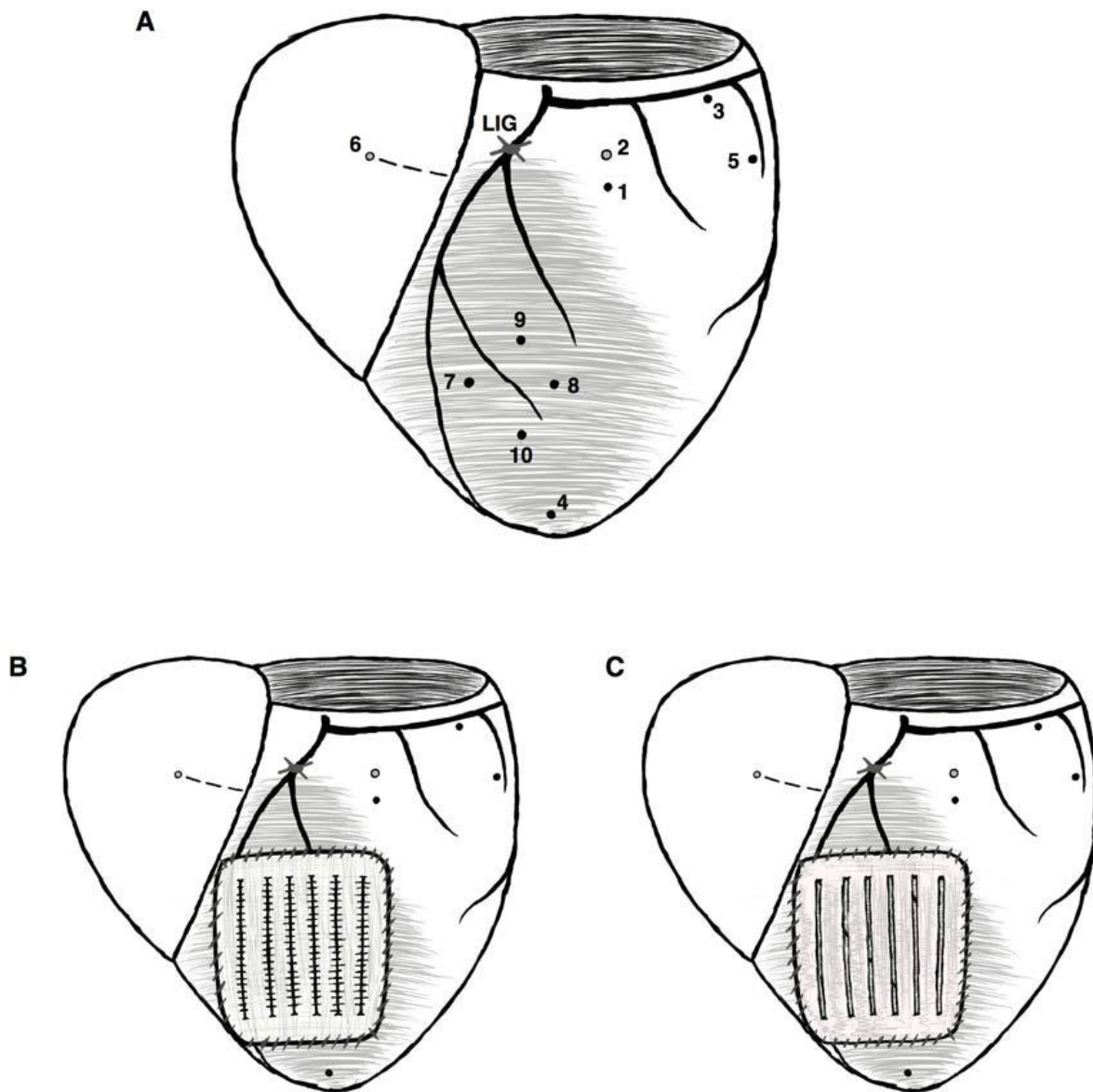


Figure 2.3 Schematic of infarct reinforcement. (A) Sonomicrometer crystals were placed on the anterior wall in the anticipated region of LAD infarction. The patch was applied to epicardium of the infarct using a running suture along all four edges. (B) Isotropic and (C) anisotropic patches were both applied under as much longitudinal tension as possible. Diagram from Fomovsky 2010.

Methods to analyze hemodynamics

Hemodynamic data were filtered to remove noise and exported from SonoSoft as text files. Analysis of global pressure-volume and local strain behavior was done in MATLAB using a set of custom scripts. For each run analyzed, quantification of local strains and determination of raw hemodynamic parameters was done using five beats preceding the start of the IVC occlusion. From these beats, all raw hemodynamic values are reported as the average across all five beats, except the rate of LV pressure generation (dP/dt) which is reported as the maximum. Generation of SV or CO curves and interpolation of functional parameters was done using the full range of IVC occlusion data. For each cardiac cycle, end-diastolic and end-systolic indices were selected manually in MATLAB. LV volumes were calculated from the global sonomicrometer crystal pairs by assuming that the LV cavity is a truncated ellipse. Since the crystals were implanted in the midwall, the calculated volume actually reflects the sum of the cavity volume and an unknown fraction of the LV wall volume. However, since the myocardium is virtually incompressible, the added wall volume can be assumed to be a constant. Stroke volume was computed by integrating the aortic flow signal between subsequent ED indices. Retrograde flow measured in the ascending aorta reflects flow into the coronary circulation, and was neglected in SV calculations (Steingart et al., 1980). Although SV could be calculated from either the LV volume trace or the aortic flow trace, deviation from the assumed truncated ellipsoid shape following infarction makes the estimation of systolic LV volumes from sonomicrometers less reliable. Therefore, all calculations of SV and CO were performed using the aortic flow data, and end-systolic volume was computed as $EDV-SV$.

To control for variability in LV preload between states, LV volumes and CO were calculated at matched values of EDP. For each occlusion, lines were fit to the ESPVR, to

the log transformed EDPVR ($\ln(\text{EDP})$ vs. EDV), and the log transformed CO curve. Values of EDV were linearly interpolated at a pressure of 12mmHg, values of ESV at a pressure of 85mmHg. For each animal, CO was interpolated across states at that animal's baseline value of EDP. Interpolation pressures were chosen to minimize extrapolation across all animals. Fitted curves and interpolated volumes were used to compare average function in each state (baseline, ischemia, longitudinal patch) across animals. Worsening of LV function was quantified as a rightward shift in the Starling curve (CO vs. EDP) between baseline and ischemia.

Methods to analyze regional deformation

Local infarct strains were calculated from the sonomicrometer crystal pairs placed on the anterior wall. Postmortem photos of the LV were used to measure the angles of each crystal pair relative to the circumferential and longitudinal axes of the LV. Implanting four crystals in the center of the ischemic region led to a total of six possible crystal pairs/segment lengths. A minimum of three segment length traces were used to compute strains, although additional segment lengths were used whenever possible, depending on the amount of noise in each trace. Strains were computed between ED and ES by interpolating segment lengths at matched pressures, using a process similar to the one used to interpolate systolic and diastolic volumes. Remodeling strains were also computed at a matched EDP of 12mmHg to capture changes in ischemic region dimensions relative to baseline. Since remodeling strains are zero at baseline by definition, the effect of ischemia was tested using a one-sample t-test against a hypothetical mean of zero. For all other comparisons, one-way ANOVA with Newman-Keuls post-hoc tests was used to detect differences between each state (baseline, ischemia, isotropic patch, anisotropic patch), and a cutoff of $p < 0.05$ was used as the threshold for significance in all tests.

Results

Of the 22 animals that underwent LAD ligation surgery, 10 animals were included in the final analysis group. Of the remaining 12, 8 animals were excluded because no shift in the CO curve between baseline and ischemia was observed, 3 did not survive the 45 minute ischemic period, and 1 animal was excluded because of data acquisition problems during the study.

Average hemodynamics across the four states tested are shown in Table 2.1. Since responses to β -adrenergic stimulation were blocked pharmacologically, heart rate and maximum LV pressure generation remained constant across all states and hemodynamic compensation following LAD ligation occurred primarily through the Frank-Starling mechanism. Ischemic EDP, EDV, and ESV were all elevated relative to baseline. Reinforcement with either patch configuration led to significant decreases in LV volumes.

Table 2.1 Hemodynamics

Parameter	Baseline	Ischemia	Isotropic	Anisotropic
EDP (mmHg)	11.3±4.3	17.3±6.1 [†]	15.8±7.2	15.9±7.5
EDV* (ml)	78.2±15.5	89.0±18.0 [†]	82.8±17.1 [†]	82.2±16.2 [‡]
ESP (mmHg)	96.1±14.8	94.7±14.3	91.4±9.3	92.2±9.7
ESV* (ml)	62.7±13.5	75.0±17.7 [†]	68.0±16.0 [†]	66.8±15.4 [‡]
SV (ml)	15.5±3.8	14.0±3.9	14.8±4.2	15.4±3.5
HR (bpm)	108±10	109±15	110±13	111±15
CO (L/min)	1.69±0.51	1.54±0.54	1.64±0.51	1.70±0.44
max dP/dt (mmHg/s)	1227±337	1220±431	1302±299	1342±249

Hemodynamic data from 10 dogs that showed a shift in cardiac output curve 45 minutes after coronary ligation. Dogs were pretreated with propranolol and atropine to prevent reflex changes in heart rate and intrinsic myocardial contractility and LAD occlusion; by design, end-systolic pressure (ESP), heart rate (HR), and maximum dP/dt did not vary significantly during the experiment. During Ischemia, animals compensated for reduced systolic function via the Frank-Starling mechanism, increasing end-diastolic pressure (EDP) and volume (EDV) to maintain stroke volume (SV) and cardiac output (CO) despite increased end-systolic volume (ESV). Anisotropic surgical reinforcement significantly reduced EDV and ESV. *Midwall volumes include cavity volume and approximately half the LV wall volume. [†]P<0.001 vs. baseline; [‡]P<0.001 vs. ischemia.

Examination of LV pressure-segment length loops showed active shortening on the anterior wall in the circumferential and longitudinal directions at baseline (Figure 2.4). After 45 minutes of ischemia, segments in both directions transitioned from active contraction during systole to passive stretching throughout the entire cardiac cycle. Segment lengths in both directions also got longer, as indicated by a rightward shift in the ischemic curve. Both patch configurations generated approximately a 10% reduction in longitudinal segment lengths with minimal effect on the circumferential direction.

Similar trends were observed in remodeling strains, reflecting changes in the end-diastolic dimensions relative to baseline (Figure 2.5). Ischemic strains indicated significant infarct expansion in both directions. Patch application was observed to significantly decrease infarct segment lengths in both directions, although the average magnitude of the reduction was over six times greater in the longitudinal direction. Additionally, anisotropic tension in both patch types was sufficient to selectively reduce longitudinal segment lengths to shorter than their baseline values. Systolic strains, reflecting segment length deformation between end diastole and end systole, were negative at baseline due to active contraction of the myocardium during systole (Figure 2.5). All post-MI systolic strains were positive, indicating a loss of contraction and passive infarct stretching in response to systolic LV pressures. Compared to ischemia, patch application did not produce any changes in longitudinal strains, but led to a significant increase in circumferential stretching at end systole.

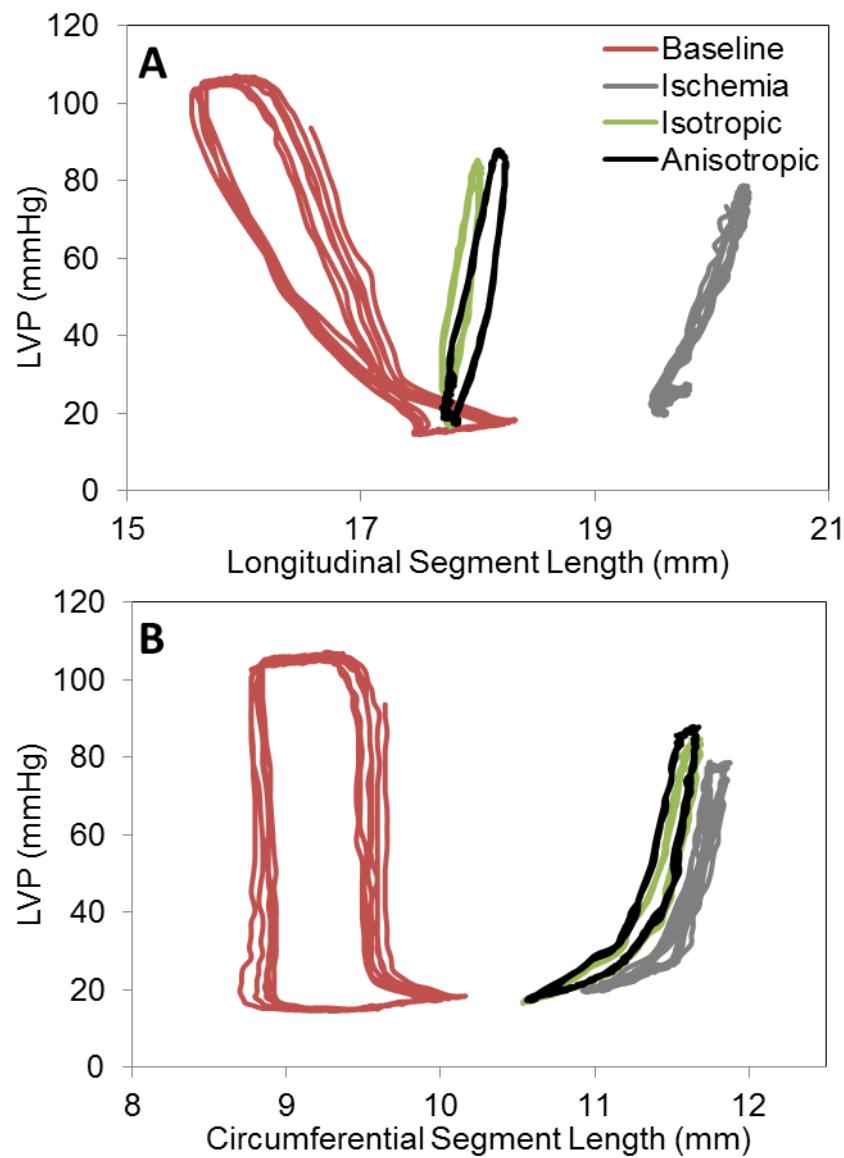


Figure 2.4 Changes in infarct segment lengths with patch reinforcement in one animal. Regardless of patch material properties, longitudinal tension resulted in a decrease in (A) longitudinal segment lengths with minimal effects on (B) circumferential segments.

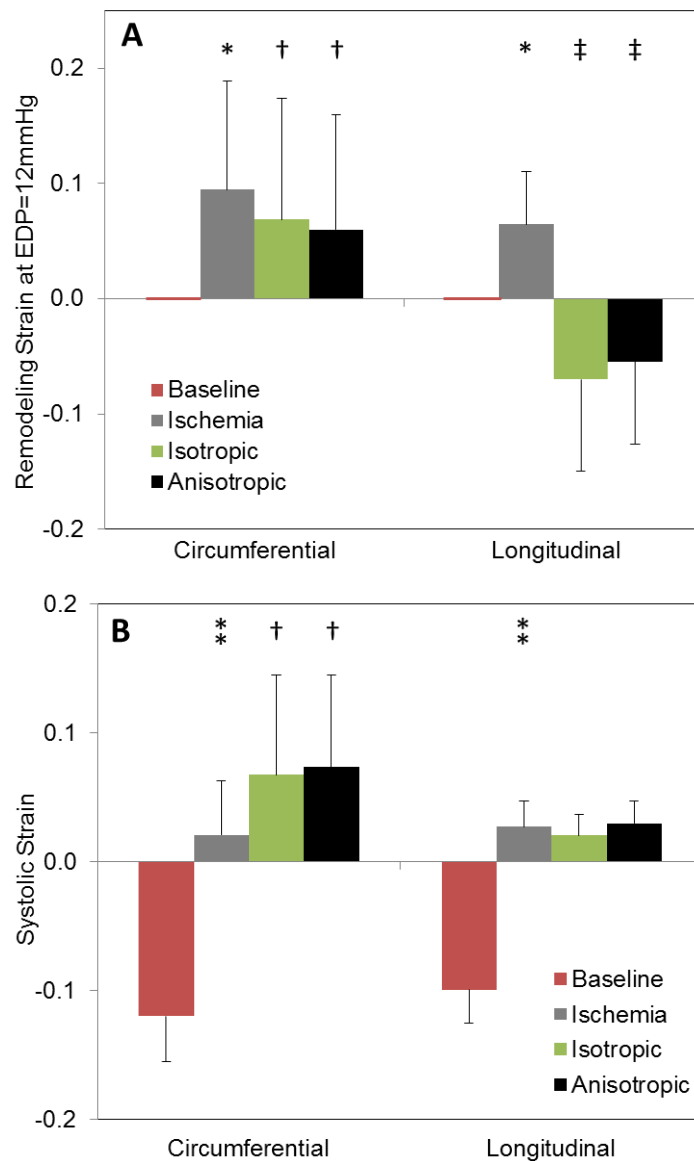


Figure 2.5 (A) Remodeling strains reflecting changes in end-diastolic infarct dimensions relative to baseline show acute infarct expansion in both directions. Longitudinal restraint with both patch types reduces segment lengths in the longitudinal dimension to shorter than at baseline. (B) Systolic strains, calculated between ED and ES, are negative at baseline (reflecting active shortening) and become positive in ischemia (passive stretching). Patch application caused a slight increase in circumferential stretching but no change in the longitudinal direction. * $p < 0.05$ v. baseline, ** $p < 0.001$ v. baseline, † $p < 0.05$ v. ischemia, ‡ $p < 0.001$ v. ischemia.

The end-diastolic and end-systolic pressure volume relationships were averaged across animals for each state (Figure 2.6). As expected, infarction caused a substantial rightward shift in the ESPVR with minimal change in slope. Longitudinal restraint with either patch caused the ESPVR to shift leftward toward the baseline curve. Minimal changes in passive behavior were observed across all four conditions. To control for differences in LV preload, LV volumes were interpolated from the average curves at matched ED and ES pressure of 12 and 85mmHg, respectively (Figure 2.6). There was no significant change in EDV between baseline and ischemia at matched EDP, while ischemic ESV was significantly increased at matched ESP. Compared to ischemia, ESV was significantly reduced with both types of patch reinforcement, while only the isotropic patch caused a significant change in EDV.

Shifts in the average cardiac output curves showed the same trends as the average ESPVRs (Figure 2.7). Relative to baseline, ischemia induced a substantial rightward shift in the ESPVR. Longitudinal restraint with either patch shifted the entire curve leftward towards baseline, indicating restoration of some of the functional deficit caused by infarction. Quantifying these shifts by comparing CO at baseline EDP again showed a substantial reduction in CO following infarction (2.08 ± 0.7 L/min baseline, 1.48 ± 0.72 L/min ischemia) (Figure 2.7). The two patch configurations restored 40% (isotropic, to 1.72 ± 0.73 L/min) and 60% (anisotropic, to 1.84 ± 0.84) of the functional deficit between baseline and ischemia. Although application of either patch appeared to cause an increase in CO relative to ischemia, only the change induced by the anisotropic patch configuration was significant.

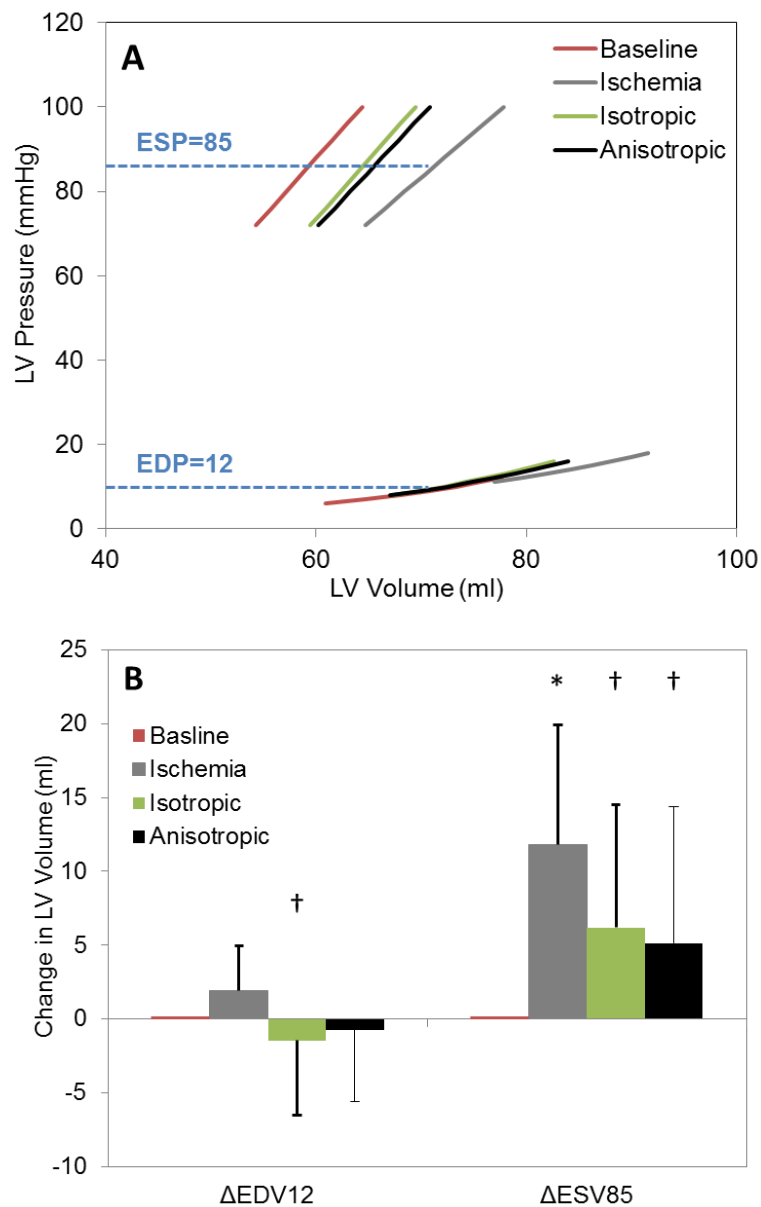


Figure 2.6 (A) The average ESPVR showed a large rightward shift between baseline and ischemia, as expected. Application of either patch shifted the active curve leftward toward the baseline curve, with minimal effects on the passive curve. (B) Interpolating changes in volumes at matched EDP and ESP, however, did reveal decreases in both EDV and ESV (dotted blue lines in (A)) with both patch types. * $p < 0.05$ v. baseline, † $p < 0.05$ v. ischemia.

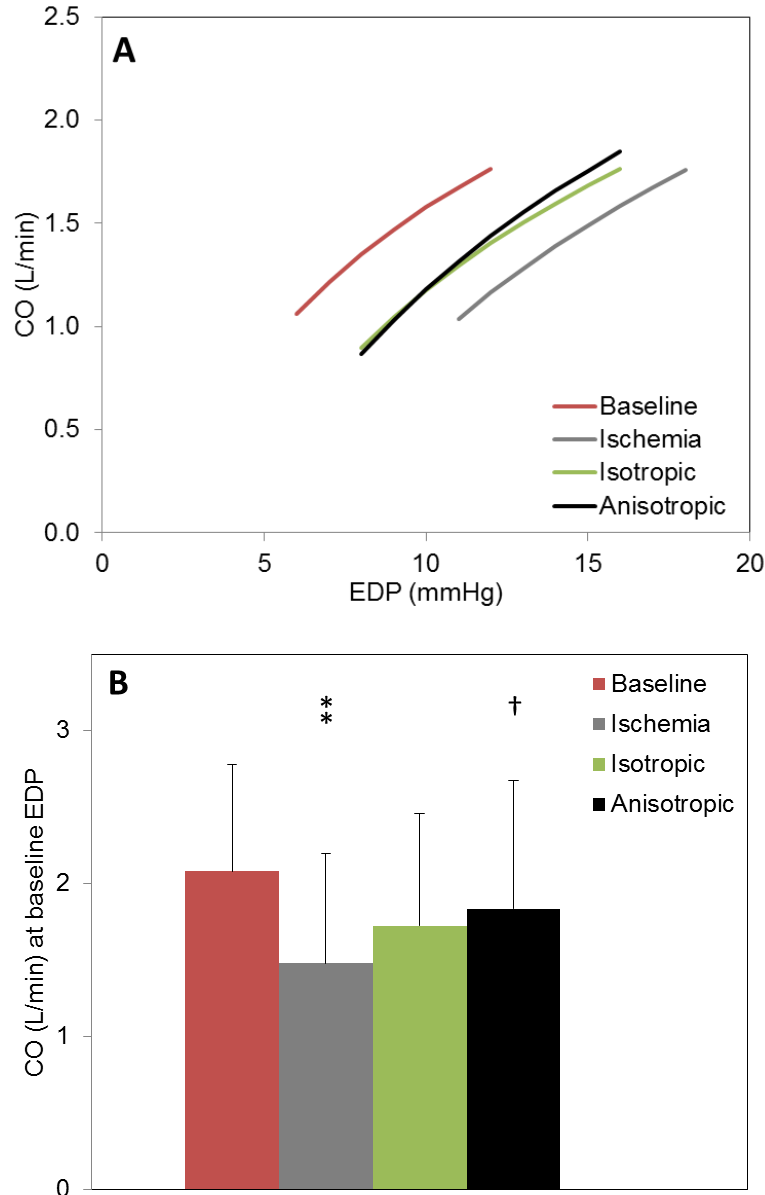


Figure 2.7 (A) Starling curves comparing LV function across states. The curve shifts right between baseline and ischemia (a higher pressure is needed to generate the same CO) and then leftward back towards baseline with reinforcement. (B) Interpolated CO (at the baseline EDP of each animal) decreased in ischemia and then increased in both patch conditions, although only CO with the anisotropic patch was significantly greater than ischemia. ** $p < 0.001$ v. baseline, † $p < 0.05$ v. ischemia.

Discussion

In this study, we used a canine model of acute MI to measure the functional effects of anisotropic infarct restraint. Since the properties of acute infarcts mirror those of passive myocardium, they stretch and bulge instead of contracting during systole, leading to impaired active LV function. Although isotropic infarct stiffening or reinforcement has been shown to ameliorate some of this systolic dysfunction, isotropically stiff infarcts also restrict diastolic filling and therefore produce no net improvement in LV function. Therefore, we examined two strategies for generating longitudinal restraint of an acute, anterior infarct: an isotropic material under anisotropic tension, and an anisotropic material under anisotropic tension. We observed functional depression in the data from 10 of 22 animals, as indicated by a rightward shift in the CO curve between baseline and 45 minutes of ischemia. As expected, this shift was accompanied by a rightward shift in the ischemic ESPVR, indicating that the LV can only eject a fraction of the normal SV at any level of preload. Overall, we observed that either approach for generating selective infarct restraint in the longitudinal direction led to substantial improvement in systolic function with minimal effect on passive filling.

Locally, longitudinal infarct reinforcement reduced longitudinal segment lengths across the cardiac cycle with minimal effects in the circumferential direction. Effects on ED and ES dimension were examined individually through remodeling and systolic strains. Remodeling strains exhibited dramatic reductions in the longitudinal direction at ED, so that reinforced segment lengths were shorter than at baseline. Although remodeling strains also indicated a reduction in circumferential dimension at ED, systolic strains in the circumferential direction increased with reinforcement. Patch application appears to have induced a significant increase in ES circumferential stretching by reducing ED

longitudinal segment lengths while simultaneously preventing an increase in longitudinal stretching.

Globally, both reinforcement approaches produced dramatic improvements in LV function. Shifts in the average EDPVR and ESPVRs suggest that longitudinal infarct restraint was able to reverse a significant amount of post-MI systolic dysfunction with minimal effects on passive filling. Changes in both LV function curves and interpolated CO values indicated severe depression of function in ischemia, followed by recovery of approximately half of the deficit after longitudinal reinforcement. Overall, both the local and global effects of these two approaches for generating longitudinal restraint yielded remarkably similar outcomes. Although the anisotropic patch led to slightly greater improvement in interpolated CO compared to ischemia, there were no significant differences between the two patches in any of the parameters measured. Overall, the results of this study suggest that selective, anisotropic tension in the longitudinal direction improves post-MI LV function.

Conclusion

This study was successful in evaluating the efficacy of longitudinal infarct restraint in improving LV function acutely post-MI. However, this study only examined the short-term effects of anisotropic reinforcement. Additionally, to isolate changes in LV pump function, all studies were performed following administration of a pharmacologic blockade to prevent reflex changes in heart rate and inotropic state. From this study, it is still unclear how the functional improvement with longitudinal restraint would alter hemodynamics and neurohormonal state. Additionally, the long-term effects of anisotropic reinforcement on LV remodeling and chronic function remain unknown.

References

- Bogen, D. K., Rabinowitz, S. A., Needleman, A., McMahon, T. A., & Abelmann, W. H. (1980). An analysis of the mechanical disadvantage of myocardial infarction in the canine left ventricle. *Circulation Research*, 47(5), 728–41.
- Dang, A. B. C., Guccione, J. M., Zhang, P., Wallace, A. W., Gorman, R. C., Gorman, J. H., & Ratcliffe, M. B. (2005). Effect of ventricular size and patch stiffness in surgical anterior ventricular restoration : a finite element model study. *Annals of Thoracic Surgery*, 79, 185–193.
- Fomovsky, G. M. (2010). *Scar Structure, Mechanics, and Ventricular Function in Healing Myocardial Infarction*. Columbia University.
- Fomovsky, G. M., Clark, S. A., Parker, K. M., Ailawadi, G., & Holmes, J. W. (2012). Anisotropic reinforcement of acute anteroapical infarcts improves pump function. *Circulation Heart Failure*, 5, 515–522.
- Fomovsky, G. M., Macadangdang, J. R., Ailawadi, G., & Holmes, J. W. (2011). Model-based design of mechanical therapies for myocardial infarction. *Journal of Cardiovascular Translational Research*, 4(1), 82–91.
- Steingart, R. M., Meller, J., Barovick, J., Patterson, R., Herman, M. V, & Teichholz, L. E. (1980). Pulsed doppler echocardiographic measurement of beat-to-beat changes in stroke volume in dogs. *Circulation*, 62(3), 542–548.

Chapter 3

Chronic, Anisotropic Reinforcement of Left Ventricular Infarcts

Global and local cardiac restraint devices have been used following myocardial infarction to limit left ventricular dilation post-MI. In our review of infarct reinforcement, we found surprising consistency across a variety of studies showing that local restraint can limit post-MI LV dilation. However, isotropic restraint approaches have not been shown to directly improve post-MI ventricular function. Chapter 2 describes our study showing that anisotropic reinforcement of acute infarcts dramatically improves LV pump function. We found that longitudinal restraint of anterior infarcts can produce a 60% recovery of the functional deficit due to ischemia. Therefore, we hypothesized that our local, anisotropic therapy might also be effective in limiting post-infarction dilation. Specifically, we hypothesized that improving post-MI function with longitudinal infarct restraint would limit LV dilation, improve chronic LV function, and alter the structure of the resulting collagenous infarct scar.

Post-MI function and remodeling

Every year, there are almost 1 million new or recurrent MIs in the United States alone (Go et al., 2013). Due to improvements in the administration of acute therapies, mortality rates due to acute MI have dramatically declined over the past several decades (10.4% to 6.3%, 1990-2006) (Go et al., 2013; Roger et al., 2011). As a result, there are more patients living with a previous MI now than ever before. Unfortunately, ventricles containing large regions of infarct scar often undergo pathological remodeling in the long term, characterized by ventricular dilation that is indicative of heart failure (Bristow et al., 1982; Thomas & Marks, 1978). Therefore, in addition to minimizing both acute and chronic functional depression, preventing the development of post-MI heart failure is an increasingly urgent clinical goal. In an *in vivo* study, we showed that local, anisotropic reinforcement of an acute infarct using an epicardial patch dramatically improved LV function following a large MI (Fomovsky, Clark, Parker, Ailawadi, & Holmes, 2012). However, the chronic effects of local, anisotropic restraint on LV function and remodeling are unknown. The goal of this study was to test the effects of local, anisotropic infarct reinforcement on chronic LV function, remodeling, and progression to heart failure.

Methods to test chronic, longitudinal infarct reinforcement *in vivo*

A canine model of non-reperfused MI (Jugdutt, 2002) was used to test the effects of chronic longitudinal reinforcement applied on the epicardial surface. Experimental group sizes (n=15) were powered to detect a similar reduction in post-MI LV dilation as observed with post-MI ACE-inhibitor treatment in dogs (Jugdutt, Schwarz-Michorowski, & Khan, 1992). 48 male mongrel dogs weighing 25-33kg were anesthetized with sodium pentobarbital and subjected to a left thoracotomy. MI was

induced by permanent ligation of the left anterior descending coronary artery, producing a large infarct on the anterior wall and apex of the LV. In patch animals, a longitudinally inextensible patch was sutured to the epicardial surface over the infarct at the end of the 45 minute open-chest ischemic period. The patch was applied under longitudinal tension, similarly to our acute studies which demonstrated that this approach induces a 10% decrease in longitudinal segment lengths throughout the cardiac cycle, without altering circumferential segment lengths (Figure 2.4).

48 hours after MI induction, animals underwent an MR scan to evaluate acute myocardial viability and baseline ventricular geometry. CINE MR was used to measure LV cavity volumes and late-gadolinium enhancement to measure infarct size (Kim et al., 1999; Shapiro et al., 1989). The same imaging protocol was repeated again 8 weeks post-MI. Hemodynamic data were collected during a terminal study following the final MR scan. The chest was opened via midline sternotomy and dogs were instrumented with a Millar conductance catheter (Millar Instruments, Houston, TX) to measure LV pressure and volume and an ultrasonic flow probe (A20, Transonic Systems, Ithaca, NY) was placed around the aorta to measure aortic flow. LV pressure and cavity volume were recorded in Lab Chart 7 (Ad Instruments), while aortic flow velocity was recorded in SonoLab DS3/SonoSOFT (Sonometrics Corporation). LV preload was varied by temporary occlusion of the inferior vena cava in order to collect data across a range of filling pressures. Dobutamine was administered intravenously ($5\mu\text{g}/\text{kg}/\text{min}$) to evaluate the ability of the viable myocardium to respond to β -adrenergic stimulation (Bristow et al., 1982; Fowler, Laser, Hopkins, Minobe, & Bristow, 1986; Ginsburg et al., 1983). Dogs were then euthanized with an intravenous bolus of Euthasol. Hearts were excised immediately and underwent retrograde perfusion with a cold solution of 2,3 butanedione-monoxime in phosphate buffered saline.

Methods to measure myocyte size in the remote myocardium

Histology in the remote myocardium was performed to detect effects of the patch on remaining viable muscle. Remote tissue was harvested from the posterior LV midwall and fixed in 10% formalin. Tissue blocks were embedded in paraffin and 7 μ m sections were cut from blocks in two perpendicular orientations to measure myocyte cross-sectional area (CSA) and length (Figure 3.1). For each orientation, sections from 5 different depths in the block were saved for staining, and the distance between each depth was sufficient to ensure that the same cells were not double counted in either the CSA or length measurements. The distances required between depths were estimated from literature values of myocyte CSA and length: the distance between measurements of myocyte CSA should be greater than the expected length of a cell (Veeraraghavan, Gourdie, & Poelzing, 2014), and the distance between measurements of length should be greater than the anticipated diameter of each cell. Therefore, sections to analyze myocyte CSA were cut from a transmural view with 140 μ m spacing between each depth, while measurements of myocyte length were made from sections cut from a basal view with 35 μ m spacing between depths. Both short and long axis sections were stained with 5 μ g/ml wheat germ agglutinin conjugated to Alexa Fluor 555 to fluorescently label myocyte cell membranes and intercalated discs (Dolber, Beyer, Junker, & Spach, 1992). Slides were imaged on a Nikon Eclipse TE2000-E confocal microscope using 543nm excitation and a 590/50nm emission filter. Short and long axis images were taken using 60x and 20x magnification, respectively.

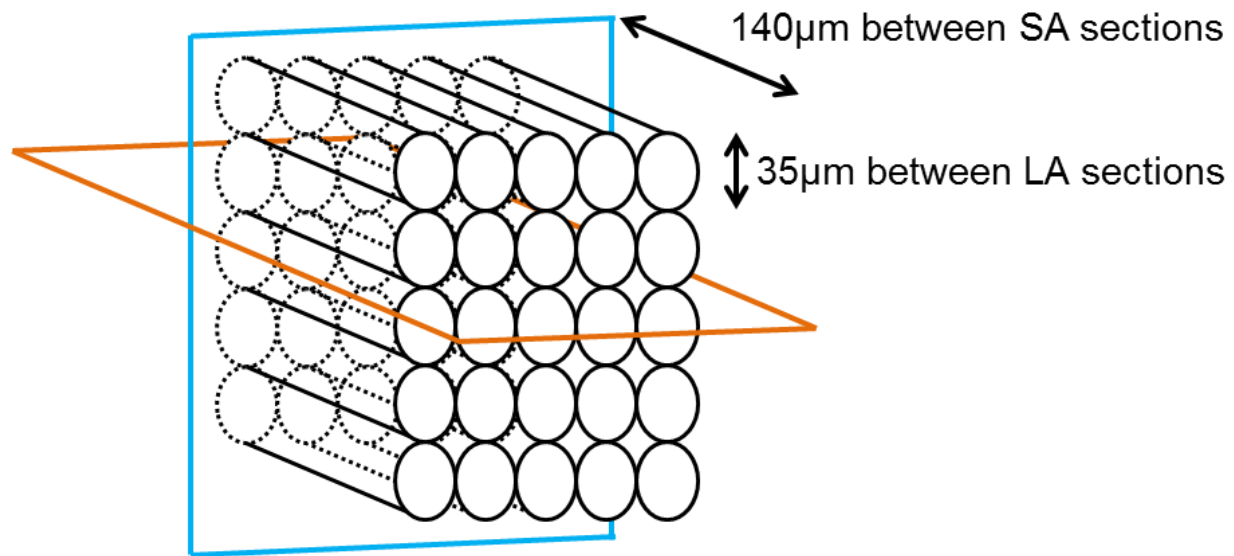


Figure 3.1 Sectioning planes to examine myocyte length and cross-sectional area. A sectioning plane approximately parallel to the base (orange) was used to measure cell length, and a transmural section used to measure CSA. Although myocyte orientation varies transmurally (not shown), these sectioning planes ensured that at least part of the section (near the midwall) contained myocytes either parallel or perpendicular to the plane.

Methods to measure collagen content and alignment in scar

To examine the collagen structure of the infarct, scar blocks were cut from the anterior midwall of the LV, from the center of the scar in control animals and from underneath the center of the patch in patch animals. Blocks were fixed in 10% formalin, embedded in paraffin and sectioned parallel to the epicardial plane. 7 μ m sections were cut from epicardium to endocardium, and 5 sections at transmural depths of 0%, 25%, 50%, 75% and 100% were selected for comparison across animals. Sections were stained with Picrosirius Red (PSR) using a slightly modified protocol to eliminate cytoplasmic staining of any remaining myocytes (Dolber & Spach, 1987; Luna, 1992). A 1.5 x 1.5 mm grid was overlaid on each slide to divide each section into smaller, non-overlapping imaging fields. All imaging fields containing collagen were assigned a number, and 10 field numbers were randomly selected for imaging and analysis. Imaging and analysis of infarct collagen structure was performed using methods that harness the optical birefringence of collagen fibers (Junqueira, Bignolas, & Brentani, 1979). All infarct scar imaging was performed on an Olympus BX51 microscope modified for imaging with circular instead of linear polarized light, which makes fibers in all orientations appear equally bright (Whittaker, Kloner, Boughner, & Pickering, 1994). Therefore, PSR stained collagen fibers appear bright under circularly polarized light and dark red under bright-field illumination. All infarct imaging was done at 10x magnification and captured with a Sony XCD-X710 CCD camera. For each field, the same image was captured twice: once under polarized light and once under bright-field illumination.

Methods to analyze magnetic resonance images

MR images were manually contoured in Segment (v1.9 R2178, <http://segment.heiberg.se>) (Heiberg et al., 2010) and analyzed in MATLAB (R2011b).

Changes in LV cavity, muscle, and scar volumes were calculated from short axis (SA) image stacks according to Simpson's rule,

$$\text{Stack Volume} = \sum \text{Slice Volume} * \text{Slice Thickness}$$

However, differences in SA slice placement between serial MR scans can make small changes in LV volumes difficult to detect. Based on the post MI remodeling data of Jugdutt, we expected an approximate 15% increase in EDV over 8 weeks (Jugdutt et al., 1992). Given the average EDV and number of SA slices in our 48 hour scans, each slice contributed an average of 11% to the total LV cavity volume. Therefore, any shifts in slice location that led to inclusion or exclusion of a SA slice could have resulted in volume errors that were around the same size as the change in volume we were aiming to detect. To combat this, we developed volume adjustments using landmarks in a LA view in addition to the SA stack. Fractional slice volume adjustments were added at the base and apex, according to the strategy shown in Figure 3.2. In a long axis slice, the location of the base was selected as the center of the mitral valve. The most apical point of the endocardium was selected for cavity volume calculations, while the most apical points of both the endocardium and epicardium were selected for wall volume calculations. The distances between the base/apex points and the stack were calculated as the shortest distance from each point to the plane of the nearest SA slice. At the base, the fractional slice was assumed to have the same area as the most basal slice, so the added volume was calculated as,

$$\text{Fractional Slice Volume}_{\text{base}} = \text{Area}_{\text{basal slice}} * \text{Distance}_{\text{base}}$$

At the apex, the additional volume was assumed to taper off in a conical shape. Therefore, added cavity and wall volumes at the apex were determined by,

$$\textit{Fractional Cavity Volume}_{\textit{apex}} = \frac{1}{3} \textit{Cavity Area}_{\textit{apical slice}} * \textit{Endocardial Distance}_{\textit{apex}}$$

$$\textit{Fractional Wall Volume}_{\textit{apex}} = \frac{1}{3} \textit{Wall Area}_{\textit{apical slice}} * \textit{Epicardial Distance}_{\textit{apex}}$$

Muscle volume was calculated by subtracting infarct volume from LV wall volume. Scar compaction dimensions were quantified from gadolinium enhanced SA images. Changes in the circumferential extent and radial thickness were averaged across all scar-containing slices, and longitudinal extent was determined by the distance between SA slices containing scar.

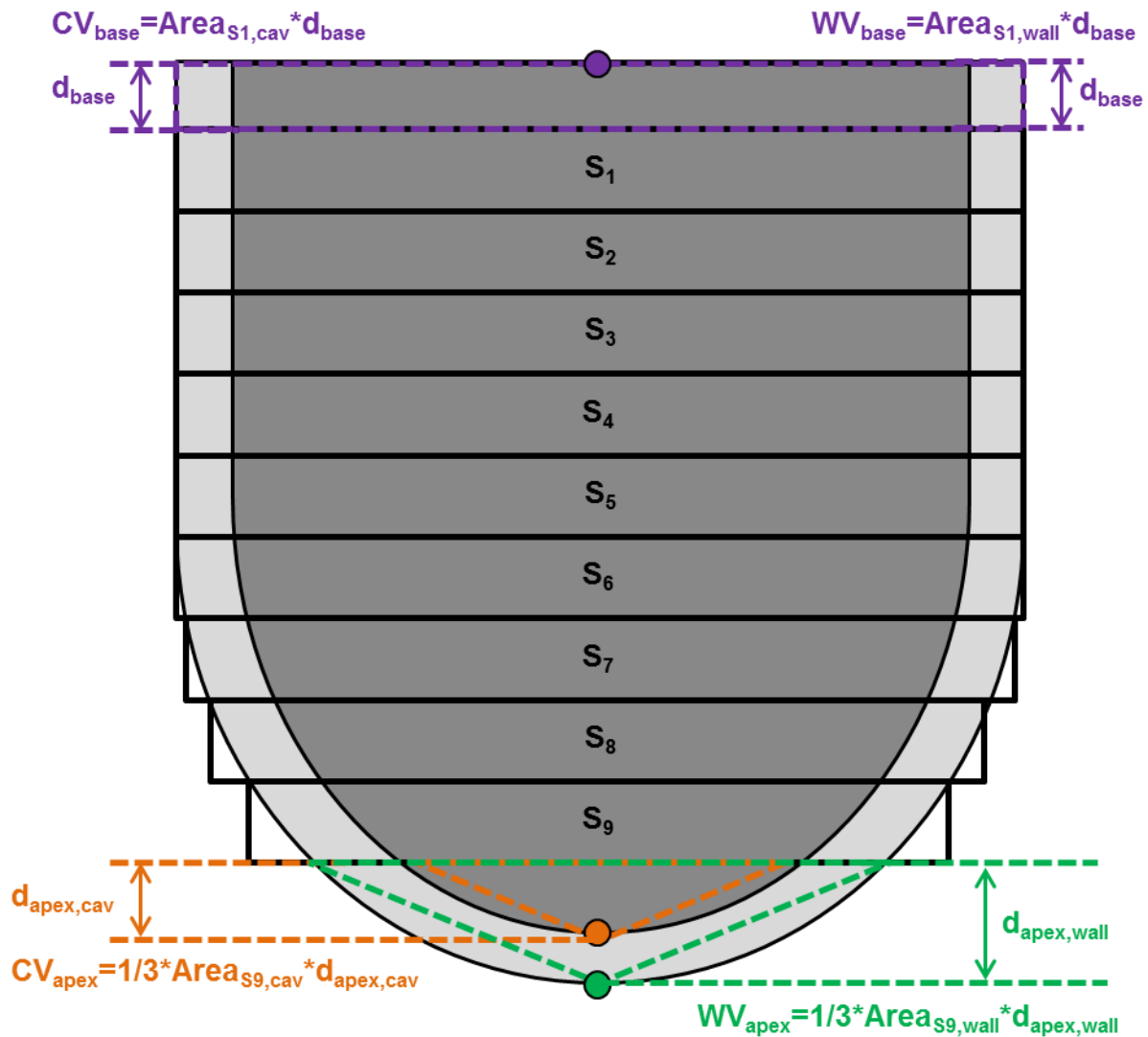


Figure 3.2 Cavity and wall volume adjustments made at the apex and base. “True” base (purple) and apex (orange + green) were selected on a LA image. Cavity and wall volume was added at the base by multiplying the areas of the basal slice by the thickness of the fractional slice between the base point and the top of the stack. Volume was added at the apex assuming a conical tapering of the LV, using the endocardial distance (orange point) to adjust the cavity volume and the epicardial distance (green point) to adjust the wall volume.

Methods to analyze LV hemodynamics

LV pressure, LV volume, and aortic flow traces from the terminal study were exported as text files from the respective acquisition programs. Data from the two systems were manually synchronized in time by selecting the first beat of each recording and aligning the point at which the aortic valve opens on the LV pressure and aortic flow traces. For each occlusion run, end-diastolic and end-systolic indices were selected manually from the pressure recording. The flow velocity signal was integrated between ED indices to determine the stroke volume of each beat, and cardiac output was calculated as the product of stroke volume and instantaneous heart rate. Function curves were generated by plotting SV and cardiac output against EDP, and for each parameter linear interpolation of the log transformed relationship [SV/CO vs. $\ln(\text{EDP})$] was used to calculate SV and CO at a matched EDP of 12mmHg. Average heart rate, the maximum rate of LV pressure generation (max dPdt), and end-systolic elastance (Ees) were calculated to compare contractility between baseline and β -adrenergic stimulated runs. Paired t-tests were used to detect differences between the baseline and post-Db values of each parameter.

Methods to analyze myocyte size and scar structure

In images of the remote myocardium, analysis of myocyte CSA was automated in ImageJ using a custom macro script and analysis of myocyte lengths was done by manually tracing cells in MATLAB. The method for image analysis in the infarct scar is outlined in Figure 3.3. First, each randomly selected imaging field (Figure 3.3A) was captured under circularly polarized and bright field illumination. The circularly polarized (Figure 3.3B) and bright field images were digitally subtracted and thresholded to isolate collagen pixels (Figure 3.3C). The collagen area fraction of each imaging field was calculated as the ratio of collagen pixels to tissue pixels. Analysis of

collagen fiber alignment was done in MatFiber, a custom MATLAB script adapted from the Fiber3 software developed by Karlon (Karlon, Covell, McCulloch, Hunter, & Omens, 1998). In calculations of average distributions, collagen orientation histograms were weighted by collagen area fraction (Figure 3.3D). Wall thickness was determined by the number of sections spanning the wall.

Collagen orientation histograms weighted by collagen content were averaged across animals at five transmural depths: epicardium, 25%, 50%, 75%, and endocardium. Differences in the average mean angle (MA) and mean vector length (MVL) at each depth between groups were examined using one-sample t-tests of the weighted circumferential component, $MVL \cdot \cos(2 \cdot MA)$. Using this approach, the average circumferential component for a group of animals will be 0 if the mean angles are randomly oriented, +1 if angles are circumferentially aligned, and -1 if angles are longitudinally aligned. Therefore, a t-test against a hypothetical mean of 0 detects significant circumferential or longitudinal alignment in each group. A similar procedure was used to detect alignment in the direction of the group mean. At each depth, unpaired t-tests were used to detect differences in alignment and collagen content between the two groups.

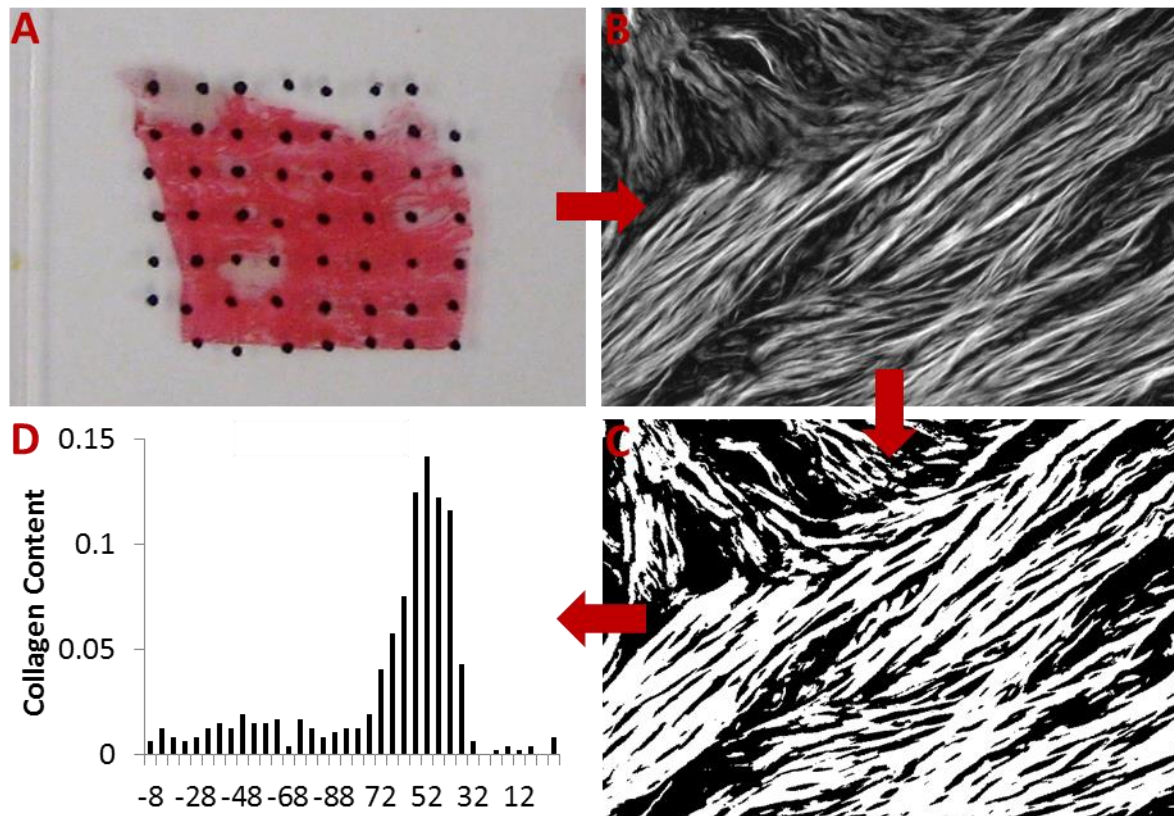


Figure 3.3 Analysis of scar structure. (A) A grid of non-overlapping imaging fields was overlaid on each section, and 10 collagenous fields were selected at random for imaging and analysis. (B) Circularly polarized and bright field (not shown) images were subtracted and (C) thresholded to isolate collagen pixels. (D) A modified Fiber3 algorithm was applied to the thresholded images to determine the distribution of collagen alignment.

Results

48 animals underwent LAD ligation surgery. Animals whose infarcts were too small to cause significant LV dilation (<20% LV) were excluded from analysis (n=3). An additional 16 animals did not survive the 8 week study period and 1 animal was excluded due to instrumentation error, leading to final group sizes of n=14 for both patch and control. By design, these group sizes were powered to detect a similar reduction in post-MI LV dilation as observed with post-MI ACE-inhibitor treatment in dogs (Jugdutt et al., 1992). An apparent trend towards higher survival in the patch group was not statistically significant (Figure 3.4). Importantly, 48 hour infarct size was similar in both groups ($33.8 \pm 5.6\%$ patch, $31.4 \pm 6.8\%$ control, P=NS), ensuring that any differences observed between groups were not due to differences in the initial infarct size (Table 3.1).

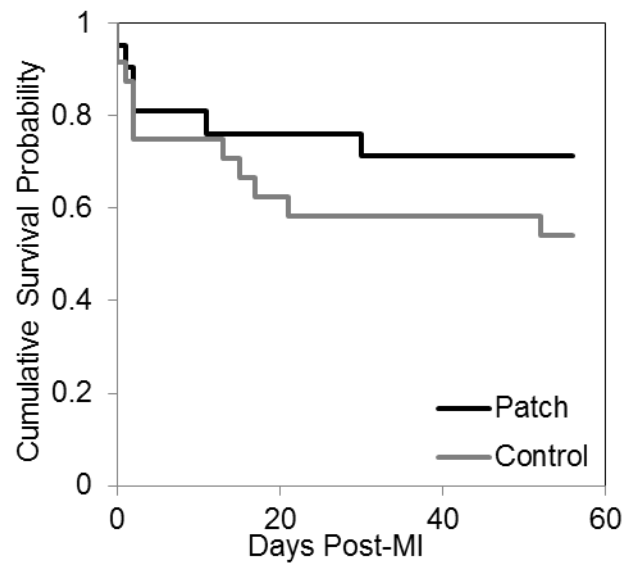


Figure 3.4 8 week survival curves in animals initially randomized to patch application or untreated control group. An apparent trend towards higher survival in the patch group was not statistically significant ($p=0.3$ by logrank test).

Table 3.1 Summary of Experimental Groups

	Patch	Control
Final Group Size	14	14
Surgery Body Mass (kg)	29.3 ± 2.1	29.8 ± 1.3
48hr Infarct Size (%LV)	33.8 ± 5.4	31.4 ± 6.8
Final Body Mass (kg)	30.7 ± 2.0	30.3 ± 2.0
Final LV Mass (g)	117.9 ± 25.5	126.0 ± 27.6
Final Heart Mass (g)	171.9 ± 17.3	183.2 ± 18.8

Experimental group size and average weight at surgery were similar between patch and control groups. Most importantly, initial infarct size did not differ between the two groups, ensuring that any differences observed between groups were not due to differences in the initial infarct size. Final body, LV, and heart mass were all similar between groups as well, suggesting there were no dramatic differences in LV remodeling ($p=NS$ for all comparisons).

Left ventricular remodeling was examined at both the organ and cell level (Figure 3.5). Average 48 hour end-diastolic volume (EDV) was $72.8 \pm 17.6 \text{ cm}^3$ in the patch group vs. $92.5 \pm 20.5 \text{ cm}^3$ in control ($P < 0.05$), and average end-systolic volume (ESV) was $55.3 \pm 14.4 \text{ cm}^3$ in the patch group, $73.3 \pm 15.2 \text{ cm}^3$ in control ($P < 0.05$). However, by 8 weeks, differences in volumes between the two groups were no longer significant, suggesting that the previously reported acute benefits of anisotropic reinforcement are either not sufficient to mitigate LV remodeling or are not sustained over the 8 week period of the study. LV muscle volume increased significantly between 48 hours and 8 weeks in both groups ($p < 0.001$). Myocardial volume was significantly greater in control animals than in patch animals at both time points ($p < 0.05$). Histological measurements of remote myocyte dimensions revealed a trend toward longer, thinner myocytes in both groups compared to normal myocytes harvested from a single non-infarcted animal. However, no differences in final myocyte dimensions were observed between patch and control animals.

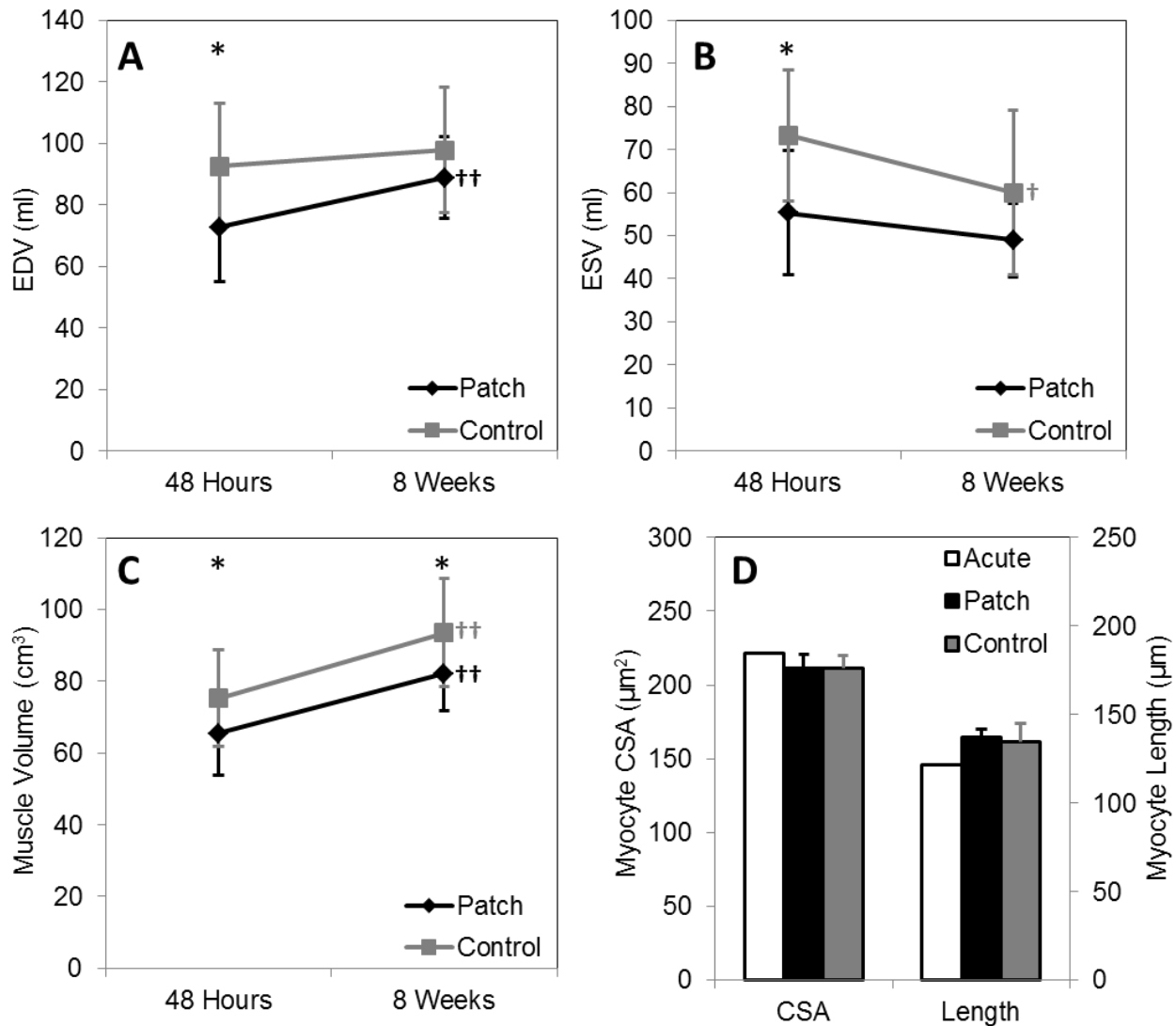


Figure 3.5 Left ventricular remodeling. (A) End-diastolic and (B) end-systolic volumes were significantly smaller in patch animals at 48 hours post-MI ($p < 0.05$ EDV, $p < 0.01$ ESV), but differences in cavity volumes faded by 8 weeks. (C) LV muscle volume (estimated from MRI as LV wall volume – infarct volume) was significantly greater in control animals at both time points ($p < 0.05$). (D) Remote myocyte measurements from both groups suggested that myocytes were longer and thinner than those from an uninfarcted control animal (white bars), consistent with the observed changes in EDV. * $p < 0.05$ patch v. control, † $p < 0.05$, †† $p < 0.001$ compared to 48 hours.

Analysis of changes in infarct size over time revealed a potential mechanism underlying the lack of sustained benefit: surprisingly dramatic scar compaction sufficient to completely reverse the effects of anisotropic reinforcement. Infarct volume decreased by more than 50% in both patch and control animals (Figure 3.6A). In both groups, the majority of compaction occurred in the circumferential direction; however, longitudinal compaction was greater than 10% on average (Figure 3.6B), sufficient to reverse the dimension changes originally induced by reinforcement (Figure 2.4). No significant differences were identified between groups, indicating that surgical reinforcement did not affect the degree or direction of scar compaction.

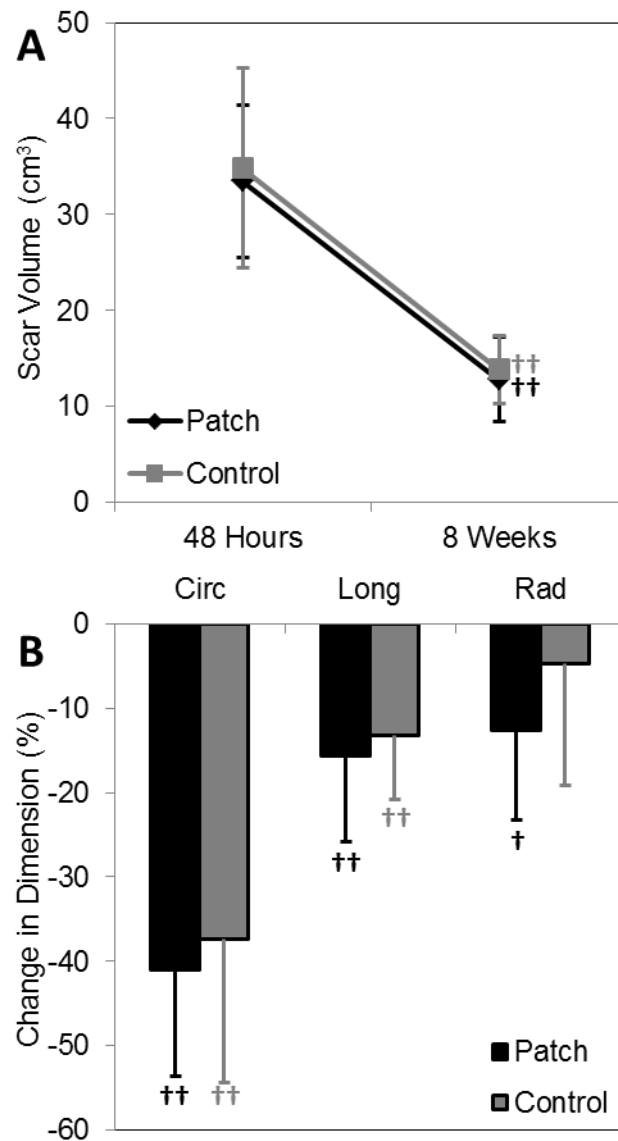


Figure 3.6 Infarct remodeling. **(A)** Infarct volume decreased significantly in both groups over the course of the study period. **(B)** Quantification of scar compaction in each dimension revealed that scars compacted by an overall average of 39% circumferentially and 14% longitudinally; significant compaction in the radial direction was observed only in the patch group. † $p < 0.01$, †† $p < 0.001$ compared to 48 hour value. $p = \text{NS}$ for all comparisons between patch and control.

Infarct scar structure at 8 weeks post-MI was examined quantitatively in terms of collagen area fraction, strength of fiber alignment, and direction of fiber alignment (Figure 3.7). Transmural alignment of collagen fibers and collagen area fraction were similar between groups ($p=NS$ for all patch v. control comparisons at each depth). Infarct wall thickness was also similar between groups, suggesting that the total amount of collagen was similar in both reinforced and unreinforced scars. In control animals, the transmural variation in mean collagen fiber angle mimics that of native myocardium, while strength of alignment was lowest at the epicardium but then fairly constant through the wall. Collagen alignment in patch animals was similar, although we observed a slight trend toward higher alignment at the midwall and lower alignment at the epi- and endocardial surfaces. Below the epicardial surface at 25% transmural depth, a slight trend toward stronger circumferential alignment in patch animals was observed, although any potential differences faded with increasing distance away from the epicardium. The total collagen content of patch and control scars was also similar, as indicated by similarities in both collagen area fraction and infarct wall thickness.

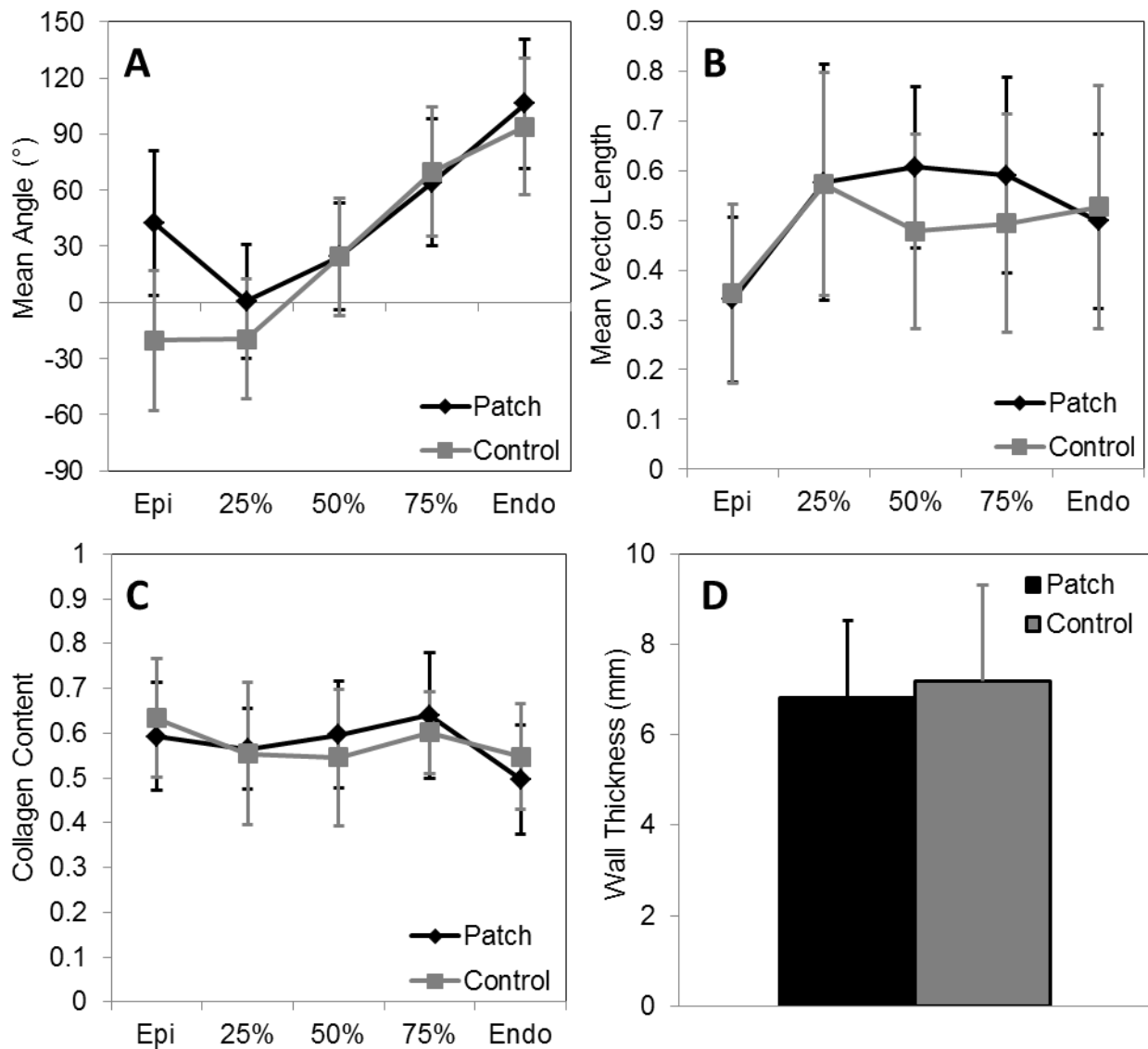


Figure 3.7 Scar Structure. (A) Mean angle and (B) mean vector length (indicating strength of alignment, where 0=randomly oriented and 1=perfectly aligned) of collagen fibers measured at 5 transmural depths. In control animals, the mean orientation of collagen fibers mimics the transmural distribution of muscle fiber angles, and strength of alignment is highest at the midwall. Patch animals exhibited a trend towards stronger circumferential fiber alignment at 25% depth, with apparent differences fading with increasing distance away from the epicardium. $p=NS$ between patch and control for mean angle and mean vector length at every transmural depth. (C) Collagen area fraction at each depth and (D) infarct wall thickness were also similar between groups, leading to no differences in total scar collagen volume fraction.

Hemodynamic data were measured at the terminal 8 week study and used to compare LV function (Figure 3.8). Baseline function in both groups was compared to data from a group of open chest, uninfarcted control animals studied previously (Fomovsky, Clark, et al., 2012), and Db was used to measure the ability of the myocytes to respond to β -adrenergic stimulation. At baseline, SV and CO (interpolated at a matched EDP of 12mmHg) were similar across groups. In uninfarcted animals, heart rate, Ees, and max dPdt all significantly increased in response to Db treatment. In both infarct groups, Db stimulation produced a significant increase in max dPdt but had no effect on Ees, and an increase in heart rate was observed in control but not patch animals. Control animals also exhibited an increase in CO following β -adrenergic stimulation, although no other groups showed changes in either CO or SV with Db administration.

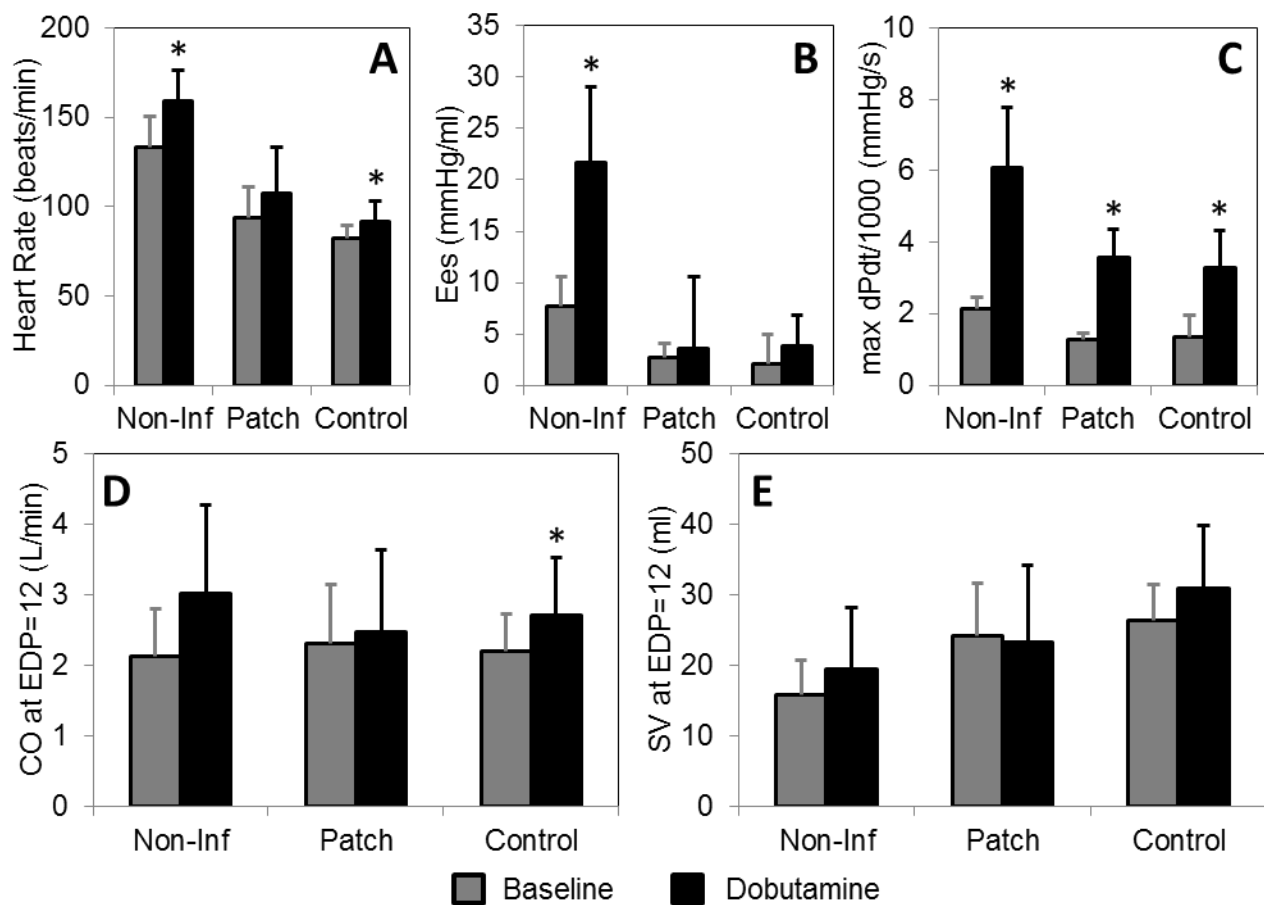


Figure 3.8 Hemodynamics at 8-week terminal study compared to previously unpublished data a group of 9 non-infarcted animals. **(A)** Heart rate, **(B)** end-systolic elastance, and **(C)** maximum rate of LV pressure generation at baseline (gray bars) were all significantly decreased in both patch and control groups compared to non-infarcted. A significant response to Db (black bars) was measured in all three indices in non-infarcted animals, but was only observed in the max dPdt of infarcted animals and in the heart rate of control animals. **(D)** Cardiac output (interpolated at a matched EDP of 12mmHg) was maintained across experimental groups, and only control animals exhibited an increase in CO with Db treatment. **(E)** Stroke volume (interpolated at a matched EDP of 12mmHg) was also similar among groups and did not change with Db treatment. * $p < 0.01$, paired comparison to pre-Db value.

Discussion

We conducted a chronic, large-animal trial of anisotropic reinforcement, a strategy previously shown to dramatically improve acute LV function following a large anteroapical infarct (Fomovsky, Clark, et al., 2012). At 48 hours, patch animals had lower EDV and ESV on MRI, confirming that anisotropic reinforcement altered LV mechanics acutely. However, by 8 weeks there were no significant differences in patch animal survival, LV function, or LV remodeling compared to untreated controls. Our scar remodeling data suggest that compaction of the infarct scar in the epicardial plane over the 8-week study may have reversed the effect of the treatment by relieving the initial tension in the patch. Upon harvest, patches were found to be strongly adhered to the epicardium with visible wrinkling in the longitudinal direction, further corroborating our hypothesis that the patches were mechanically unloaded by the end of the study. These results were surprising, because the infarct healing literature typically focuses on infarct expansion – circumferential and longitudinal dilation plus radial thinning – rather than scar compaction. However, a recent review of studies that actually reported infarct dimensions suggests that expansion and compaction occur with similar frequency (Richardson & Holmes, 2013). Accordingly, different therapeutic approaches may have very different efficacy in different animal models or even in different patients. We would expect surgical restraint – as in our study – to be most effective for infarcts that would normally expand if untreated. This might explain why studies that applied isotropic patches locally to prevent infarct expansion have produced more variable effects on LV remodeling than those that employed global restraint with cardiac support devices (Clarke, Ghanta, Ailawadi, & Holmes, 2014).

Considering what is known about the process of infarct scar formation, we were also surprised to find that mechanical reinforcement did not alter the collagen structure of

the resulting scar. In the weeks following an MI, fibroblasts infiltrate the damaged region and begin to deposit and remodel collagen to eventually form a stiff, noncontractile scar (Eghbali et al., 1989). The recruitment and activity of these cells are governed by an array of biochemical and biophysical cues, including mechanical stretch (Lee, Holmes, and Costa 2008; Thomopoulos, Fomovsky, and Holmes 2005). *In vitro*, fibroblasts can respond to uniaxial stretch by depositing new collagen fibers parallel to the strain cue, or by rotating existing fibers toward alignment with the stretch direction (Canty et al., 2004; Petroll, Ma, & Jester, 2003). *In vivo*, our group has shown that the strain pattern in an infarct is a crucial determinant of the scar structure that forms, and can explain differences in scar collagen arrangement across different infarct locations and animal models (Fomovsky, Rouillard, & Holmes, 2012; Rouillard & Holmes, 2012). Specifically, in infarcts subject to uniaxial in-plane stretching we have observed collagen alignment in the direction of greatest stretch, while infarcts that undergo equibiaxial stretching form scars with randomly oriented collagen fibers (Fomovsky & Holmes, 2010; Fomovsky, Rouillard, et al., 2012). Therefore, we would expect reinforcement therapies that dramatically alter deformation and stretching in an acute infarct to change the collagen structure of the resulting scar. This surprising result may offer some clues to the timing of the mechanical unloading of the patch by compaction: since most of the collagen deposition occurs in weeks 1-4 following infarction in the dog (Jugdutt & Amy, 1986), substantial unloading may have already occurred by this point in healing. Consistent with this timeline, Theroux et al. reported a 10% reduction in ED circumferential segment lengths measured by sonomicrometry at 2 weeks and a 21% reduction at 3 weeks in healing infarcts in dogs (Theroux, Ross, Franklin, Kemper, & Sasyama, 1976). An alternate potential explanation is that the mechanical effects of the patch are confined to the outer part of the infarct (where we saw some qualitative but non-significant differences in structure); however, this explanation seems less likely

given that we previously measured large acute changes in mechanics at the midwall in response to patch application (Figure 2.4).

In the current study, we hypothesized that selective longitudinal infarct restraint would force the direction of greatest infarct stretching to be circumferential, leading to a scar composed of fibers more strongly aligned in the circumferential direction. Although we did not find any significant differences between patched and unpatched scar structure, we did observe a slight trend toward greater circumferential alignment at 25% transmural depth, in agreement with our original hypothesis. The effects of epicardial restraint on scar structure seem to diminish with increasing distance away from the epicardium, as evidenced by the remarkable similarity in both strength and direction of fiber alignment near the endocardium. We also observed a trend toward more randomly oriented collagen at the epicardial surface in patch animals, but we suspect that these fibers reflect a fibrotic foreign body response to patch implantation and that their deposition may not be governed by the same cues direction formation of the infarct scar. However, our data suggest that by 8 weeks post-MI, compaction is the dominant scar remodeling process and may mask more subtle differences in scar structure that were present during the early stages of scar formation. Serial measurements of scar dimensions throughout the course of infarct healing, similar to the time course of changes in an infarct segment length measured over 4 weeks post-MI by Theroux (Theroux et al., 1977), would be needed in order to get a complete picture of the time course of scar remodeling in each direction.

Given previous reports of attenuation of LV dilation with both global and local infarct restraint approaches, we were also surprised to find no differences in final LV cavity volumes between our patch and control groups. Patch animals did have significantly smaller LV volumes at 48 hours post-MI, but differences in cavity volumes between

groups had faded by 8 weeks. In accordance with the cavity volumes, final LV mass, heart mass, and remote myocyte dimension measurements all indicated similar degrees of myocardial remodeling. Surprisingly, myocardial volume calculated from MRI indicated significantly greater muscle volume in control animals at both 48 hour and 8 week time points. However, since 48 hours is too soon to observe differences in myocardial volume due to LV hypertrophy, we suspect that the apparent difference in wall volume arises from an inability to detect differences in acute radial thinning in the border zone due to the transmural resolution of the MR images. It is possible that the apparent difference in 8 week muscle volumes stems from a similar phenomenon, since differences in final myocardial volume on MRI conflicted with direct measurements of final LV mass and remote myocyte size. Although we used myocyte size data from a single, uninfarcted animal as a basis for comparison to our patch and control groups, our un-infarcted cell length and CSA values matched well with previously reported values in dogs. Using fixed, paraffin-embedded sections, Gerdes & Kasten and Komamura et al. measured average myocyte CSAs of $279\mu\text{m}^2$ (heart mass = 141g) and $179\mu\text{m}^2$ (heart mass = 198g), respectively, and Volders et al. measured an average length of $140\mu\text{m}$ (heart mass = 222g) in isolated myocytes (Gerdes & Kasten, 1980; Komamura et al., 1993; Volders et al., 1998). However, substantial variability in reported myocyte dimensions between studies using different preparation and measurement techniques led us to compare our patch and control values to data that were generated using the exact same experimental and analysis procedures.

The results of the current study highlight the importance of developing computational models that can accurately predict not only the acute effect of a therapy on LV mechanics, but also its long-term effects on scar and LV remodeling. Although local infarct restraint therapies are susceptible to mechanical unloading through scar compaction, global restraint devices (restraining one or both ventricles) are also

sensitive to changes in ventricular geometry. In a study of post-MI, global LV restraint in sheep, Ghanta and colleagues observed that the restraint level (selected to be optimum at the time of implantation) decreased over time as the LV reverse remodeled, to the point where there was no longer any restraint pressure being applied to the LV at the final time point (Ghanta et al., 2007). In a follow-up study exploring the effects of adjustable restraint during healing, the same group explored a dynamic approach in which restraint pressure was maintained constant during healing and found enhanced reductions in LV volumes compared to static restraint (Lee et al. 2012). Another group used a local device to examine the effects of optimized, static infarct restraint on LV remodeling and found that local reinforcement led to smaller LV volumes but no improvement in SV (Koomalsingh et al., 2013). In order to predict the chronic effects of acute infarct reinforcement, computational models that better represent the dynamic interplay between scar remodeling, ventricular remodeling, and degree of restraint are needed. Such models will not only be useful for predicting the chronic effects of acute therapies or the optimal timing of reinforcement, but could also be used to explore and optimize dynamic approaches.

It is worth noting that all measurements of scar compaction in this study were made from MR images acquired at end diastole in a pressurized LV. Changes in scar dimensions measured in a loaded configuration could simultaneously reflect changes in cavity pressure, scar mechanical properties, and/or scar dimensions. Due to stiffening of the scar during healing, our scar compaction data likely overestimate the amount of in-plane (circumferential and longitudinal) compaction and underestimate radial compaction compared to the ideal case of making serial measurements of scar dimensions in an unloaded LV. As an example, imagine two identical, unloaded ventricles with the same size scar, but one scar is much stiffer than the other. When both ventricles are inflated to the same cavity pressure, the stiffer scar will not deform

or stretch as much as the soft scar, making it appear smaller (circumferentially and longitudinally) and thicker (radially) than the soft scar. Although the volume of both scars is still the same, small differences in the radial dimension can be hard to quantify from MRI due to limitations in the number of pixels spanning the LV wall. Therefore, as infarcts stiffen during healing, serial measurements of scar dimensions in a loaded ventricle may lead to overestimation of in-plane compaction and underestimation of radial thinning. In addition, changes measured from MRI are often, as in this study, unaccompanied by simultaneous measurement of LV pressure, so differences in loading during measurement of scar dimensions are also unknown.

Conclusion

In summary, the present study explored the use of longitudinal infarct restraint as a chronic, post-MI therapy. None of the acute functional benefits of patch application observed in a previous study were sustained over 8 weeks, nor were any differences identified in LV remodeling or scar structure. Examination of the infarct dimensions during healing suggested that our restraint device had become mechanically unloaded by dramatic in-plane scar compaction. The results of the present study highlight the need for computational models that can predict infarct and ventricular remodeling and suggest that local, dynamic restraint therapies may offer enhanced benefit over static devices.

References

- Bristow, M. R., Ginsburg, R., Minobe, W., Cubicciotti, R. S., Sageman, S., Lurie, K., ... Stinson, E. B. (1982). Decreased catecholamine sensitivity and B-adrenergic-receptor density in failing human hearts. *The New England Journal of Medicine*, 307(4), 205–211.
- Canty, E. G., Lu, Y., Meadows, R. S., Shaw, M. K., Holmes, D. F., & Kadler, K. E. (2004). Coalignment of plasma membrane channels and protrusions (fibroprotrusions) specifies the parallelism of tendon. *Journal of Cell Biology*, 165(4), 553–563.
- Clarke, S. A., Ghanta, R. K., Ailawadi, G., & Holmes, J. W. (2014). Cardiac Restraint & Support Following Myocardial Infarction. In T. Franz (Ed.), *Cardiovascular and Cardiac Therapeutic Devices* (pp. 169–206). Springer Berlin Heidelberg.
- Dolber, P. C., Beyer, E. C., Junker, J. L., & Spach, M. S. (1992). Distribution of gap junctions in dog and rat ventricle studied with a double-label technique. *Journal of Molecular and Cellular Cardiology*, 24, 1443–1457.
- Dolber, P. C., & Spach, M. S. (1987). Picrosirius red staining of cardiac muscle following phosphomolybdic acid treatment. *Stain Technology*, 62(1), 23–26.
- Eghbali, M., Blumenfeld, O. O., Seifert, S., Buttrick, P. M., Leinwand, L. A., Robinson, T. F., ... Giambrone, M. A. (1989). Localization of types I, III and IV collagen mRNAs in rat heart cells by in situ hybridization. *The Journal of Molecular and Cellular Cardiology*, 21, 103–113.
- Fomovsky, G. M., Clark, S. A., Parker, K. M., Ailawadi, G., & Holmes, J. W. (2012). Anisotropic reinforcement of acute anteroapical infarcts improves pump function. *Circulation Heart Failure*, 5, 515–522.
- Fomovsky, G. M., & Holmes, J. W. (2010). Evolution of scar structure, mechanics, and ventricular function after myocardial infarction in the rat. *American Journal of Physiology, Heart and Circulatory Physiology*, 298(1), H221–8.
- Fomovsky, G. M., Rouillard, A. D., & Holmes, J. W. (2012). Regional mechanics determine collagen fiber structure in healing myocardial infarcts. *Journal of Molecular and Cellular Cardiology*, 52(5), 1083–90.

- Fowler, M. B., Laser, J. A., Hopkins, G. L., Minobe, W., & Bristow, M. R. (1986). Assessment of the beta-adrenergic receptor pathway in the intact failing human heart: progressive receptor down-regulation and subsensitivity to agonist response. *Circulation*, 74(6), 1290–1302.
- Gerdes, a M., & Kasten, F. H. (1980). Morphometric study of endomyocardium and epimyocardium of the left ventricle in adult dogs. *The American Journal of Anatomy*, 159(4), 389–94.
- Ghanta, R. K., Rangaraj, A., Umakanthan, R., Lee, L., Laurence, R. G., Fox, J. A., ... Chen, F. Y. (2007). Adjustable, physiological ventricular restraint improves left ventricular mechanics and reduces dilatation in an ovine model of chronic heart failure. *Circulation*, 115(10), 1201–10.
- Ginsburg, R., Bristow, M. R., Billingham, M. E., Stinson, E. B., Schroeder, J. S., & Harrison, D. C. (1983). Study of the normal and failing isolated human heart: decreased response of failing heart to isoproterenol. *American Heart Journal*, 106(3), 535–40.
- Go, A. S., Mozaffarian, D., Roger, V. L., Benjamin, E. J., Berry, J. D., Blaha, M. J., ... Turner, M. B. (2013). Heart Disease and Stroke Statistics--2014 Update: A Report From the American Heart Association. *Circulation*, 129, e28–e292.
- Heiberg, E., Sjogren, J., Ugander, M., Carlsson, M., Engblom, H., & Arheden, H. (2010). Design and validation of Segment - a freely available software for cardiovascular image analysis. *BMC Medical Imaging*, 10(1).
- Jugdutt, B. I. (2002). The dog model of left ventricular remodeling after myocardial infarction. *Journal of Cardiac Failure*, 8(6 Suppl), S472–5.
- Jugdutt, B. I., & Amy, R. W. M. (1986). Healing after myocardial infarction in the dog: changes in infarct hydroxyproline and topography. *Journal of the American College of Cardiology*, 7(1), 91–102.
- Jugdutt, B. I., Schwarz-Michorowski, B. L., & Khan, M. I. (1992). Effect of long-term captopril therapy on left ventricular remodeling and function during healing of canine myocardial infarction. *Journal of the American College of Cardiology*, 19(3), 713–721.

- Junqueira, L. C., Bignolas, G., & Brentani, R. R. (1979). Picrosirius staining plus polarization microscopy, a specific method for collagen detection in tissue sections. *Histochemical Journal*, 11(4), 447–455.
- Karlon, W. J., Covell, J. W., McCulloch, A. D., Hunter, J. J., & Omens, J. H. (1998). Automated measurement of myofiber disarray in transgenic mice with ventricular expression of ras. *The Anatomical Record*, 252(4), 612–25.
- Kim, R. J., Fieno, D. S., Parrish, T. B., Harris, K., Chen, E., Simonetti, O., ... Judd, R. M. (1999). Relationship of MRI delayed contrast enhancement to irreversible injury, infarct age, and contractile function. *Circulation*, 100, 1992–2002.
- Komamura, K., Shannon, R. P., Ihara, T., Shen, Y. T., Mirsky, I., Bishop, S. P., & Vatner, S. F. (1993). Exhaustion of Frank-Starling mechanism in conscious dogs with heart failure. *The American Journal of Physiology*, 265(4 Pt 2), H1119–31.
- Koomalsingh, K. J., Witschey, W. R. T., McGarvey, J. R., Shuto, T., Kondo, N., Xu, C., ... Pilla, J. J. (2013). Optimized local infarct restraint improves left ventricular function and limits remodeling. *The Annals of Thoracic Surgery*, 95(1), 155–62.
- Lee, E. J., Holmes, J. W., & Costa, K. D. (2008). Remodeling of engineered tissue anisotropy in response to altered loading conditions. *Annals of Biomedical Engineering*, 36(8), 1322–1334.
- Lee, L. S., Ghanta, R. K., Mokashi, S. A., Coelho-Filho, O., Kwong, R. Y., Kwon, M., ... Chen, F. Y. (2012). Optimized ventricular restraint therapy: adjustable restraint is superior to standard restraint in an ovine model of ischemic cardiomyopathy. *The Journal of Thoracic and Cardiovascular Surgery*, 145(3), 824–31.
- Luna, L. G. (1992). *Histopathologic Methods and Color Atlas of Special Stains and Tissue Artifacts*. Gaithersburg, MD: American Histolabs.
- Petroll, W. M., Ma, L., & Jester, J. V. (2003). Direct correlation of collagen matrix deformation with focal adhesion dynamics in living corneal fibroblasts. *Journal of Cell Science*, 116(Pt 8), 1481–1491.
- Richardson, W. J., & Holmes, J. W. (2013). Do infarcts really expand or compact? Relationship between changing material properties and apparent infarct remodeling. Presented at the ASME 2013 Summer Bioengineering Conference, June 26-29, 2013, Sunriver, Oregon.

- Roger, V. L., Go, A. S., Lloyd-Jones, D. M., Benjamin, E. J., Berry, J. D., Borden, W. B., ... Turner, M. B. (2011). Heart disease and stroke statistics--2012 update: a report from the American Heart Association. *Circulation*, *125*, e2–e220.
- Rouillard, A. D., & Holmes, J. W. (2012). Mechanical regulation of fibroblast migration and collagen remodeling in healing myocardial infarcts. *The Journal of Physiology*, *18*, 4585–4602.
- Shapiro, E. P., Rogers, W. J., Beyar, R., Soulen, R. L., Zerhouni, E. A., Lima, J. A., & Weiss, J. L. (1989). Determination of left ventricular mass by magnetic resonance imaging in hearts deformed by acute infarction. *Circulation*, *79*(3), 706–711.
- Theroux, P., Ross, J., Franklin, D., Covell, J. W., Bloor, C. M., & Sasayama, S. (1977). Regional myocardial function and dimensions early and late after myocardial infarction in the unanesthetized dog. *Circulation Research*, *40*(2), 158–65.
- Theroux, P., Ross, J., Franklin, D., Kemper, W. S., & Sasayama, S. (1976). Regional myocardial function in the conscious dog during acute coronary occlusion and responses to morphine, propranolol, nitroglycerin, and lidocaine. *Circulation*, *53*(2), 302–314.
- Thomas, J. A., & Marks, B. H. (1978). Plasma norepinephrine in congestive heart failure. *The American Journal of Cardiology*, *41*(2), 233–43.
- Thomopoulos, S., Fomovsky, G. M., & Holmes, J. W. (2005). The development of structural and mechanical anisotropy in fibroblast populated collagen gels. *Journal of Biomechanical Engineering*, *127*(5), 742.
- Veeraraghavan, R., Gourdie, R. G., & Poelzing, S. (2014). Mechanisms of cardiac conduction: a history of revisions. *American Journal of Physiology. Heart and Circulatory Physiology*, *306*(5), H619–27.
- Volders, P. G., Sipido, K. R., Vos, M. A., Kulcsár, A., Verduyn, S. C., & Wellens, H. J. (1998). Cellular basis of biventricular hypertrophy and arrhythmogenesis in dogs with chronic complete atrioventricular block and acquired torsade de pointes. *Circulation*, *98*(11), 1136–1147.
- Whittaker, P., Kloner, R. A., Boughner, D. R., & Pickering, J. G. (1994). Quantitative assessment of myocardial collagen with picosirius red staining and circularly polarized light. *Basic Research in Cardiology*, *89*(5), 397–410.

Chapter 4

Effects of Sample Heterogeneity on Biaxially Measured Material Properties

Upon harvest, both reinforced and unreinforced infarct scars exhibited significant heterogeneity in scar morphology. Some animals formed scars with one or several large patches of dense collagen, while others formed scars that more closely resembled diffuse fibrosis, with few or no large areas of coherent scar. In an effort to quantify differences in scar mechanical properties as a complement to the analysis of scar structure, biaxial mechanical testing was performed on a subset of seven (4 patch, 3 control) animals. However, the variability between animals and heterogeneity of collagen deposition within each infarct made both the specimen preparation and interpretation of test results a challenge. Therefore, a finite element model was built to simulate the effects of scar heterogeneity on the measured biaxial mechanical properties of an infarct.

Theory of plane stress analysis in biaxial testing

Biaxial testing of soft tissues is a robust way to characterize the material properties of both synthetic and biologic materials. Unlike uniaxial methods, biaxial analysis allows characterization of anisotropic materials, in which deformation along a single axis in the material can depend on loading in the other dimensions. A state of plane stress is a common assumption made in biaxial mechanical characterization of soft tissues. Plane stress describes a state in which stresses perpendicular to the plane of analysis are negligible relative to the stresses in the plane. In planar biaxial testing, stress and strain are analyzed in the plane of applied load (x - and y -dimensions), strains in the z -dimension can be estimated assuming incompressibility, and stress in the z -dimension is assumed to be 0. In this simplified formulation, the deformation gradient tensor (\mathbf{F}) reduces to:

$$\mathbf{F} = \begin{bmatrix} \lambda_1 & \kappa_1 & 0 \\ \kappa_2 & \lambda_2 & 0 \\ 0 & 0 & \lambda_3 \end{bmatrix}$$

Where each λ is the axial stretch in the corresponding dimension, and κ are shears. The components of the deformation gradient tensor \mathbf{F} can be calculated from the x - y positions of discrete surface markers, as:

$$x = \mathbf{F} \cdot X$$

$$\begin{bmatrix} x_1 & x_2 & \dots & x_n \\ y_1 & y_2 & \dots & y_n \end{bmatrix} = \begin{bmatrix} F_{11} & F_{12} & p_1 \\ F_{21} & F_{22} & p_2 \end{bmatrix} \begin{bmatrix} X_1 & X_2 & \dots & X_n \\ Y_1 & Y_2 & \dots & Y_n \\ 1 & 1 & \dots & 1 \end{bmatrix}$$

where x_i and y_i are the deformed and X_i and Y_i the undeformed coordinates of marker i , and p_i are the components of the translation vector. Assuming incompressibility, stretch in the z -dimension can be determined from the deformation in the x - y plane:

$$F_{33} = \lambda_3 = \frac{1}{\lambda_1 \lambda_2 - \kappa_1 \kappa_2}$$

The right Cauchy-Green deformation tensor (\mathbf{C}) and Lagrangian strain tensor (\mathbf{E}) can then be directly computed from \mathbf{F} :

$$\mathbf{C} = \mathbf{F}^T \mathbf{F}$$

$$\mathbf{E} = \frac{1}{2}(\mathbf{C} - \mathbf{I})$$

where \mathbf{I} is the identity tensor. The 1st Piola-Kirchoff Stress tensor is the most readily calculated from experimental biaxial data, because it expresses stress in the material as the current force divided by the original, undeformed cross-sectional area of the sample.

Sample preparation and biaxial test setup

To ensure the validity of the plane stress assumption and the analysis described above, an in-plane dimension:thickness ratio of 10:1 or greater is typically employed. However, because the LV is a thick-walled structure, our infarct scars were too thick upon harvest to satisfy this condition. Therefore, each scar was cut in half transmurally, into an epicardial and endocardial sample, prior to testing. It was at the midwall in these sliced samples where we were first able to observe striking differences in gross

scar structure that had gone undetected in the MR studies and in our other scar analyses. In the subgroup of 7 scars that were subjected to biaxial testing, some contained large patches of dense scar, while others exhibited a more diffuse fibrotic pattern with small patches of dense scar. Patch animals tended to have larger areas of dense collagen, although this observation was partially confounded by a consistent, visible fibrotic response to the sutures running around the edges of the patch (Figure 4.1). After transmural slicing, the thickness of each sample was measured for subsequent stress calculations. Since some samples exhibited regional variation in thickness, five thickness measurements were made across the surface of each sample and the average value was used in subsequent area and stress calculations.

We performed biaxial mechanical testing on each sample using a custom device developed by Dr. Michael Sacks (Grashow, Yoganathan, & Sacks, 2006). The device is controlled through a LabView Virtual Instrument, and consists of four arms controlled by four motors, allowing independent stretch and translation along the two in-plane axes. Loads along each axis are measured by two load cells attached to perpendicular arms, and deformation in the tissue is quantified optically by digital tracking a grid of nine markers attached to the sample surface. In this study, small glass beads were used as markers and were attached to the surface of the tissue with Crazy Glue. To mount the sample in the device, four hooks were placed along each edge of the sample, and adjacent pairs of hooks were connected by a suture loop, which were then placed around a roller on the device arm. While in the device, the sample was submerged in a circulating bath of cold, oxygenated arrest solution to prevent muscle contracture during testing. Figure 4.2A shows a sample prepared for testing, and Figure 4.2B shows a sample mounted in the device. Load-controlled tests were run by specifying applied forces along each axis and measuring the resulting deformation.

In an ideal sample, we would have been able to place all 16 hooks and the entire marker grid in an area of coherent scar. This would ensure that the entirety of each applied load was being transferred to the scar, and that the subsequent deformation represented the mechanical response of the scar alone to those applied loads. Unfortunately, due to the heterogeneity in each scar distribution, we were not able to achieve this configuration in any sample. Although in some cases we could have excised a large area of dense scar to test in isolation, the degree of heterogeneity we observed in our measurements of local collagen alignment suggested that measurements taken from a small subregion of the scar might not be reflective of the properties of the scar region as a whole. In addition, trimming in the epicardial (circumferential-longitudinal) plane would have produced samples with dimensions that violated the 10:1 ratio required for plane stress analysis, necessitating that samples undergo further transmural slicing into thinner sheets. Therefore, we chose to keep our samples intact and test the entire scar area in control animals, and the entire scar area reinforced by the patch in patch animals. However, the effects of sample heterogeneity on the measured displacements and resulting stress-strain estimations were unknown. Therefore, a collection of finite element models was constructed to examine potential differences in biaxial behavior among samples containing different amounts or distributions of scar.

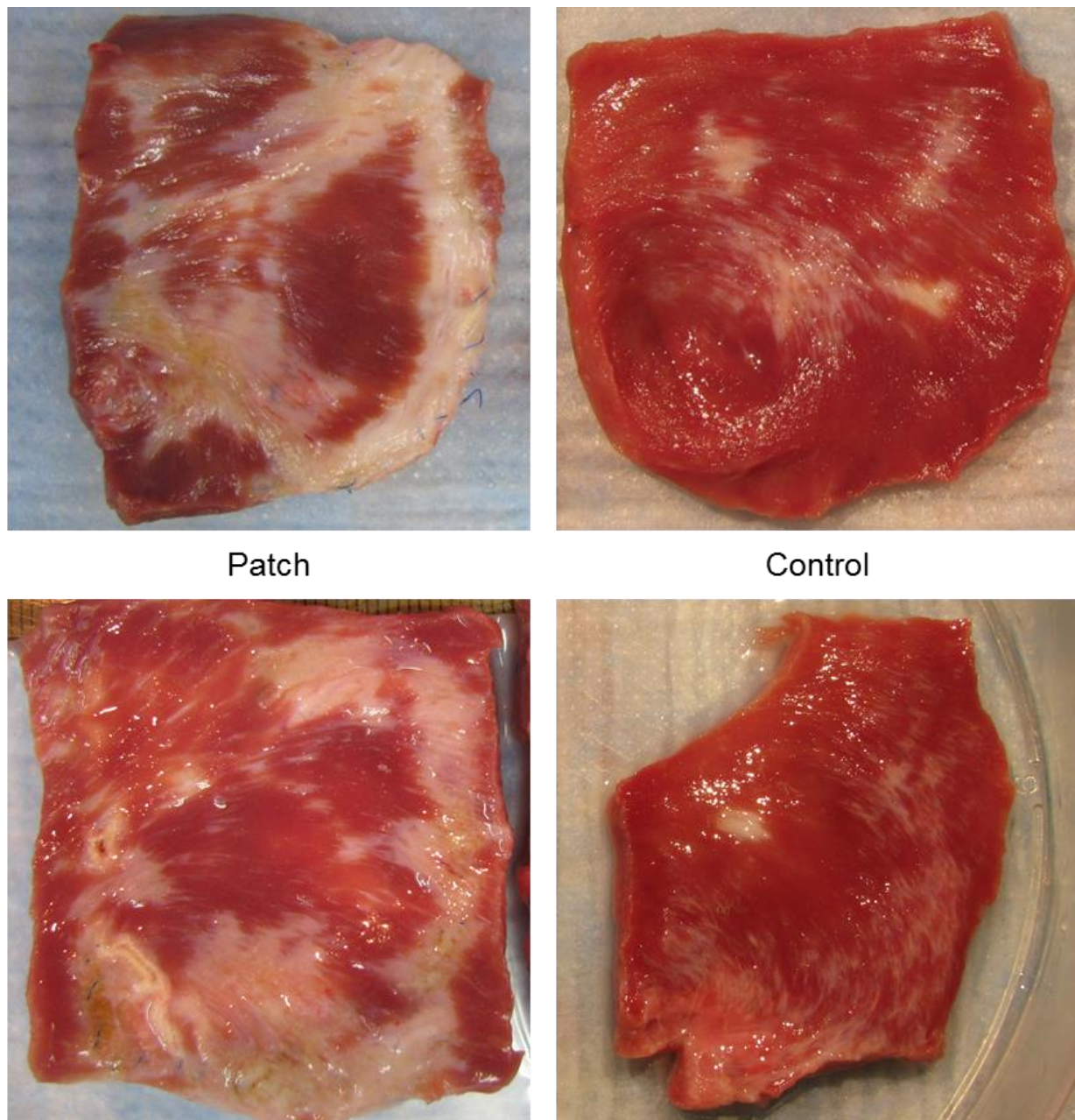


Figure 4.1 Two patch (left) and two control (right) infarct scar biaxial test specimens, sliced in half transversally and displayed at the midwall.

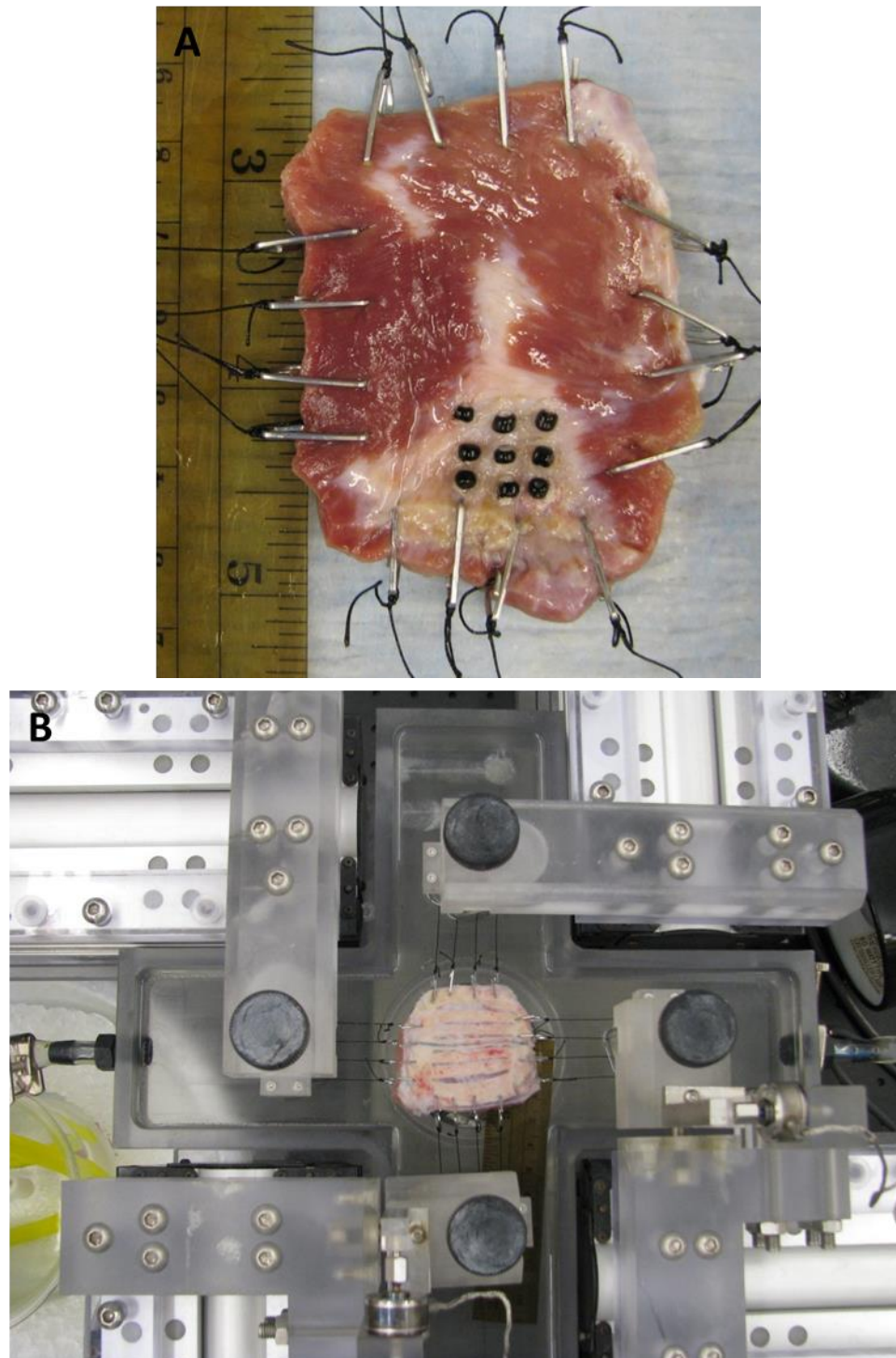


Figure 4.2 (A) Infarct specimen prepared for biaxial testing and (B) specimen mounted in biaxial testing device.

Model geometry & material properties

We used a simplified, rectangular geometry to evaluate the effects of various scar distributions on biaxial stress-strain behavior. A 5cm x 5cm x 0.5cm mesh was constructed to represent an excised scar sliced in half transmurally, and was divided into 2000 (20x20x5) hexahedral elements. To examine the effect of scar distribution, different scar configurations were simulated by varying the distribution of individual scar and muscle elements. Both muscle and scar were assumed to be isotropic and were modeled using a nearly incompressible Veronda-Westmann constitutive model (Veronda & Westmann, 1970):

$$W = C_1(e^{(C_2(I_1-3))} - 1) - \frac{C_1 C_2}{2}(I_2 - 3) + U(J)$$

where C_1 and C_2 are material coefficients, I_1 and I_2 are invariants of the deviatoric part of the right Cauchy-Green deformation tensor, and $U(J)$ is the dilatational component. Material coefficients for passive myocardium ($C_1=5$, $C_2=20$) were determined by fitting the passive canine myocardium biaxial test data of Demer and Yin (Demer & Yin, 1983), and stiff scar was approximated by scaling the C_2 coefficient by a factor of 50. A density of 1.06 g/cm³ and a bulk modulus of 25000 were used for both muscle and scar.

Loading & boundary conditions

In the finite element software FEBio (Maas, Ellis, Ateshian, & Weiss, 2012), biaxial tension was applied by assigning point forces to columns of nodes along each edge. Four locations of applied load were defined on each edge to mimic the positions of the four hooks used on each edge in our biaxial experiments (Figure 4.3, open circles). However, each load was assumed to be evenly distributed transmurally through the

sample, so each location of applied load in the x-y view actually represents a column of six nodes stacked on top of each other, each with the same assigned applied force acting normally to the corresponding edge of the sample. Simulations were run using an assigned load of 25g to each node, leading to an applied equibiaxial load of 600g ($25\text{g}/\text{node} \times 24 \text{ nodes}/\text{side} = 600\text{g}$).

The mesh was fixed in space with zero displacement boundary conditions in the x, y and z directions. In symmetrical models, translation in the x-y plane was prevented by constraining transmural columns of nodes in the center of each edge (Figure 4.3). Nodes in the location marked with a red "X" were fixed in the y-direction, and those marked with a blue "X" were fixed in the x-direction. Translation in the z-direction was constrained by fixing nodes at the corners, marked with a green "X", although unlike the other directions, this constraint was applied only to a single layer of nodes (instead of transmurally) to allow element thinning during loading. In a subset of models, the distribution of scar elements created a non-symmetrical geometry, and therefore required a slight change in boundary conditions to prevent artificial restriction of motion. In these models, the constraints in the x-y plane were moved to pairs of corners, to effectively simulate two fixed and two loaded edges.

We simulated our biaxial test marker displacement data by exporting the positions of a central grid of nine nodes on the surface of the model geometry (Figure 4.3, black circles). To mirror our analysis approach for biaxial test data, we calculated Lagrangian strain from the nodal displacements and 1st Piola-Kirchoff stress using the current applied load and the undeformed cross-sectional area of the sample. Since only a subset of the marker grid was placed in scar in some of our biaxial test samples, we calculated strains using a subset of four nodes located in scar elements (markers 1,2,4,5). A convergence study was performed to examine the relationship between surface

displacements and element density. Five “All Scar” models of increasing mesh density (decreasing element size) were constructed: 8, 144, 400, 1024, and 1600 elements. All models were loaded to 600g of equibiaxial tension, and the average x-displacements of a row of elements were plotted relative to the normalized x-positions of each element in the unloaded mesh.

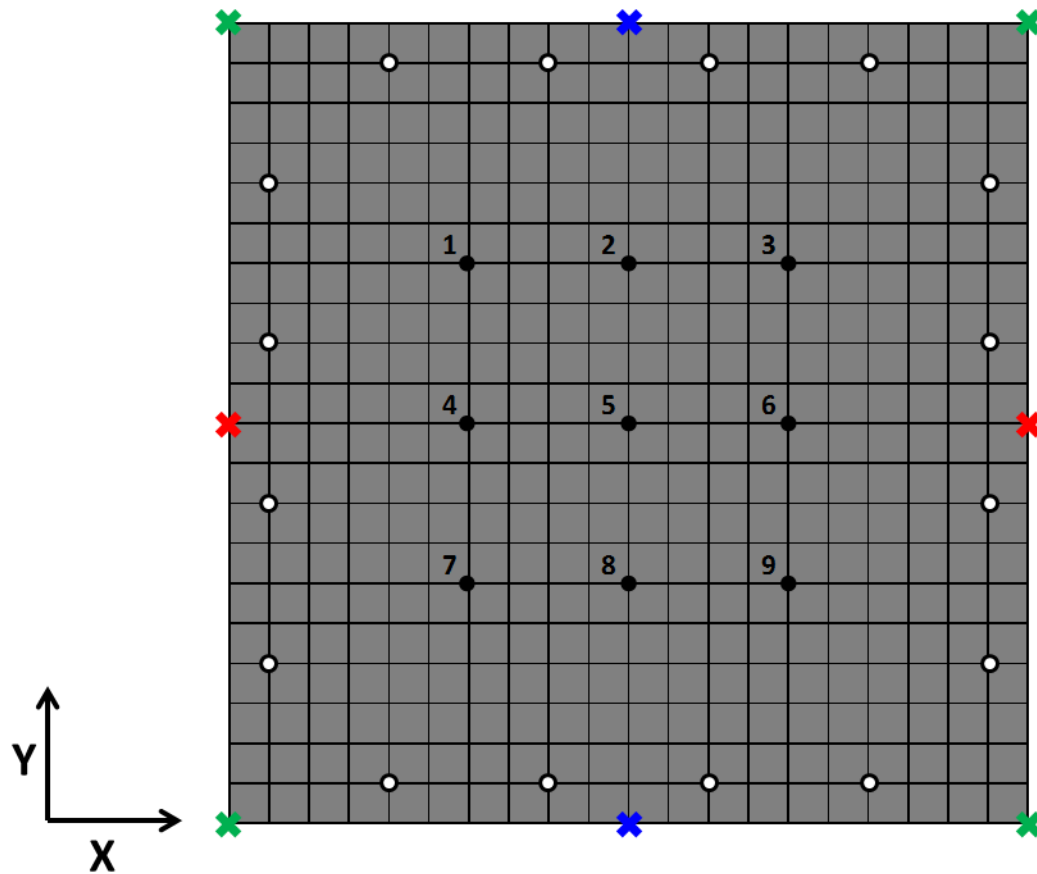


Figure 4.3 Diagram of model definition. Locations of applied nodal loads (normal to the corresponding edge) are shown with open white circles. Nodes in the locations marked with a red "X" were fixed in Y, nodes marked with a blue "X" were fixed in X, and a single layer of nodes at the locations marked with a green "X" were fixed in Z. Displacements of surface markers were simulated by tracking the positions of the nodes marked with closed black circles.

Mesh refinement study

A model composed entirely of scar elements was built to serve as a reference for comparison with all subsequent test models of variable scar distribution and size. Convergence analysis was performed on this “All Scar” model by comparing average element displacements between five meshes of increasing element number: 8, 144, 400, 1024, and 1600 elements. Displacement of each surface element in a horizontal (X) row was plotted against relative element position (Figure 4.4A). Subsequent mesh refinements between 8 and 1600 elements revealed decreasing changes in average element displacement across the entire surface of the mesh. Differences in the simulation predictions of each mesh were quantified by comparing the maximum displacement between each subsequent mesh refinement (Figure 4.4B). Similarly to the trends observed across the entire mesh surface, percent change between refinements decreased with increasing mesh density. Mesh refinement from 1024 to 1600 elements (the densest mesh examined), the change in predicted maximum displacement with refinement was less than 2%. Since the difference in simulation run time was negligible across all mesh densities, one additional refinement was performed and this 2000 element mesh was used for all subsequent examinations of scar distribution and size.

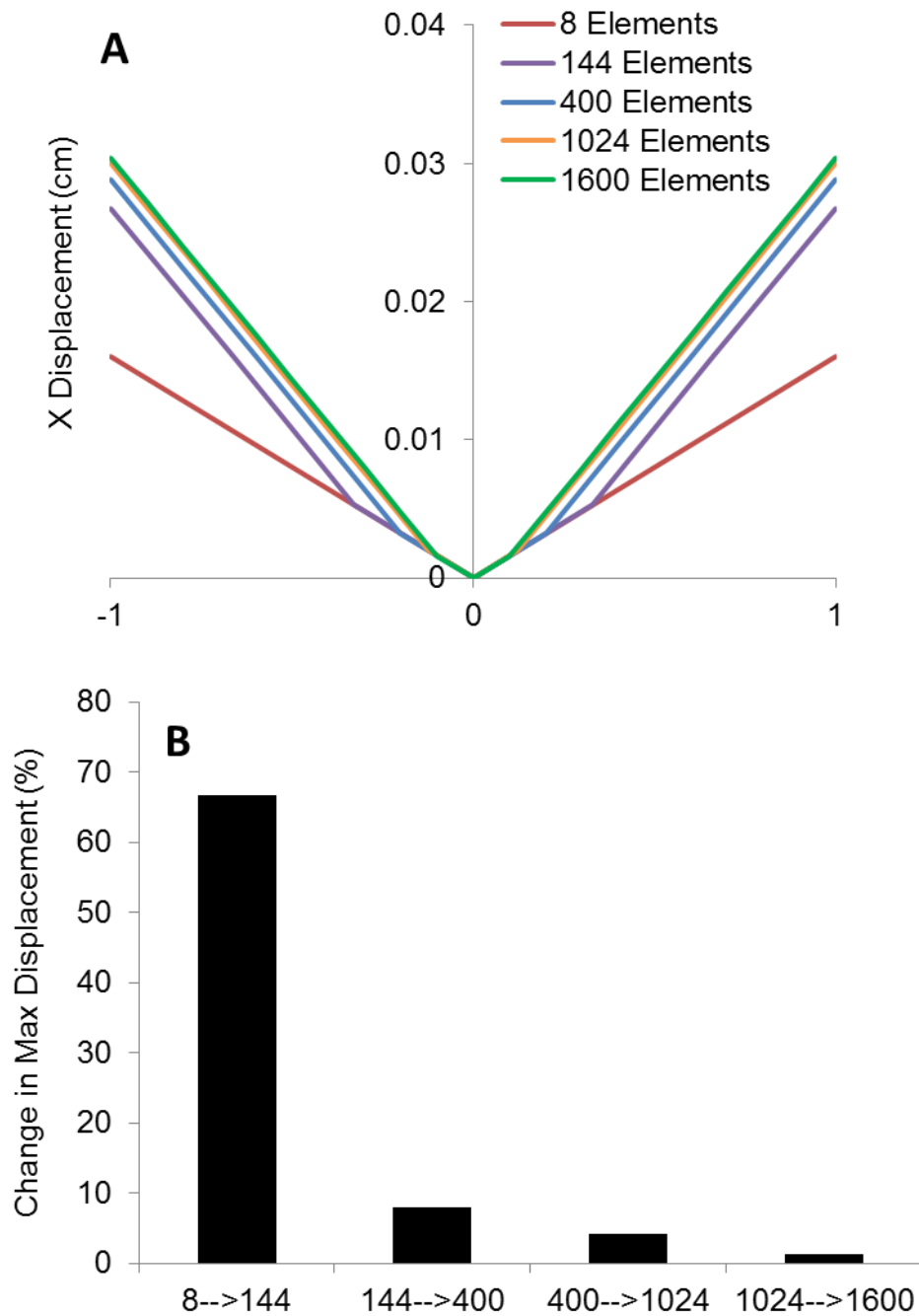


Figure 4.4 Mesh refinement study. (A) Average element displacements in the x-direction in an isotropic, equibiaxially loaded scar model. (B) Percent change in maximum displacement with each mesh refinement.

Models to examine the effects of scar distribution

In each scar distribution model, the total amount of scar (25% of sample volume) was defined to be the same and the distribution of scar was transmurally uniform. The six scar distributions examined are shown in Figure 4.5. A model with a large, central scar (“Center Scar”) was built to examine the effects of applying loads to muscle at the perimeter of the sample instead of directly to the scar region. Two additional models with a single scar region were constructed to investigate changes in measured behavior if only a subset of markers are in scar (“Mid Corner Scar”) and if some of the loads are applied in scar (“Corner Scar”). A more diffuse pattern of fibrosis was modeled as a distribution of small scar patches (“Dispersed Scar”). The effects of an anisotropic distribution (of mechanically isotropic scar) were examined with the final pair of models, one in which loads were applied in muscle (“Parallel Strips Short”) and one in which loads were applied in scar (“Parallel Strips Long”).

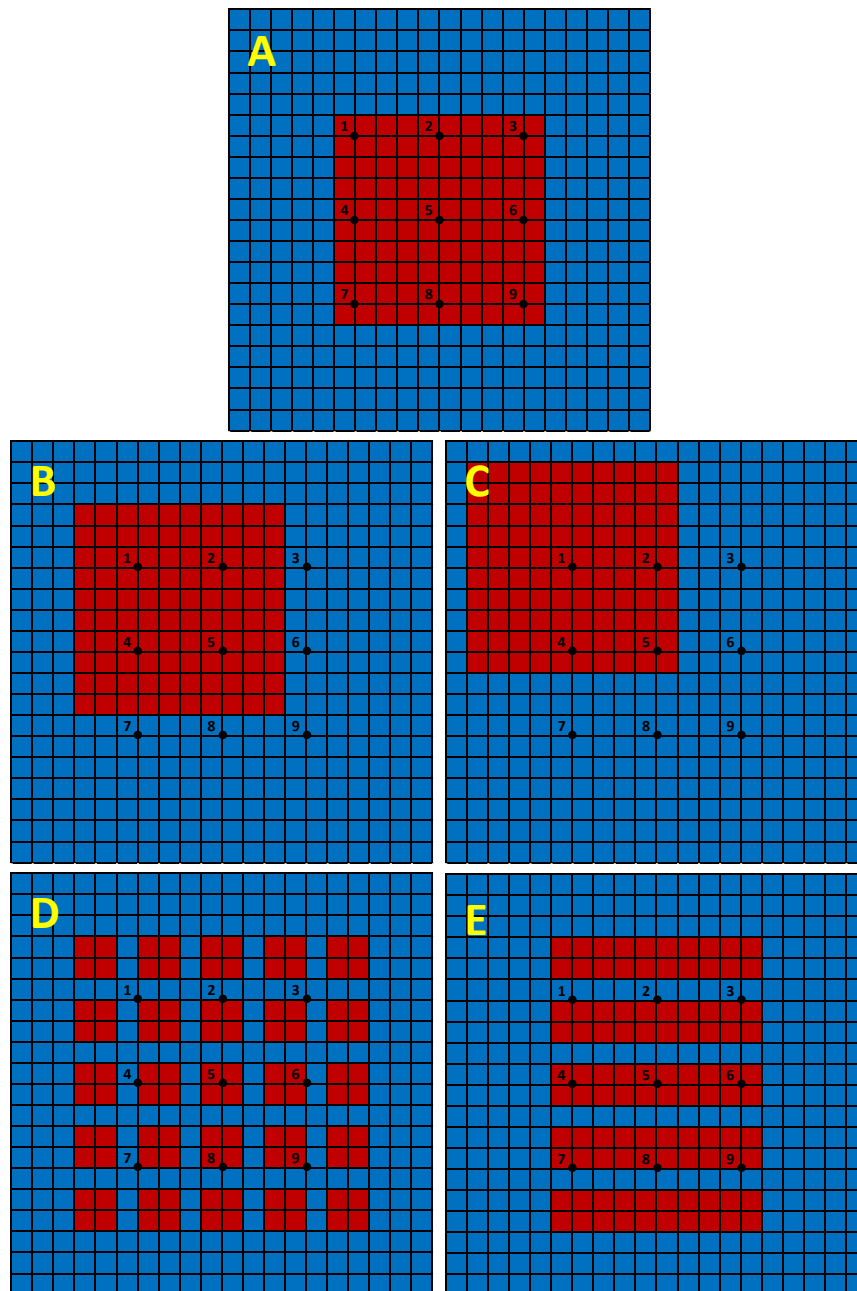


Figure 4.5 Models to examine the effects of scar distribution, with scar elements in red and muscle in blue. (A) Center Scar, (B) Mid Corner Scar, (C) Corner Scar, (D) Dispersed Scar, and (E) Parallel Strips.

Models to examine the effects of scar size

A separate set of models was built to examine the impact of the size of a single patch of scar on stress and strain in the scar region (Figure 4.6). Using the “Center Scar” model as a starting point, models of 16%, 9%, 4%, and 1% central scar (by volume) were constructed. Instead of calculating stress and strain using model outputs analogous to our experimental biaxial data, we examined average stress and strain in the shaded central region (Figure 4.6). Transmural averages of all elements in this region (4 elements \times 5 layers = 20 elements) as well as averages of only the surface elements (4 elements) were computed for comparison between models. Although we assume a state of plane stress in our biaxial analysis, the 3D finite element models allow us to examine the distribution of z-stress through the thickness of the sample. Although stress in the z-direction is 0 on each surface, this is not representative of the transmural distribution of stress in this direction. Therefore, average stresses using these two sets of elements were computed to detect any differences in transmural v. surface behavior. Since all models were perfectly symmetrical, we used stress and strain in the x-direction to represent the behavior of each model in the loading plane.

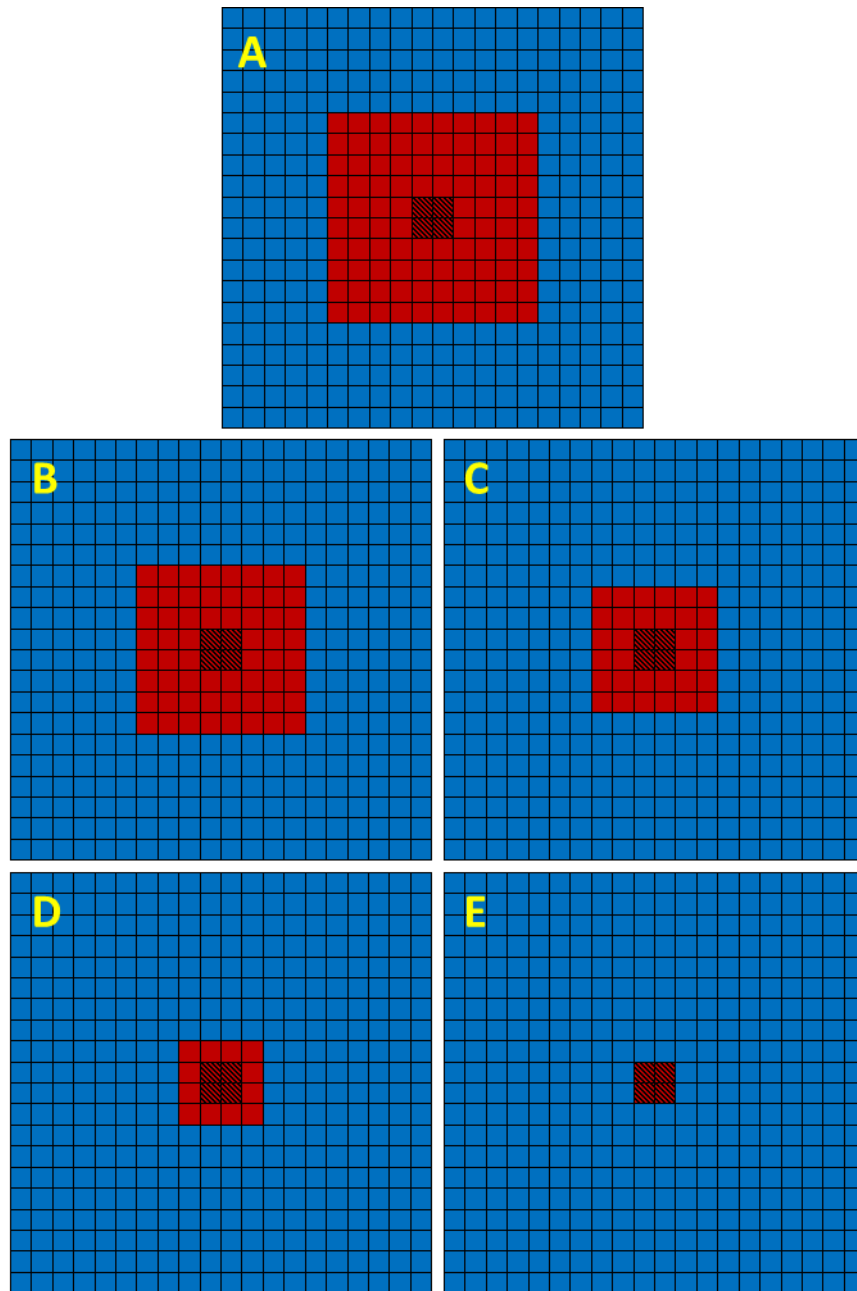


Figure 4.6 Models to examine the effects of scar size, with scar elements in red, muscle in blue, and the central region of scar used for average stress and strain shaded in gray. (A) The 25% scar model was identical to the Center Scar model, and symmetrical reductions in scar size produced (B) 16%, (C) 9%, (D) 4%, and (E) 1% scar models.

Results: Scar distribution

Since each model consisted of the same undeformed geometry (Figure 4.3) and was subjected to the same applied loads, average global 1st Piola-Kirchoff stresses calculated for each model were identical. Since the x and y dimensions of the sample were equal, stresses in the x and y directions were also equal. Therefore, we quantified the effects of scar distribution between models as differences in strain in the x (E11) and y (E22) directions. To determine the error in each model relative to the true scar behavior, the strains measured in each scar configuration were compared to those in the “All Scar” model. The absolute strains of each model were calculated using a subset of 4 markers (1,2,4,5), which were located entirely in scar in the Mid Corner and Corner Scar models. The same marker quadrant was used to calculate strains in the Dispersed and Parallel Strips models as well, even though no 4-marker quadrant in either model could be chosen to completely eliminate muscle elements. Each marker corresponded to a node on the surface of the mesh, so deformation of the grid was calculated from displacements of the selected nodes.

Strains calculated from the surface markers are shown in Figure 4.7. Although most models containing muscle slightly overestimated both axial strain components compared to the All Scar model, the differences in absolute strains were less than 1%. The two models with the greatest errors are the models in which the quadrant of markers used in the strain calculation was not composed entirely of scar (Dispersed Scar and Parallel Strips models). Interestingly, although the Parallel Strips model exhibited the largest strain error in the direction perpendicular to the scar (E22), this model also had the greatest accuracy in predicting E11. In the remaining models, in which the subset of markers was located entirely within a single patch of scar, absolute differences in strain were on the order of 0.3%.

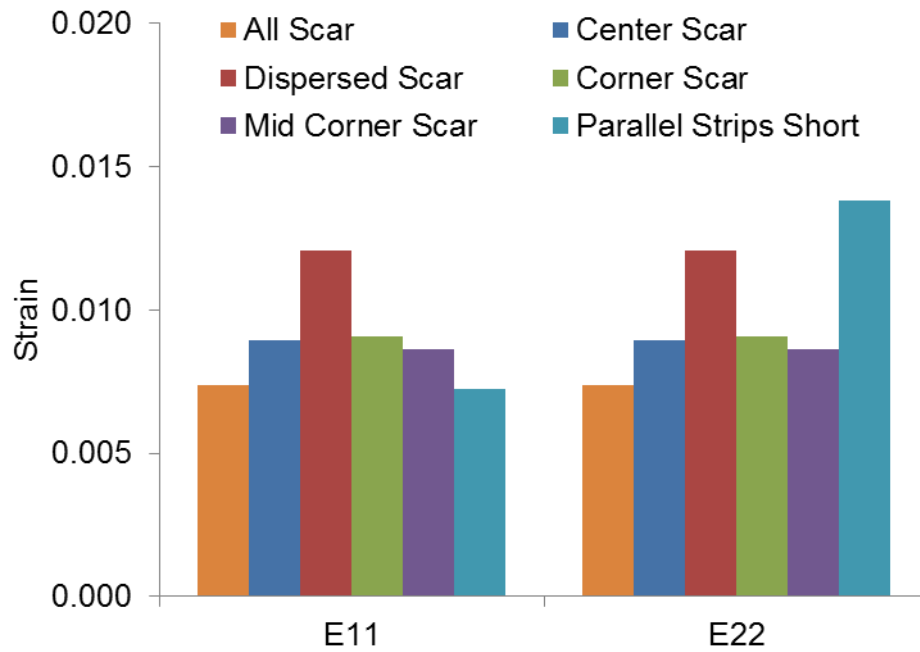


Figure 4.7 Absolute strains in each model at an equibiaxial stress of ~ 40 kPa. Across all models, differences in strain compared to the All Scar model were less than 1%. For the subset of models in which the four-marker grid used to calculate strains did not contain any muscle elements (Center Scar, Corner Scar, Mid Corner Scar), differences in absolute strains compared to the All Scar model were less than 0.3%.

Results: Scar size

We employed a separate group of five models to examine the effect of scar size (Figure 4.5). Rather than using our global, biaxial analysis methods to compare the behavior of each model, we chose to look at average stress and strain in the central elements in an effort to detect possible stress shielding of the scar. Stress and strain in the x-direction were averaged in the center of the scar in each model (shaded region in Figure 4.5), both transmurally (five layers of elements) and on the surface (1 layer of elements). Transmural averages of stress and strain were fairly stable among all scar sizes (Figure 4.8A). Compared to the All Scar model, a scar patch of any size experienced higher stresses and strains in the center of the infarct region. However, averages of the surface elements only (one transmural layer of elements) exhibited much more variation with scar size (Figure 4.8B). In the center of the scar region, the surface element averages of stress and strain increased with decreasing scar size.

In examining the surface distribution of stress in the x-direction across the entire geometry, we observed stress concentrations in the elements at the corners of each scar region, which constitute an increasing fraction of the scar region as the scar size shrinks, resulting in a higher average stress (Figure 4.9). We also examined the distribution of stress in the z-direction in a planar slice through the edge of the scar (Figure 4.10). In models of every scar size, elements on the scar border were under compression in the z-direction, with stress concentrations at the corners approximately three times higher than at the edge centers. Maximum compressive stresses at the infarct corners increased with decreasing scar size. Z-stress concentrations at the scar corners were accompanied by increases in x-stress in elements on the top and bottom surfaces of the geometry, which increased in magnitude with decreasing scar size (Figure 4.11)

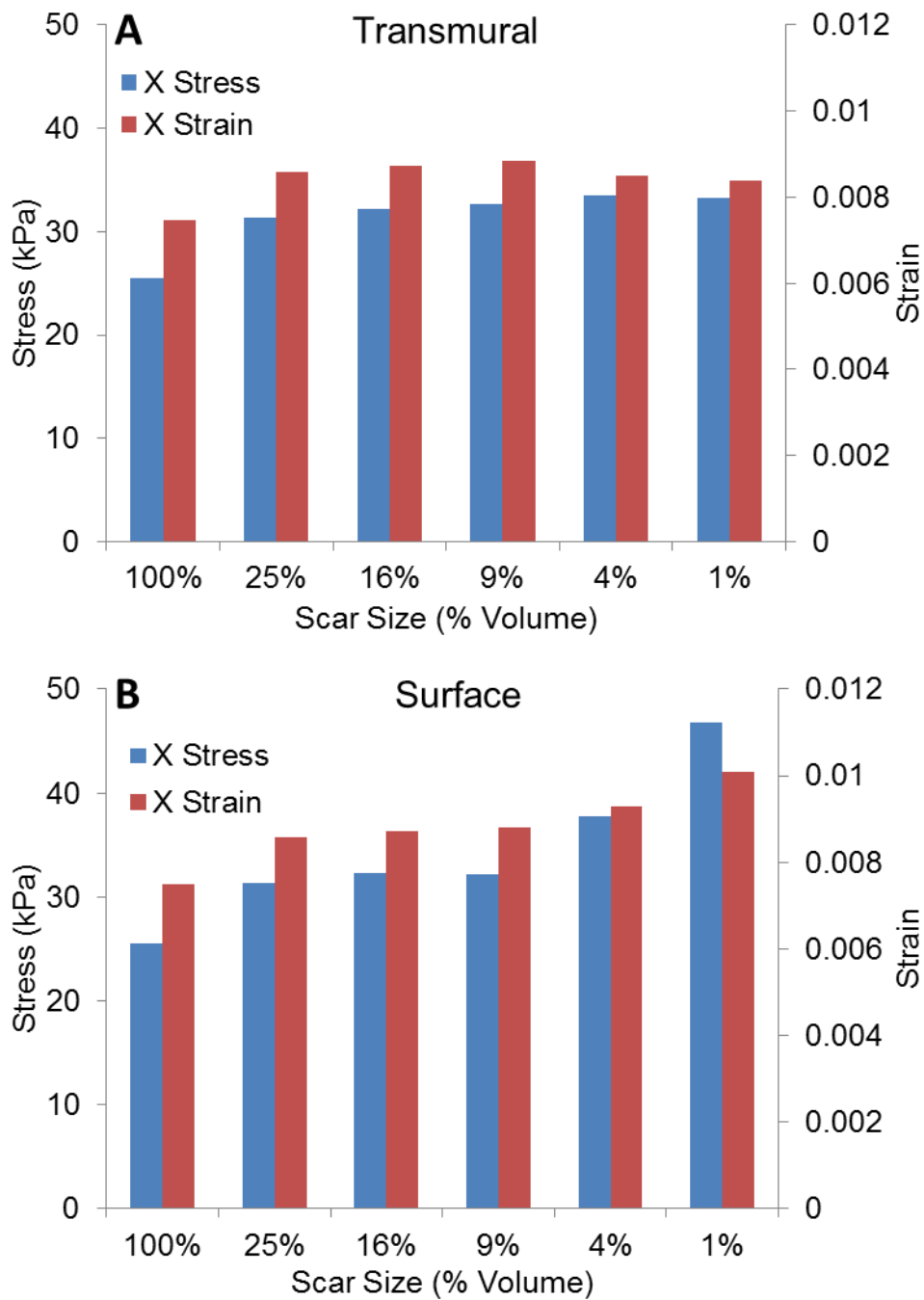


Figure 4.8 Stress and strain in the center region of infarcts of decreasing size, averaged across elements in (A) all five transmural layers and (B) a single transmural layer on the surface.

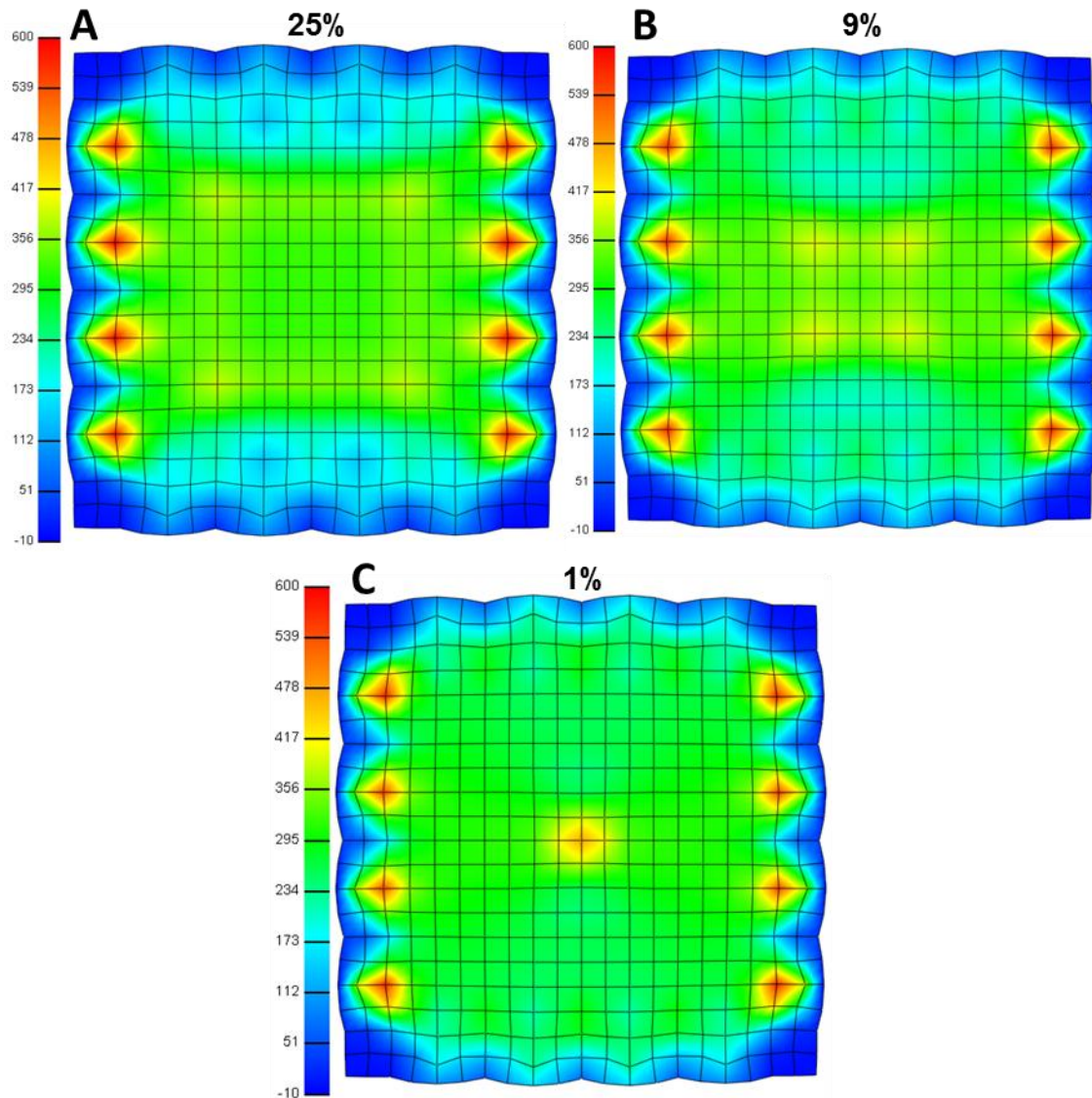


Figure 4.9 Distribution of stress (in g/cm^2 , with a scale of -10 to 600 g/cm^2 approximately corresponding to a scale of -1 to 60 kPa) in the x-direction across in the (A) 25%, (B) 9%, and (C) 1% scar models. Stress concentrations were observed at the corners of the scar region in each model.

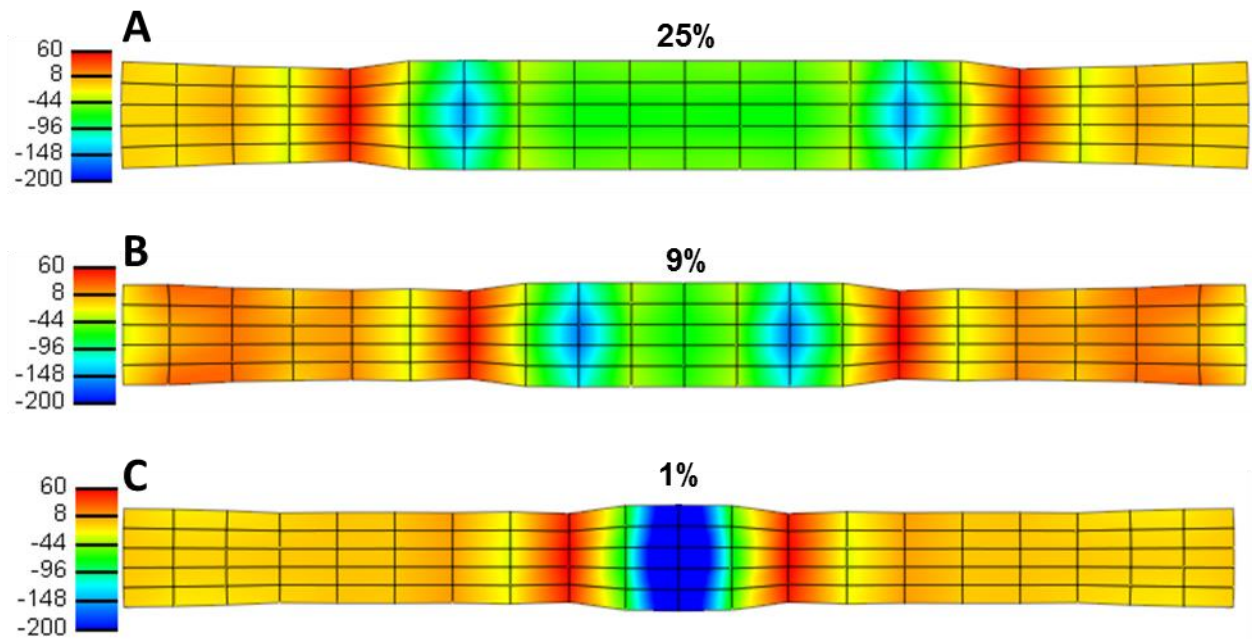


Figure 4.10 Distribution of stress in the z -direction (in g/cm^2 , with a scale of -200 to $60\text{g}/\text{cm}^2$ approximately corresponding to a scale of -20 to 6 kPa) in a planar cut along an edge of the scar region in the (A) 25%, (B) 9%, and (C) 1% scar models. The maximum compressive stress at the scar corners increased with decreasing scar size.

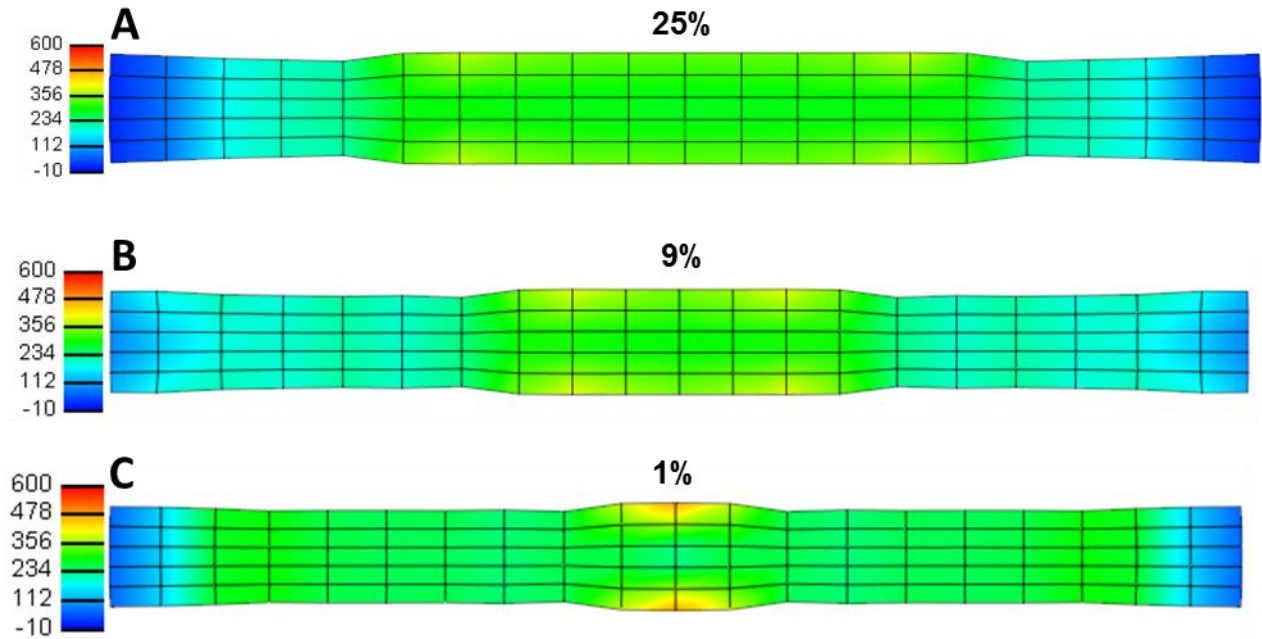


Figure 4.11 Distribution of stress in the x-direction (in g/cm^2 , with a scale of -10 to $600\text{g}/\text{cm}^2$ approximately corresponding to a scale of -1 to 60 kPa) in a planar cut along an edge of the scar region in the (A) 25%, (B) 9%, and (C) 1% scar models. Tensile stress in the x-direction was highest at the scar corners, in elements on the top and bottom surfaces.

Discussion

In order to better understand the effects of sample heterogeneity on global biaxial test data, we built a series of finite element models to examine regional deformations in biaxial test samples containing scars of different sizes and in various locations. To isolate the effects of scar distribution, we compared models containing large regions of scar, smaller dispersed scar patches, and parallel strips of scar, while keeping the total volume of scar equal across models. A separate series of models were built to examine the effects of scar size, all utilizing a single, central region of scar. In general, the models suggested that data from samples containing a large patch of scar can be used to generate accurate strain measurements, provided that at least a subset of the marker grid is located entirely in scar.

Across all scar distribution models, we observed errors in calculated strains that were less than 1% compared to the idealized model consisting entirely of scar. Given that the glass bead markers used in our biaxial experiments were approximately 1mm in diameter and the total width of each patch sample was at least 5cm, each marker represented at least 2% of the sample width. Since the hooks used to apply loads were inserted a small distance away from the sample edge, the relevant sample width inside the area of applied load is even smaller than 5cm, meaning that each marker accounts for over 2% of the sample dimensions. Therefore, small errors in the optical identification and tracking of the center of each marker during the experiment could produce errors on the order of 2%. Comparing this estimation with the model predictions, we postulate that the errors arising from heterogeneous distributions of scar are on the same order as errors in our experimental measurements. However, considering only those models that did not include muscle elements in the strain calculation (Center Scar, Corner Scar, Mid Corner Scar), the errors in strain were even

smaller (0.3% or less). Therefore, in models with a subset of markers in a single scar region, we conclude that the errors arising from our experimental measurement methods were likely larger than the errors due to the presence of surrounding muscle.

Of all the scar distributions examined, the error in strain that would be computed from global, homogenous analysis in a typical biaxial testing experiment was largest in the Parallel Strips model, in the direction perpendicular to the alignment of the scar regions. Interestingly, however, this model also exhibited the greatest strain accuracy in the direction parallel to the scar strips. In this scar configuration, the displacements of markers (located in scar) in the direction parallel to the slits led to very accurate estimations of E_{11} , almost as if a uniaxial tensile test had been performed on the scar alone. However, this “uniaxial” accuracy cannot be assumed or extended to experimental data, where non-isotropic, fibrous materials with a greater degree of mechanical coupling between the two in-plane directions will all contribute to errors in biaxially measured strains. In samples where no subset of markers located entirely in scar exists (such as the Dispersed Scar model), or in which the distribution of scar is more complex than those represented in the above models (e.g. larger transmural variations).

We used a separate set of models to examine the effect of scar size for a single patch of scar in the same location (Center Scar). Compared to the All Scar model, models with a central scar region showed an approximate 20% increase in stress and a 15% increase in strain in the center of the scar, which when averaged transmurally was stable across all scar sizes. However, averaging in-plane stress and strain in the surface elements only revealed a threshold in scar size around 9% scar, below which the accuracy of the averages in the center of the scar began to fall off rapidly.

We examined distributions of in-plane and transmural stress and discovered stress concentrations at the scar corners. These stresses were compressive in the z -direction, leading to increases in in-plane stress and strain along the scar borders by material incompressibility. Tensile stress concentrations in the x - y plane were also observed at the scar corners, in the layers of elements on the top and bottom surfaces. These stresses arise from the requirement that both the top and bottom surfaces be traction free, necessitating that compressive stresses in the z -direction on either face are relieved by in-plane stretching in the other two dimensions. This gives rise to the parabolic profile of transmural stress in the z -direction, in which compressive stress was highest in the central transmural layer of elements. However, these stress concentrations at the scar corners only affected the accuracy of the results in small scars, where these corner elements were also close to the central scar region where stress and strain were quantified. In models where the region of scar size was approximately 10% or larger (9% by volume of entire sample, 11% of the volume between the applied loads), the edges of the scar were sufficiently distant from the center, leading to stable averages between scar sizes.

Conclusion

We observed that average stress and strain in fractional scar models of all sizes were slightly higher than in the All Scar model. Although scar-specific models may hold potential to further improve the accuracy of measured material properties in complex, heterogeneous samples, we found that in general the errors in measured strains due to sample heterogeneity were on the same order or smaller than estimated errors in our biaxial experimental measurements. As a practical guide to analyzing biaxial test data from samples with variable amount and distributions of scar, we conclude that: 1) we can assume reasonable accuracy of biaxial test data for samples with at least a subset of

4 markers in a single patch of scar, and 2) measurement of surface deformation is relatively unaffected by scar size above a threshold of approximately 10% scar.

References

Demer, L. L., & Yin, F. C. P. (1983). Passive biaxial mechanical properties of isolated canine myocardium. *Journal of Physiology*, 339, 615–630.

Grashow, J. S., Yoganathan, A. P., & Sacks, M. S. (2006). Biaxial stress-stretch behavior of the mitral valve anterior leaflet at physiologic strain rates. *Annals of Biomedical Engineering*, 34(2), 315–325.

Maas, S., Ellis, B., Ateshian, G., & Weiss, J. (2012). FEBio: finite elements for biomechanics. *Journal of Biomechanical Engineering*, 134(1).

Veronda, D. R., & Westmann, R. A. (1970). Mechanical characterization of skin-finite deformations. *Journal of Biomechanics*, 3(1), 111–24.

Chapter 5

Finite Element Model of Left Ventricular Infarct Restraint

A finite element model of acute, anterior infarction in the left ventricle was developed to determine the optimum infarct reinforcement strategy. This model predicted dramatic improvement in LV function with longitudinal infarct stiffening, and an acute *in vivo* study in dogs confirmed the effectiveness of longitudinal reinforcement. However, a follow-up study of chronic restraint showed no sustained benefits of longitudinal stiffening. We hypothesize that the lack of sustained benefit is due to substantial scar compaction during healing, which relieves patch tension and negates the effects of the therapy. Therefore, we constructed a new finite element model of the infarcted left ventricle to explore the dynamic interplay between mechanical reinforcement therapies and changes in scar dimensions.

Left ventricular geometry

We built a finite element model to simulate acute infarct reinforcement and subsequent scar remodeling. In brief, model geometry was based on MR images of a single control animal from our chronic reinforcement study (Chapter 3), chosen because the minimum cavity volume of this animal was most similar to the estimated experimental unloaded cavity volume. Passive and active myocardial material parameters were chosen to match the baseline (pre-infarction) end-diastolic and end-systolic pressure-volume relationships measured invasively in our acute reinforcement study (Chapter 2). The acute infarct and reinforcement models were then evaluated and refined based on their ability to reproduce local strains and global pressure-volume behavior measured during the acute study, before proceeding to simulations of chronic scar remodeling. Each step of model development and validation is described in more detail below.

Canine left ventricular geometry was generated from the 48 hour post-MI MR images of an infarcted control (non-reinforced) animal (CP09). The endocardium (excluding papillary muscles) and epicardium were manually traced on the SA CINE stack using Segment (Heiberg et al., 2010). The anterior and posterior RV insertion points were marked on a single, mid-ventricular SA slice using the endocardial pin points feature. Pin points were also used to mark the most apical endocardial point and the center of the mitral valve on a single LA image. Although none of the frames in the CINE time series represent the undeformed geometry since the LV is never fully unloaded during the cardiac cycle, contours of the frame immediately following end systole (beginning of isovolumic relaxation) were used as the closest possible estimation of the unloaded LV configuration. The unloaded geometry was then estimated by scaling this digitized end-systolic geometry as detailed below.

Short axis LV contours were exported from Segment into MATLAB. The SA contours of the endocardium and epicardium were re-interpolated to generate a fixed number of equally spaced points around the circumference of each slice. The landmarks identified by short and long-axis pinpoints were used to construct a new set of axes reflecting the apex-base, septal-lateral, and anterior posterior directions. The interpolated stack contours were converted from image (pixels) into distance (cm) coordinates and rotated into the landmark coordinate system. The transformed stack points were converted to prolate spheroidal coordinates, and scaled in lambda by a factor of 0.85 to match the experimental unloaded cavity volume. Average unloaded cavity volume of the animals in the acute experiment was estimated by fitting the average baseline end-diastolic pressure-volume relationship with an exponential curve, and then extrapolating to a cavity pressure of 0mmHg to find the volume intercept. The scaled points were fit with a 16 element prolate spheroid using Continuity (Figure 5.1A-B). The mesh was refined in the prolate spheroidal coordinate system, resulting in a denser mesh with controlled element densities in the circumferential, longitudinal, and radial directions. Coordinates of the refined nodes were passed from Continuity back to MATLAB to define the mesh structure. Nodal connectivity was specified to generate 8-node hexahedral elements throughout the mesh. The connectivity of the hexahedral elements used throughout the mesh required that a small hole be left open at the apex. However, significant torsion of the ventricle during inflation and contraction caused convergence problems at the apex, as surfaces of elements that were in close proximity but were not actually connected came into contact with one another. To prevent excess element shear and surface contact, two rows of elements were deleted from the apex (transmurally) to expand the hole and prevent elements from contacting one another. A large, transmural infarct region was defined on the anterior wall and apex of the LV (Figure 5.1C). The number of infarct elements was chosen to provide an infarct size similar to the average 48 hour infarct size of the chronic study animals (~33%).

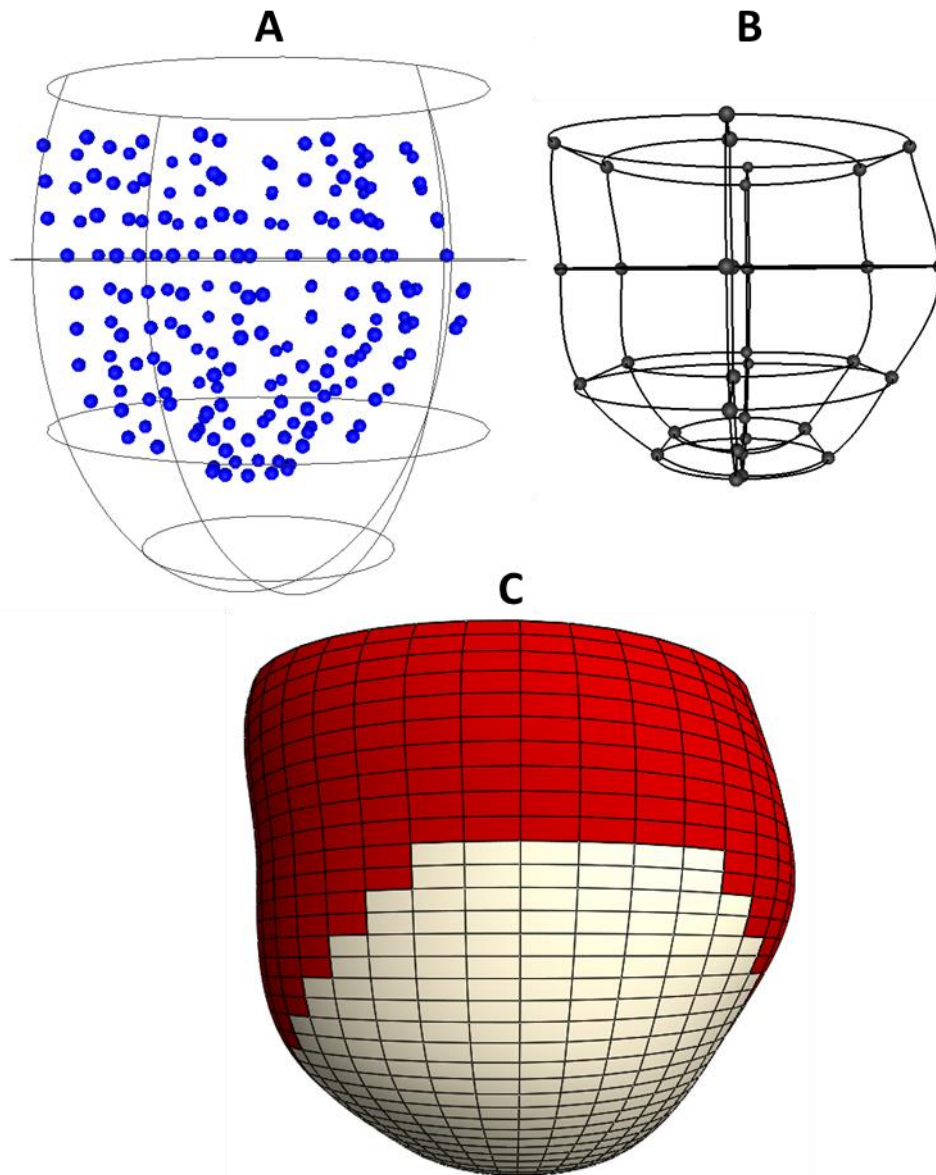


Figure 5.1 Left ventricular mesh generation. (A&B) Endo- and epicardial contour points from the SA MR images were fitted to a 16 element prolate spheroidal mesh. (C) The resulting mesh was refined in 3 dimensions and partitioned into muscle (red) and infarct (white) regions.

Muscle material properties

All finite element simulations were performed in the FEBio software suite (Maas, Ellis, Ateshian, & Weiss, 2012). Passive myocardium was modeled using a transversely isotropic Mooney-Rivlin material, which models the elastic response of the tissue as the combined response of fibers embedded in an isotropic matrix. This constitutive model takes the form:

$$\Psi = W_1(I_1, I_2) + W_2(\tilde{\lambda}) + \frac{K}{2} [\ln(J)]^2$$

where W_1 represents the isotropic Mooney-Rivlin ground matrix and W_2 represents the contribution of the fibers. I_1 and I_2 are the first and second invariants of the deviatoric part of the Right Cauchy Green deformation tensor (\tilde{C}), J is the determinant of the deformation gradient, and $\tilde{\lambda}$ is the deviatoric part of the stretch in the fiber direction:

$$\tilde{\lambda}^2 = a_0 \cdot \tilde{C} \cdot a_0$$

where a_0 is the initial fiber direction. The isotropic component is represented as:

$$W_1 = c_1(I_1 - 3) + c_2(I_2 - 3)$$

where c_1 and c_2 are the Mooney-Rivlin material coefficients. The contribution of the fibers is modeled using piecewise functions of fiber stretch:

$$W_2(\tilde{\lambda}) = 0, \quad \tilde{\lambda} \leq 1$$

$$W_2(\tilde{\lambda}) = c_3(e^{-c_4}(E_i(c_4\tilde{\lambda}) - E_i(c_4) - \ln\tilde{\lambda})), \quad 1 < \tilde{\lambda} < \lambda_m$$

$$W_2(\tilde{\lambda}) = c_5(\tilde{\lambda} - 1) + c_6 \ln \tilde{\lambda}, \quad \tilde{\lambda} \geq \lambda_m$$

Here E_i is the exponential integral function, resulting in fiber stress contributions evaluated as:

$$\tilde{\lambda} \frac{\partial W_2}{\partial \tilde{\lambda}} = 0, \quad \tilde{\lambda} \leq 1$$

$$\tilde{\lambda} \frac{\partial W_2}{\partial \tilde{\lambda}} = c_3(e^{c_4(\tilde{\lambda}-1)} - 1), \quad 1 < \tilde{\lambda} < \lambda_m$$

$$\tilde{\lambda} \frac{\partial W_2}{\partial \tilde{\lambda}} = c_5 \tilde{\lambda} + c_6, \quad \tilde{\lambda} \geq \lambda_m$$

In this model, λ_m is the stretch at which fibers are uncrimped, c_3 is the scaling factor for exponential stress, c_4 is the fiber uncrimping rate, c_5 is the modulus of straightened fibers, and c_6 is calculated to force stress continuity at λ_m . Fiber stress is defined as 0 for fiber stretches less than 1 so that fibers only sustain tension; the stress response of elements under compression is governed completely by the isotropic component. In our model, λ_m was set to a fiber stretch value far above what could ever be observed physiologically ($\lambda_m = 10$) to avoid the piecewise transition to the linear portion of the fiber law. This way, fibers under tension were modeled using only the exponential portion of the fiber law.

A single fiber angle was defined in each element. A transmural distribution of muscle fiber angles was generated based on the measurements made in canine myocardium by Streeter (Streeter, Spotnitz, Patel, Ross, & Sonnenblick, 1969). Fiber angles of 80°, 45°, 10°, -25°, -60° were defined in the endocardial, sub-endocardial, midwall, sub-

epicardial, and epicardial transmural element layers, respectively. Rotation between the global Cartesian and local cardiac coordinate systems was accomplished using a strategy developed by Meier (Meier, Ziskin, Santamore, & Bove, 1980). At a single node in each element, a local, radial unit vector is defined, which is perpendicular to the endocardial surface. A unit vector tangent to the element surface was found by finding the normal vector to the plane containing the base-apex axis and the single element node. This vector was crossed with the radial vector to find the local longitudinal axis, and finally the local longitudinal and radial vectors were crossed to find the local circumferential vector. The resulting rotation matrix consisting of these three vectors was used to convert element input (fiber angle) and output (strain, stress) parameters between the local element and global Cartesian coordinate systems.

Values of the passive material coefficients were chosen so that the model EDPVR passed through the interpolated points of the average baseline EDPVR of the acute study animals. Passive myocardium was modeled using: $c_1 = 0.8$, $c_2 = 0$, $c_3 = 0.05$, $c_4 = 23$, $c_5 = 350$, $\lambda_m = 10$. The bulk modulus was set to $k=250$ to minimize compressibility while preserving a bulk:shear ($k:c_1$) ratio between 100 and 1000. Active contraction of the muscle was modeled as a length-dependent active stress (T_a) in the fiber direction, following the time-varying elastance model of Guccione (Guccione & McCulloch, 1993).

$$T_a = \left(\frac{Ca_0^2}{Ca_0^2 + ECa_{50}^2} \right) C(t)$$

$$ECa_{50} = \frac{Ca_0}{\sqrt{e^{B(\lambda_f l_r - l_0)} - 1}}$$

Here Ca_0 is the peak intracellular calcium concentration, B is the tension-sarcomere length relation constant, λ_f is the fiber stretch, l_r is the unloaded sarcomere length, l_0 is

the sarcomere length below which no tension develops, and $C(t)$ is a user-defined load curve used to scale the maximum isometric stress. In our model, we used values of $Ca_0 = 4.35\mu\text{M}$, $B = 4.75\mu\text{m}^{-1}$, $l_r = 1.2\mu\text{m}$, and $l_0 = 1.58\mu\text{m}$. The maximum isometric stress was linearly increased from 0 to 135kPa (Guccione, Waldman, & McCulloch, 1993) during active contraction. The maximum isometric stress was assumed to be the same in all muscle elements, while we assumed no active stress generation in all infarct elements. To prevent expansion and shape change of the apical hole during loading, the single, transmural ring of elements directly surrounding the apical hole was partitioned and assigned as a stiff, isotropic Mooney-Rivlin material: $c_1 = 500$, $c_2 = 500$, $k = 5000$.

Mesh refinement Study

A mesh refinement study was performed to determine the optimum density of the final mesh. To balance accuracy with computation time, we sought to determine the lowest mesh density that produced stable results compared to further refinements. Several meshes of increasing refinement were created to examine distributions of strains in the infarct region with increasing mesh density. Meshes consisting of 1280, 2880, 5120, 8000, and 18000 elements were constructed, keeping the number of transmural elements fixed at five in each model. Midwall strains in a circumferential ring of elements passing through the center of the scar were used to examine the effects of refinement on simulated deformation in the muscle, border zone, and infarct (Figure 5.2). Changes between refinements were evaluated quantitatively using the in-plane strains at the center of the infarct (Figure 5.3). We observed stability of infarct strains between the 8000 \rightarrow 18000 element mesh refinements (percent changes in all strains were less than 2%), accompanied by a dramatic increase in simulation time. Therefore, the 8000-element model was selected as the optimum mesh. However, as described above in the “Left ventricular geometry” section, two rows of elements were removed from the apex

to prevent convergence problems due to element torsion. Therefore, the resulting mesh had the same element density as the 8000 element mesh but with slightly fewer elements. This final 7600-element mesh was used for all subsequent simulations.

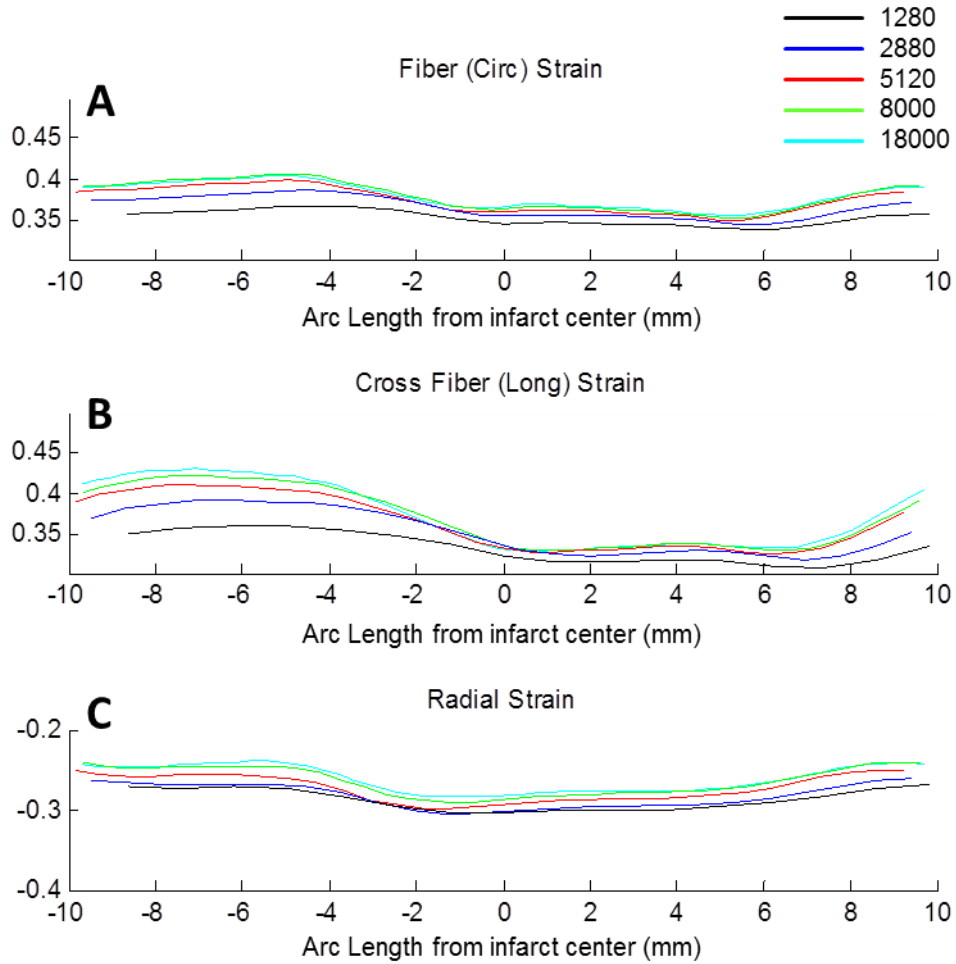


Figure 5.2 (A) Circumferential, (B) longitudinal, and (C) radial strains in a circumferential ring of elements (where 0 is the center of the infarct) for meshes of increasing element density. In all three dimensions, the magnitudes of changes in infarct and remote strains decreased with subsequent mesh refinements. Changes in in-plane strains in each region are quantified in Figure 5.3.

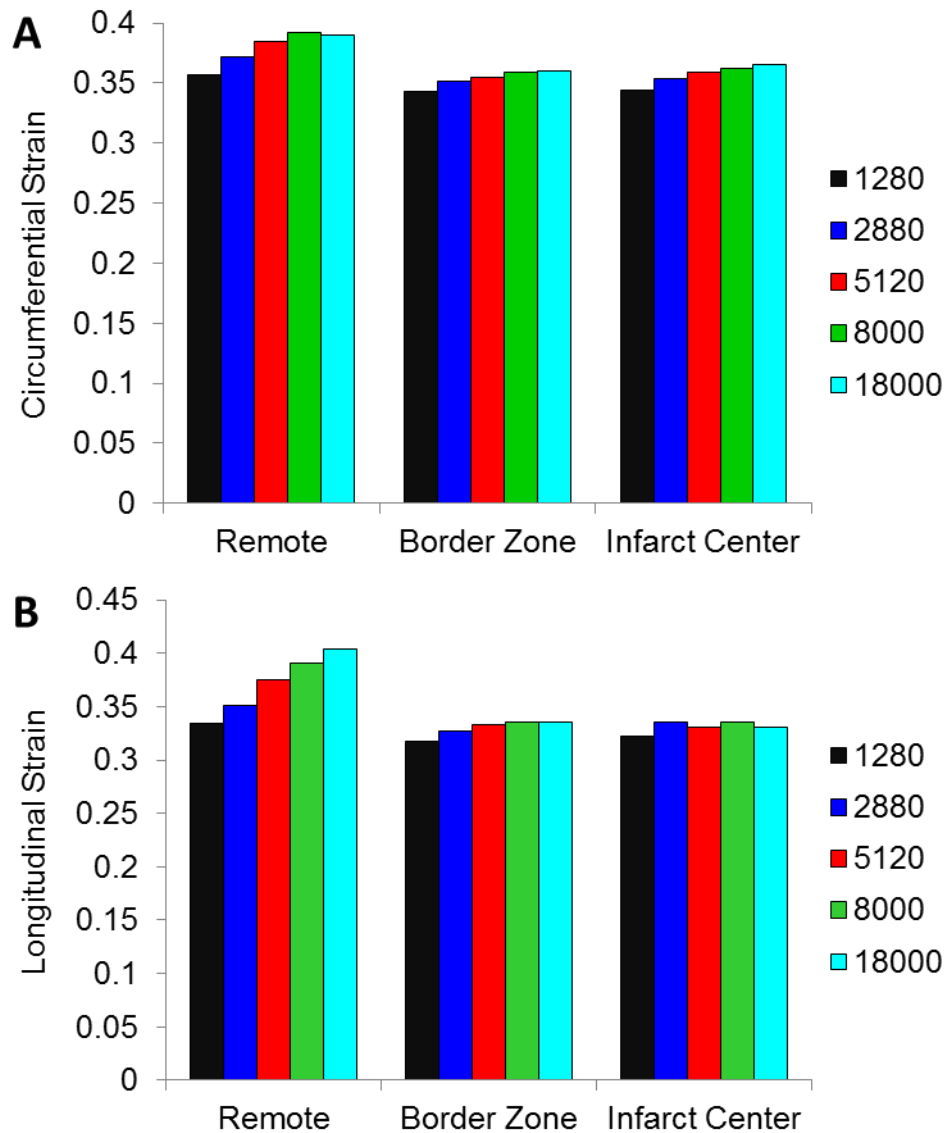


Figure 5.3 (A) Circumferential and (B) longitudinal strains at the midwall in the remote, border zone, and infarct regions in meshes containing 1280, 2880, 5120, 8000, and 18000 elements. In each region, increasing element density led to slight increases in strain, with diminishing returns for each subsequent refinement.

Acute infarct & patch material properties

Previous finite element models have assumed that an acute infarct can be represented using the same material law and coefficients as passive myocardium. However, data from our acute patch study suggested that the acute infarct was remodeling, even after only 45 minutes of ischemia. Remodeling strains were calculated to reflect changes in infarct dimensions between baseline→ischemia and baseline→patch. Remodeling strains were calculated from segment lengths interpolated at matched values of EDP across states, ensuring that changes in infarct dimensions reflect actual differences in mechanics rather than differences in loading (LV pressure). On average, the infarcts in our acute canine study underwent significant expansion in both the circumferential and longitudinal directions (Figure 2.5A). However, assuming no changes in acute infarct geometry or material properties in an acute infarct FE model eliminates the possibility of matching the experimental remodeling data. Hypothesizing that restraint of this acute infarct expansion might partially contribute to the restoration of function we observed with acute patch application, we explored two mechanisms of generating larger infarct stretches in response to the same load:

- 1) A reduction in infarct wall thickness with no change in material properties
- 2) Softening of the acute infarct material

A morphometric study examining the relationship between capillary structure and coronary perfusion pressure in the canine heart found that capillaries constitute 4-6% of the total myocardial wall volume (May-Newman, Mathieu-Costello, Omens, Klumb, & McCulloch, 1995). Therefore, a loss of coronary perfusion pressure following ligation could translate into a loss of capillary volume and a subsequent decrease in infarct wall thickness. Assuming constant infarct material properties and LV cavity pressure, a

thinner infarct will experience higher stresses and undergo greater in-plane stretching than an infarct with preserved wall thickness. To determine whether this mechanism could explain the infarct expansion we observed in our acute data, we removed the fibers and softened the isotropic component of the elements in the epicardial layer of the infarct ($c_1 = 0.01$, $c_2 = 0$, $k = 100$). We evaluated remodeling by comparing the longitudinal strains resulting from passive inflation of the LV to a cavity pressure of 12mmHg between baseline \rightarrow ischemia and baseline \rightarrow patch states. Effectively thinning the infarct wall by dramatically softening the epicardial layer of elements resulted in midwall strains that agreed well with the experimental remodeling (Figure 5.4, red bars).

Patch reinforcement was also simulated by modification of the material properties of the elements in the epicardial layer of the infarct. To impose stiff, longitudinal reinforcement, longitudinally oriented fibers were defined in the epicardial infarct layer and the fiber coefficients of the transversely isotropic Mooney-Rivlin material model were increased ($c_3 = 10$, $c_4 = 100$). Upon adding this restraint to the acute infarct model, we observed that simulating acute infarct wall thinning by softening the epicardial layer of infarct elements led to longitudinal remodeling within one standard deviation of our experimental averages in both the ischemia and patch states. Unfortunately, however, subsequent models built using this approach had problems with convergence, presumably due to the combination of very stiff fibers embedded in an extremely soft matrix.

Therefore, we decided to explore whether transmural softening of the acute infarct could also match our experimental remodeling data. Simulating acute softening by decreasing the remaining isotropic coefficient in the Mooney-Rivlin material model ($c_1 = 0.4$), we observed that this approach predicted longitudinal remodeling that matched

our experimental data as well as the wall thinning approach (Figure 5.4, green bars). Although softening of the infarct material is perhaps a less physiological representation of acute infarct expansion than infarct wall thinning due to loss of perfusion pressure, we were able to use both approaches to match our experimental remodeling data. Therefore, we used the transmural infarct softening approach in all subsequent simulations of reinforced and unreinforced acute infarcts. The patch layer was also modeled using a transversely isotropic Mooney-Rivlin material model, with isotropic coefficients chosen to match acute infarct ($c_1 = 0.4$, $c_2 = 0$, $k = 500$). The material coefficients describing the longitudinal fibers were increased dramatically to represent a longitudinally inextensible patch, until the magnitude of restraint at an EDP of 12mmHg matched our experimental remodeling data (Figure 5.4).

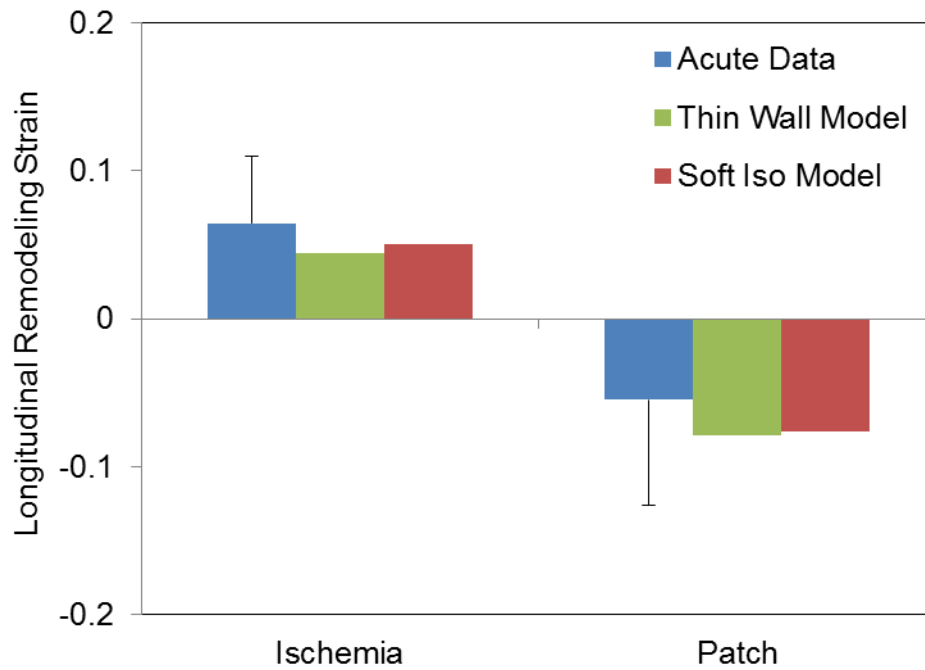


Figure 5.4 Infarct remodeling strains (between baseline and 45 minutes of ischemia) from the acute patch canine study (blue). Both simulated infarct wall thinning and isotropic infarct softening were able to replicate the acute infarct expansion data.

Chronic scar material properties

Our finite element simulation of a heterogeneous biaxial test sample predicted negligible errors in experimentally measured strains, provided that the markers used in the displacement calculation were all located in a single, large region of scar. A biaxial sample was selected that had a large region of dense scar (CP45, endocardium), containing six out of nine of the surface markers (Figure 5.5A). Biaxial loads and displacement data for the bottom two rows of markers (those located in scar) were imported into MATLAB. Strains were calculated according to the method described in Chapter 4, and axial stresses were determined from dividing the axial loads by the specimen cross-sectional area (CSA). Sample CSA was estimated by:

- 1) measuring the distance between the outer hooks on each edge of the sample
- 2) averaging the two distances along each axis to determine the average length and width of the area of the sample to which load was applied
- 3) averaging the thickness measurements made with calipers at five different locations throughout the sample on the day of the experiment
- 4) multiplying the average thickness value with the average length and width values to estimate the sample CSA along the x- and y-axes.

Four biaxial loading protocols that covered a wide range of the E11-E22 stretch plane were selected (Figure 5.5B):

- 1) 250g in X1, 750g in X2
- 2) 350g in X1, 750g in X2
- 3) 500g in X1, 750g in X2
- 4) 750g in X1, 750g in X2

The “All Scar” biaxial test finite element model was employed to estimate the material properties of the stiff, compacted scar. The axial strains of the CP45 specimen suggested that the sample was stiffer in the X2 direction, since the equibiaxial loading protocol (#4, 750g in X1, 750g in X2) resulted X1 strains (circumferential direction) that were more than twice as large as strains in X2 (longitudinal direction). Therefore, longitudinal fibers were added to the All Scar model, and a transversely isotropic Mooney-Rivlin material model was used. The four loading protocols were simulated by modifying the nodal forces applied to each edge. The isotropic and fiber coefficients were manually adjusted to identify the single set of coefficients that produced the best match to the strain data from all four loading protocols: $c_1 = 400$, $c_2 = 400$, $k = 40000$, $c_3 = 200$, $c_4 = 32$. This set of coefficients led to good agreement with the experimental ratios of E11 and E22 for each protocol, although our model underestimated the degree of mechanical coupling between the X1 and X2 directions, leading to under- or overestimation of the maximum strains for some protocols. However, the lack of mechanical coupling in the model is not surprising, since we assumed a uniform distribution of longitudinal fibers, whereas the experimental fiber distribution is much more complex, heterogeneous, and transmurally variable.

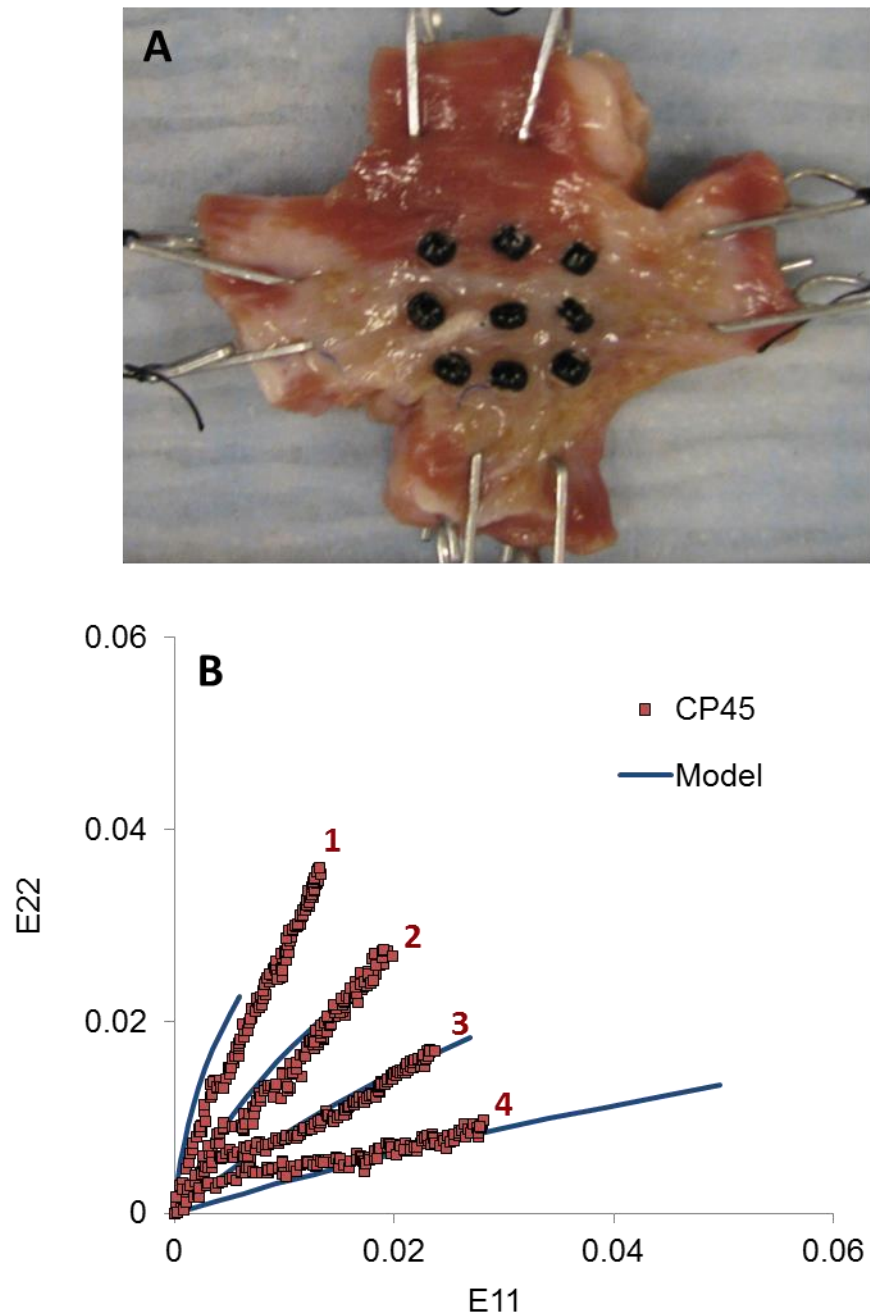


Figure 5.5 Estimation of scar mechanical properties at 8 weeks. (A) Biaxial test data from the CP45 endocardial section was used for fitting. (B) The “All Scar” biaxial test finite element model was used to simulate multiple loading protocols and tune the scar material coefficients to match the experimental biaxial stretch response.

Scar compaction

Compaction of the scar was simulated in FEBio using the in-situ strain plugin. This feature allows addition of a residual stress/initial strain distribution to the unloaded mesh, while preserving the undeformed geometry. To generate longitudinal scar compaction in the epicardial plane, a uniform tensile pre-stretch was applied in all infarct elements, in the local fiber direction. Since the tensile residual stress was applied to the undeformed geometry without imposing any deformation, balance of the resulting forces produced in-plane compression of the scar and establishment of a new reference geometry containing the compacted scar. The degree of initial scar compaction was modulated by varying the magnitude of the initial stretch in the infarct elements. Three levels of prescribed pre-stretch in the fiber direction were examined: 10%, 25%, and 50% (stretches of 1.1, 1.25, and 1.5, respectively).

The FEBio multigeneration material framework was used to change the material properties of the scar after compaction. The multigeneration material allows definition of multiple sub-materials, each active during user-defined, non-overlapping “generations.” The reference configuration of the mesh resets at the beginning of each generation, so the mesh geometry at the start of each generation is assumed to be the undeformed state. This framework allowed us to:

- 1) Generation 1: Simulate longitudinal compaction of the acute scar.
- 2) Generation 2: Reset the reference configuration of the entire mesh to the compacted scar geometry and re-define the infarct material coefficients to stiffen the scar.

Boundary conditions & loading

To prevent rigid body motion during loading, all nodes on the basal surface were constrained in three dimensions. To prevent expansion of the apical hole during pressurization and contraction, the ring of nodes at the apex in each transmural layer were constrained relative to each other. In each transmural layer, fixed distance constraints were used between every pair of nodes to prevent the area of the opening from changing. Passive inflation of the ventricle was simulated by applying a uniform, linearly increasing pressure to all elements on the endocardial surface. Changes in LV cavity volume during inflation were calculated in MATLAB using the coordinates of the endocardial nodes at each time step, allowing examination of the EDPVR. Simulation of active function required the use of an additional volume constraint to hold LV cavity volume constant during active contraction. This constraint preserved the volume bounded within the endocardial surface during contraction and output the cavity pressure required to balance the active stress. To map out the linear ESPVR, multiple simulations of isovolumic contraction were run from different starting points. To do so, the model was first passively inflated to a specified cavity pressure, isovolumic contraction was initiated, and the maximum cavity pressure generated to balance contraction and maintain a constant cavity volume was recorded. The maximum pressure value was plotted against the cavity volume (of the isovolumic phase) of each model, and a linear fit to these data points yielded the ESPVR. Since transition between passive cavity inflation and isovolumic contraction required temporal control over the activation of the volumetric constraint, a multi-step analysis was required.

Results: Local deformation

Six distinct left ventricular models were examined: Baseline, Acute Infarct, Acute Patch, and three Chronic Patch models with varying degrees of scar compaction. The

magnitude of longitudinal compaction was controlled by prescribing a residual uniaxial tension to the undeformed reference geometry, resulting in compression when the model is allowed to come to equilibrium. We ran simulations using three different prescribed values of initial fiber stretch: 10%, 25%, and 50%. However, due to the nonlinear and fibrous nature of the infarct material, the magnitude of prescribed stretch did not equal the resulting magnitude of compression. The amount of longitudinal compression resulting from each value of initial stretch at an end-diastolic pressure of 12mmHg is shown in Figure 5.6A. In each case, the resulting longitudinal compaction (measured by averaging longitudinal strain in midwall elements in the center of the infarct) was less than half of the magnitude of the prescribed fiber stretch. Across all models, the degree of compaction increased with increasing pre-stretch, with the largest pre-stretch case (50%) producing the best match to our 8 week scar compaction data.

To determine whether compaction and stiffening of the scar was mechanically unloading patch tension, we examined longitudinal stresses in elements located in the center of the patch (Figure 5.6B). The acute patch model, in which the underlying scar is even softer than passive myocardium, exhibited tensile longitudinal stresses in the patch at end diastole, which increased even further in response to the high LV pressure at end systole. In all three scar compaction models, we observed a dramatic decline in longitudinal patch stress at both end diastole and end systole. The patch in the 10% pre-stretch model was still under tensile stress, although stresses at both time points were greatly reduced compared to the acute model. Longitudinal stress in the patch switched to compressive in both the 25% and 50% pre-stretch models, at both end diastole and end systole, indicating that the patch is no longer bearing any load during the cardiac cycle in either model.

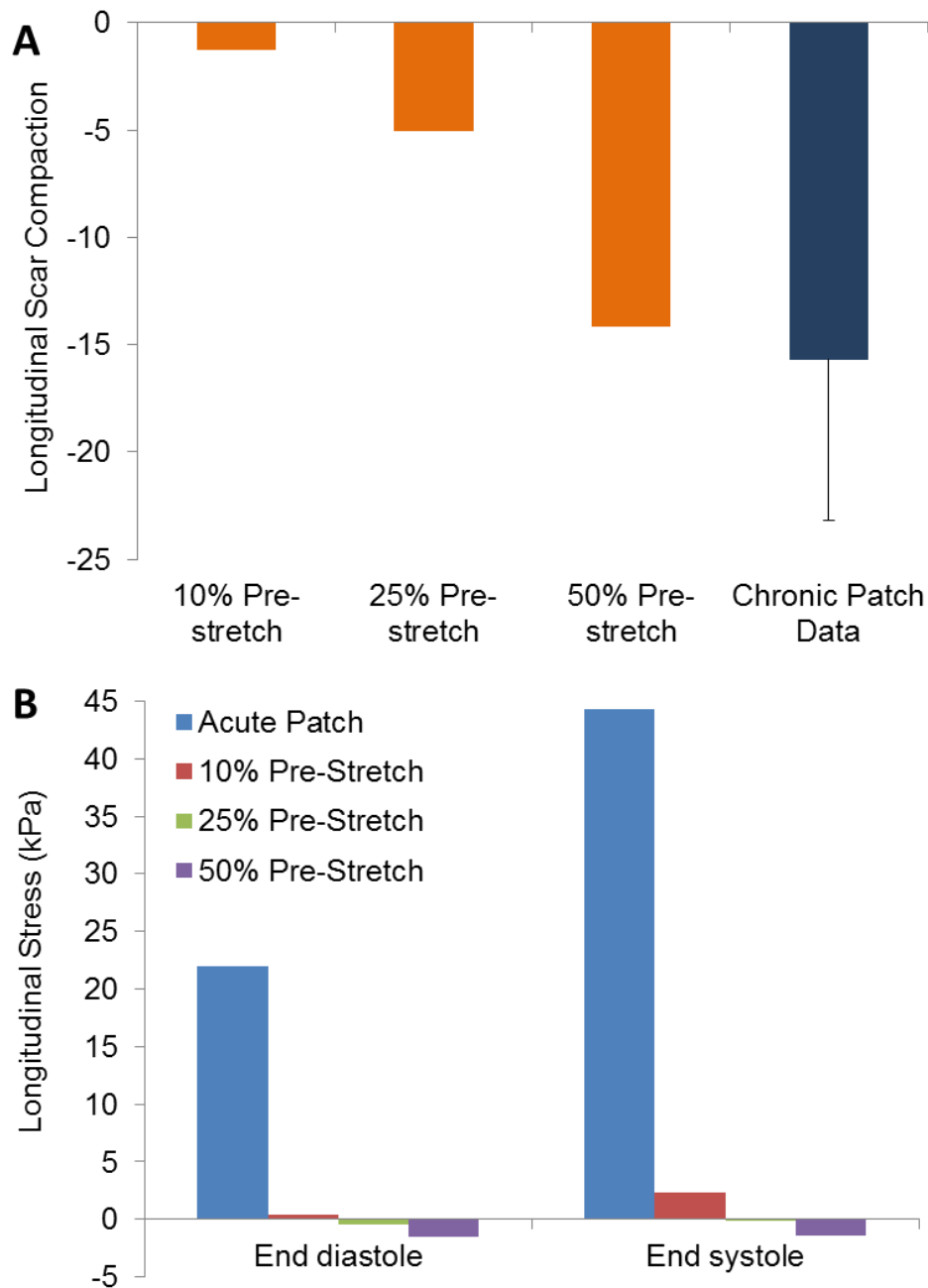


Figure 5.6 Simulation of scar compaction. (A) Variable levels of prescribed longitudinal pre-stretch in the infarct led to increasing amounts of infarct compression, evaluated at an EDP of 12mmHg. The 50% pre-stretch model was the closest match to our 8 week scar compaction data. (B) Longitudinal stresses at end diastole and end systole in the center of the patch were tensile in the presence of an acute infarct, tensile but greatly reduced in the 10% pre-stretch model, and compressive in both the 25% and 50% pre-stretch models.

Results: Global function

Pressure-volume behavior was used to validate model predictions of global function and compare function across simulations. In construction of the baseline model, the average pre-infarction pressure-volume curves from the acute canine study were used to tune material parameters for passive myocardium and active contraction (Figure 5.7A). Addition of the anterior infarct (which was isotropically softened to match infarct remodeling strain data, as described above) and longitudinally stiff epicardial patch (the stiffness of which was also selected to match infarct remodeling strains, as described above) also led to good agreement with the average experimental curves. Changes in stroke volume (interpolated from average P-V curves, between an EDP of 12mmHg and an ESP of 85 mmHg) across states were also captured well in the baseline and acute infarct models (Figure 5.7B). However, despite matching the measured remodeling strains, the model slightly underestimated the magnitude of the increase in stroke volume we observed with patch restraint in the acute experiment.

Comparison of our chronic models with the average experimental curves from the 8 week patch animals revealed large differences in cavity volume (Figure 5.8). The estimated unloaded cavity volume from our experimental curves was almost twice as much as the unloaded volumes predicted for any of the three chronic scar models. However, this poor agreement in absolute volumes was not surprising, since we did not include remodeling or dilation of the noninfarcted portion of the LV in our models. Apparent differences in the passive stiffness of the computational and experimental ventricles (as indicated by the slope of the EDPVR) can also be attributed to the dramatic difference in unloaded cavity size.

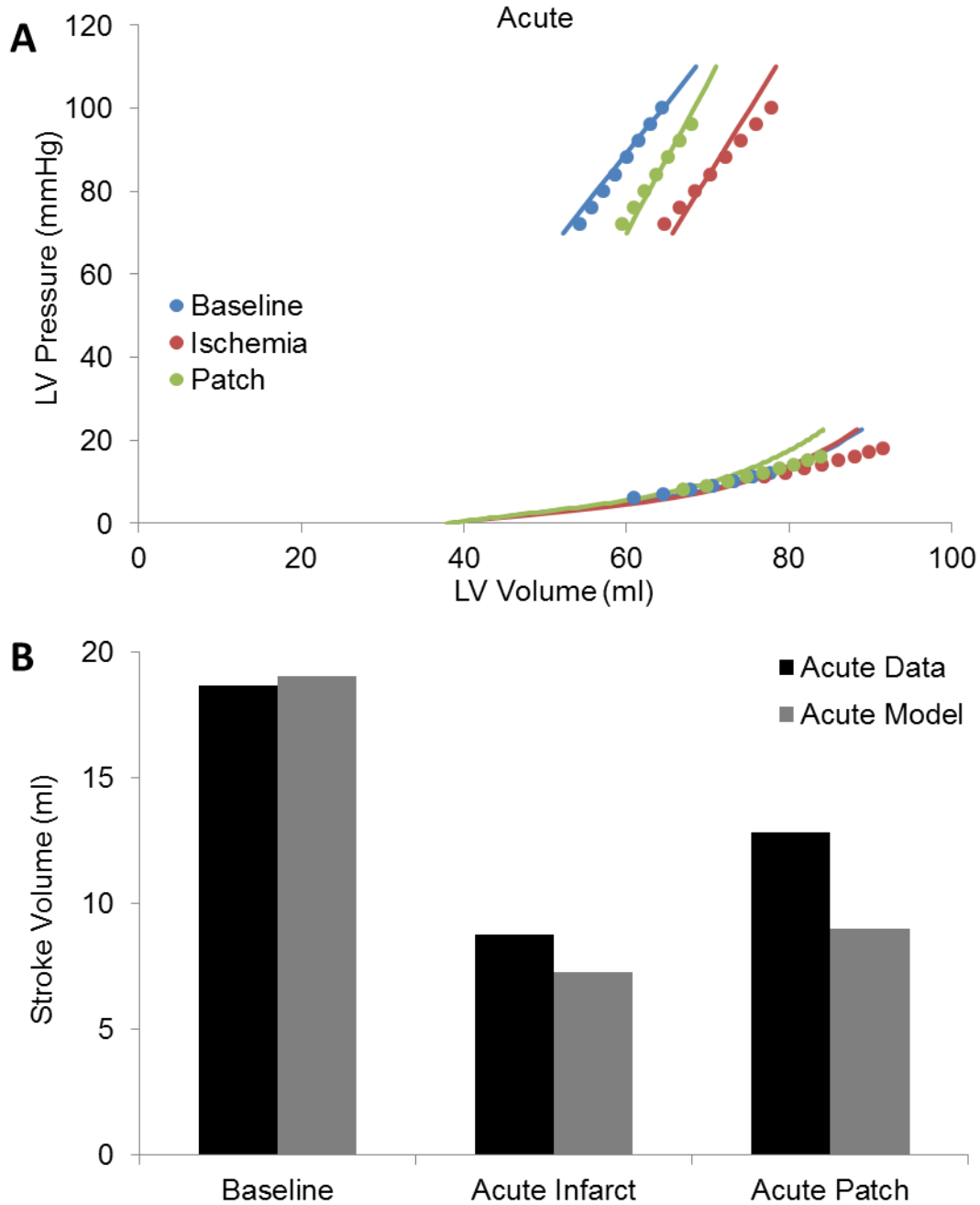


Figure 5.7 Acute function. (A) Average pressure-volume curves from the acute canine experiment (circles) compared to the model predictions (lines). (B) Comparison of experimental and computational stroke volumes, interpolated from average PV curves between EDP = 12mmHg and ESP = 85mmHg.

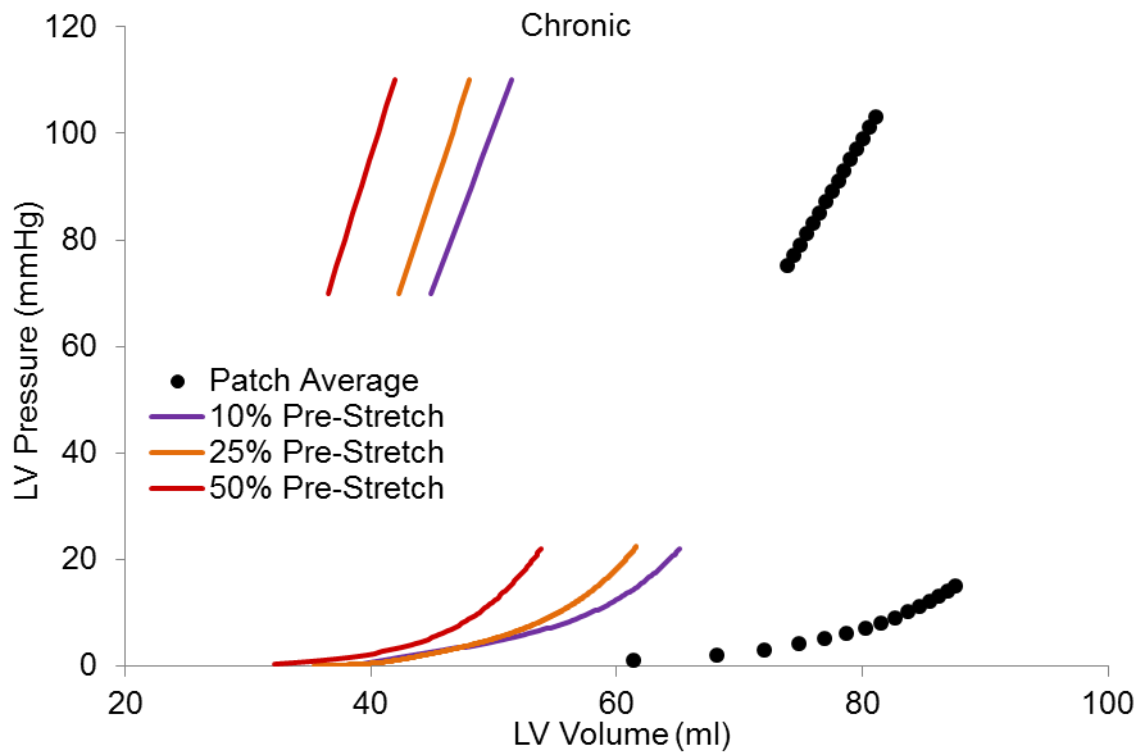


Figure 5.8 Chronic function. Average pressure-volume curves from the chronic canine experiment (circles) compared to the model predictions (lines). Since our chronic models simulated remodeling of the scar but not of the ventricle, all chronic predictions of global pressure-volume behavior substantially underestimated left ventricular cavity volumes.

Discussion

In this study, we developed a new finite element model of the canine left ventricle. We used MR images to construct a mesh that reflected the cardiac geometry of the dogs used in our studies. Unlike previous models, we did not assume that the acute infarct exhibited the same material properties as passive myocardium. Instead, we allowed transmural softening of the acute infarct to match our experimental data showing significant infarct expansion at matched EDP after 45 minutes of ischemia. We also incorporated in-plane compaction and stiffening of the infarct to simulate our experimental observations during infarct healing in our chronic reinforcement study. With these changes implemented simultaneously, this new model is capable of capturing key features of infarct remodeling throughout healing.

Due to the amount of scar compaction we observed in our chronic study, accompanied by a lack of improvement in LV function or remodeling, we hypothesized that longitudinal scar compaction may have negated the acute effects of our therapy by mechanically unloading the Dacron patch used to impose restraint. Using longitudinal stresses in the center of the patch as an indicator of the level of applied restraint at end diastole and end systole, we observed that even small amounts of scar compaction accompanied by scar stiffening were sufficient to completely unload the tension in the patch. In our intermediate compaction model, we observed that a 25% fiber pre-stretch led to approximately 5% longitudinal compaction in the center of the scar. However, this 5% compaction was sufficient to generate compressive longitudinal stresses in the patch at both end diastole and end systole. The average amount of scar compaction we observed in our experiment was more than three times greater, approximately 16% at 8 weeks post-MI. Therefore, if even small degrees of longitudinal compaction are capable of unloading the tension, it seems likely that our patch was mechanically unloaded

fairly early in the infarct healing process, potentially much sooner than our final, 8-week time point.

Conclusion

The current model generates accurate predictions of the global changes associated with acute ischemia and reinforcement. The model also incorporates both acute (acute infarct expansion) and chronic (compaction and stiffening) changes in the scar geometry and material properties during healing. This model allows for more comprehensive examination of the effects of restraint therapies, and the interplay between scar remodeling and therapy effectiveness. In the current example, incorporation of scar compaction and stiffening during healing predicted that the patch would be mechanically unloaded well before 8 weeks, which was consistent with our experimental observations. However, the current model is limited by the exclusion of post-MI cavity dilation, and the chronic predictions would greatly benefit from the inclusion of ventricular remodeling.

References

- Guccione, J. M., & McCulloch, A. D. (1993). Mechanics of active contraction in cardiac muscle: Part I- constitutive relations for fiber stress that describe deactivation. *Journal of Biomechanical Engineering*, *115*, 72–81.
- Guccione, J. M., Waldman, L. K., & McCulloch, A. D. (1993). Mechanics of active contraction in cardiac muscle: Part II- cylindrical models of the systolic left ventricle. *Journal of Biomechanical Engineering*, *115*, 82–90.
- Heiberg, E., Sjogren, J., Ugander, M., Carlsson, M., Engblom, H., & Arheden, H. (2010). Design and validation of Segment - a freely available software for cardiovascular image analysis. *BMC Medical Imaging*, *10*(1).
- Maas, S., Ellis, B., Ateshian, G., & Weiss, J. (2012). FEBio: finite elements for biomechanics. *Journal of Biomechanical Engineering*, *134*(1).
- May-Newman, K., Mathieu-Costello, O., Omens, J. H., Klumb, K., & McCulloch, A. D. (1995). Transmural distribution of capillary morphology as a function of coronary perfusion pressure in the resting canine heart. *Microvascular Research*, *50*, 381–396.
- Meier, G. D., Ziskin, M. C., Santamore, W. P., & Bove, A. A. (1980). Kinematics of the Beating Heart. *IEEE Transactions on Biomedical Engineering*.
- Streeter, D. D., Spotnitz, H. M., Patel, D. P., Ross, J., & Sonnenblick, E. H. (1969). Fiber Orientation in the Canine Left Ventricle during Diastole and Systole. *Circulation Research*, *24*(3), 339–347.

Chapter 6

Acute, Anisotropic Reinforcement for Acute Right Ventricular Failure

Acute failure of the right ventricle (RV) is a common complication of cardiac surgery, and is associated with in-hospital mortality rates as high as 70-75% (Haddad, Couture, Tousignant, & Denault, 2009). Significant improvement in acute, post-infarction left ventricular function with anisotropic reinforcement led us to explore the efficacy of selective restraint of the right ventricle in ameliorating acute RV failure. On the left side, a finite element model of the canine left ventricle was used to determine the optimum direction for mechanical infarct reinforcement. However, due to the complex geometry and mechanics of the RV, no finite element models of the RV have been sufficiently validated to allow examination of various restraint directions *in silico*. Therefore, isotropic restraint and two orthogonal directions (parallel and perpendicular to the RV outflow tract) of anisotropic RV restraint were examined experimentally in an acute model of RV failure. A new strategy was developed to apply multiple types of

patch reinforcement to the epicardial surface, allowing us to examine all three patch configurations sequentially without having to remove and re-suture the patch. Right ventricular pressure, cardiac output, and acute changes in regional deformation on the anterior wall of the RV were used to compare the effects of each reinforcement type.

Right ventricular failure

Acute right ventricular failure (RVF) is a relatively common complication of complex cardiac surgery. Up to 20% of early complications and deaths in heart transplant patients can be attributed to acute failure of the RV, and up to 30% of patients undergoing implantation of a left ventricular assist device (LVAD) will develop RVF (Haddad et al., 2009). Although the majority of therapies focus on treating failure in the left ventricle, simultaneous failure of the right side dramatically increases mortality. In the population of patients with hemodynamic instability following any type of cardiac surgery, the mortality rate in patients with LV failure is 30-40% but jumps as high as 86% in patients with biventricular failure (Reichert et al., 1992).

Currently, there are limited medical and surgical treatment options for patients with RVF. Post-operative support includes administering inotropes and/or pulmonary vasodilators, minimizing intravenous fluid administration, and ensuring adequate ventilation and oxygenation. If medical therapy is unsuccessful, mechanical circulatory support is the next therapeutic option. Unfortunately, right ventricular assist device (RVAD) implantation is maximally invasive, is associated with mortality rates as high as 45% ((Chen et al., 1996), and is considered a temporary or last resort treatment. In one study, only 10 of 30 patients who underwent RVAD implantation for isolated RV failure following cardiac surgery survived to discharge (Moazami et al., 2004).

One group has studied the effects of selective restraint of the right ventricle as a treatment for RVF (Cevasco et al., 2014). Ischemic failure was induced in sheep by right coronary artery ligation and the effects of restraint were studied 8 weeks later using a fluid-filled balloon placed around the epicardium of the RV. Three increasing levels of restraint (balloon inflation pressure) were evaluated, but no differences in RV EDV, ESV, EF or diastolic compliance were observed between baseline and any restraint level. However, the authors did observe trends suggesting a trade-off between improvement in active function and interference with passive function, similar to studies of isotropic restraint of the LV. Therefore, we hypothesized that acute, anisotropic restraint might also hold promise for improving function in the ischemic right ventricle.

Methods for generating right ventricular failure

A porcine model of acute, ischemic failure of the right ventricle was chosen for this study. Adult swine of either sex were anesthetized with a 1ml/kg/hr infusion of propofol. Animals were intubated and ventilated with room air, with the addition of a positive end expiratory pressure valve as needed to maintain pO_2 . Arterial pressure was monitored by a catheter inserted into the femoral artery. The chest was opened and heart exposed via a midline sternotomy. The RCA and marginal branches were dissected free and vessel loops were placed around large branches to facilitate temporary occlusion. A Millar pressure catheter was inserted into the RV through a small hole in the right atrium (RA), a fluid-filled pressure line left in the RA to measure atrial pressure, and an ultrasonic flow probe placed around the pulmonary artery to measure RV stroke volume. Six sonomicrometer crystals were placed in the anterior wall of the LV, in the anticipated area of ischemia. The crystals were implanted in an angled, 3 row by 2 column grid, oriented so that adjacent crystal pairs were either parallel or perpendicular to the RV outflow tract (RVOT). Umbilical tape was passed

under the inferior vena cava (IVC) and through a hollow tube and was used to generate transient reductions in RV preload through temporary IVC occlusions. Baseline recordings of RV pressure, pulmonary flow, and segment lengths were saved once all instrumentation was in place and prior to any ischemia. An example of an instrumented porcine RV from this study is shown in Figure 6.1.

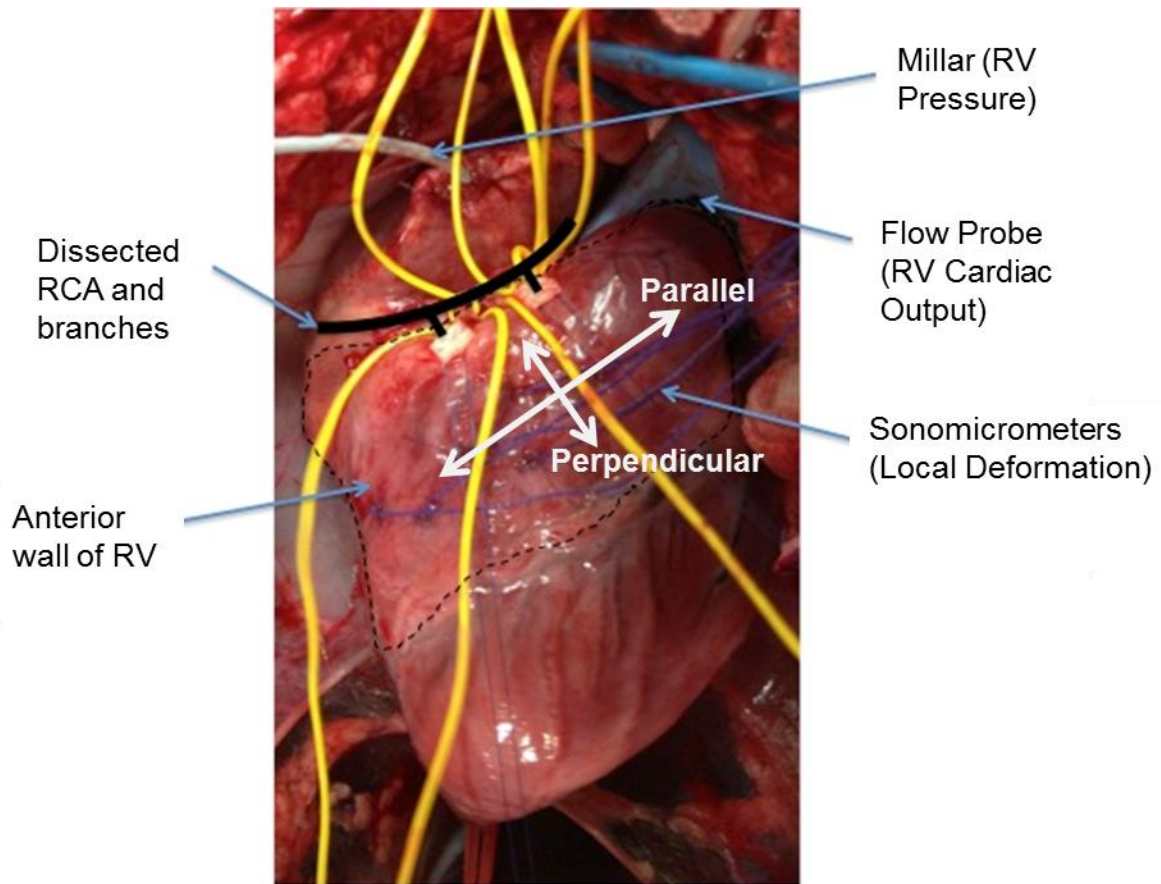


Figure 6.1 Porcine right ventricle instrumented for acute reinforcement study.

We initially pursued a microembolization model of acute RVF, as described by Nordhaug et al.(Nordhaug, Steensrud, Muller, Husnes, & Myrmel, 2004) A suspension of 50 μ m diameter polystyrene microspheres (Phosphorex, Hopkinton, MA) in a solution of saline with 0.01% Tween 80 was injected into the RCA either directly or via a cannula. In three pilot animals, three different combinations of microsphere concentration and volume were tested:

- 1) 5ml (2.5ml injection x 2 doses) of 4mg/ml solution \rightarrow 20mg microspheres
- 2) 8ml (2ml injection x 4 doses) of 2.5mg/ml solution \rightarrow 20mg microspheres
- 3) 20ml (2ml injection x 10 doses) of 2.5mg/ml solution \rightarrow 50mg microspheres

Although Nordhaug reports that microspheres were injected into the RCA until a 35% decrease in RV cardiac output was observed, we did not observe any changes in RV CO during any of our experiments. In one animal, histology of the RV myocardium in the area supplied by the RCA was performed and revealed a surprising lack of microspheres. These pilot studies suggested that we would not be able to use this model to generate sufficient dysfunction to see improvement with reinforcement later on, so the embolization model was abandoned and a ligation model similar to that reported by Spalding et al. was pursued instead.(Spalding, Ala-Kokko, Kiviluoma, Alahuhta, & Juvonen, 2001)

During each study, the amount of RV ischemia was evaluated visually based on changes in myocardial color and development of regional dyssynchrony. The aim was to generate the maximum tolerable amount of RV dysfunction in each animal, despite considerable variation in RCA branch anatomy. In every animal, the contribution of each marginal RCA branch was determined by individual, 5 minute occlusions of each branch. Combinations of branches were then tested to estimate the size of the

anticipated ischemic area, and selected branches were permanently ligated. Following ligation of all selected branches, ischemia was allowed to develop for 10-15 minutes. Antiarrhythmic drugs, inotropic agents, and defibrillation were used as needed. Each data set collected included several (at least five) normal beats for evaluation of segment lengths and current hemodynamic state, followed by an IVC occlusion to evaluate function across a range of filling pressures.

Patch reinforcement began immediately after collection of ischemic data runs. The patch used in these studies was identical to the patch used in all LV reinforcement studies, except that in the current study no slits were cut in the patch so that it remained mechanically isotropic. The patch was attached to the RV epicardium with a separate running stitch along each of the four edges and oriented so that the longer edge of the patch was parallel to the RVOT (orientations parallel and perpendicular to the RVOT are marked with white arrows in Figure 6.1). The free ends of each length of suture were passed through one of two pieces of rubber tubing at opposite corners of the patch (Figure 6.2). This system allowed selective loosening and tightening of individual edges of the patch to test various reinforcement configurations without having to remove the patch from the epicardial surface. Three restraint configurations were tested: anisotropic restraint parallel to the RVOT, anisotropic restraint perpendicular to the RVOT, and isotropic restraint. In each animal, at least two non-consecutive sets of data were collected for each patch configuration, separated by “patch off” runs in which all edges were loosened to effectively remove reinforcement without removing the patch. Animals were euthanized with an overdose of sodium pentobarbital upon completion of data collection.

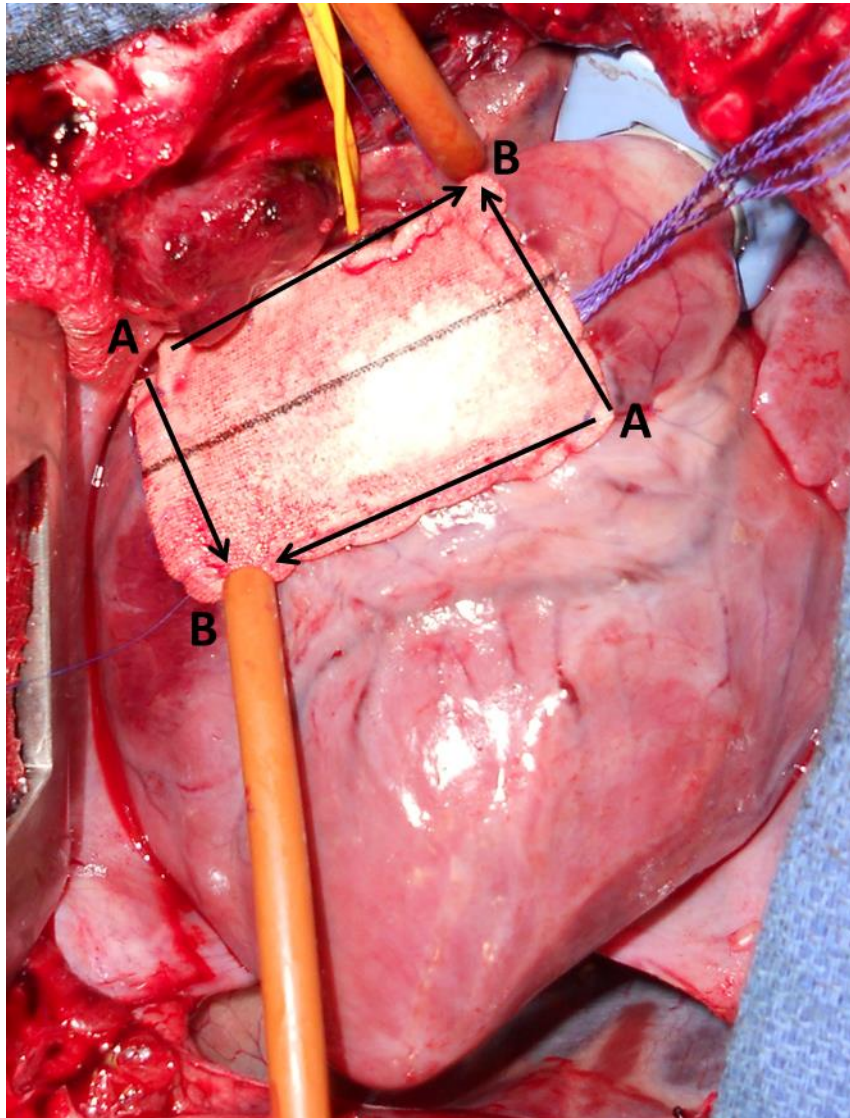


Figure 6.2 Patch attached to RV epicardium. Four suture lengths (marked with black arrows) were tied at opposite corners of the patch (marked “A”), and a running stitch was placed along each edge. At the other two opposite corners (marked “B”), the free ends of each suture were passed through a small length of flexible tubing. Hemostats were used to clamp down on the suture within the tubing after selective loosening or tightening of each edge, allowing us to test all three reinforcement strategies without removing the patch from the epicardium.

Methods for data analysis

The methods used to analyze all hemodynamic and sonometric data in this study were similar to those used in the analysis of the acute LV reinforcement data in Chapter 2. Briefly, data traces were filtered to remove noise and exported from SonoSoft to be analyzed in Matlab. RV pressure-segment length loops were used to evaluate changes in regional deformation between baseline, ischemia, and patch reinforcement runs. RV function curves were generated by plotting SV or CO v. EDP during each occlusion, and function was compared across runs by interpolating SV at a matched value of EDP (from linear fits of each function curve).

Changes in stroke volume and maximum segment length were averaged across animals. Differences in the percent change in stroke volume relative to baseline between ischemic states (Ischemia, Parallel Patch, Isotropic Patch, Perpendicular Patch, Patch Off) were compared using ANOVA. The percent change in maximum length of each segment (relative to baseline) was also analyzed by ANOVA. For both stroke volume and segment lengths, comparisons between baseline and ischemia were made by calculating the average percent change in each parameter (referenced to baseline value) and using a two-tailed, one-sample t-test against a hypothetical mean of zero. A cutoff value of $p=0.05$ was used for all tests, and Newman-Keuls post-hoc tests were used to make pairwise comparisons between groups when the ANOVA indicated significance.

Results: Local deformation

Data from a preliminary group of six animals were analyzed for inclusion in this chapter. In some animals, the reduction in stroke volume was accompanied by a shift in the pressure-segment length behavior from an actively contracting loop (at baseline)

to a passively stretching exponential (during ischemia), reminiscent of the local changes observed in the acute LV infarcts (Figure 6.3A). However, in other segment or animals, the change in pressure-segment length behavior was characterized by a narrowing of the loop without complete elimination of the active contractile behavior (Figure 6.3B).

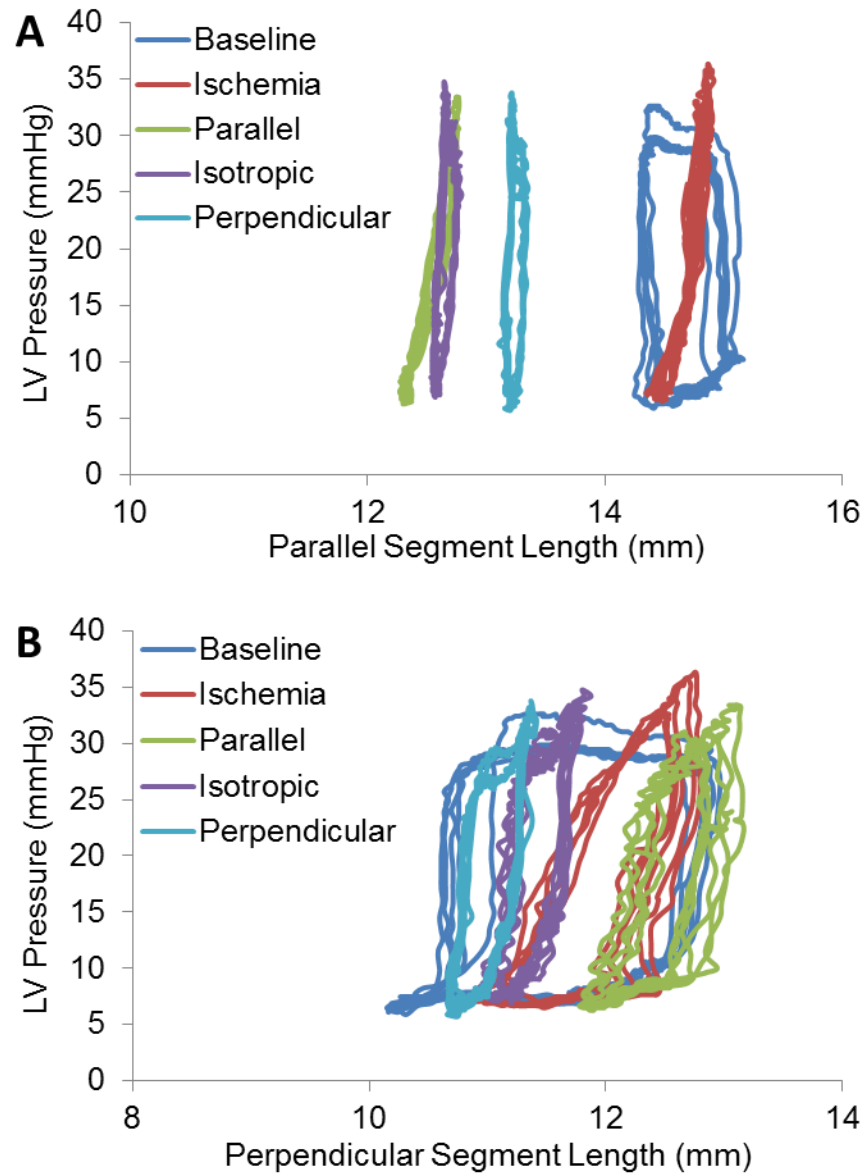


Figure 6.3 Example pressure-segment length plots for a single animal (RV11), showing changes in the lengths of a segment (A) parallel and (B) perpendicular to the RV outflow tract.

To quantify the effects of each patch configuration on local deformation, we compared changes in maximum segment lengths across states (Figure 6.4). Segments oriented parallel and perpendicularly to the RVOT (and the direction of reinforcement) were selected, and percent change from baseline in the maximum length of each segment was averaged across animals. With parallel reinforcement, we observed an average $-7.5 \pm 7.4\%$ decrease in parallel segment length, with a $-2.6 \pm 2.8\%$ decrease in the perpendicular direction. The change in parallel segment length was similar with isotropic reinforcement ($-7.7 \pm 8.1\%$), accompanied by increased restraint of the perpendicular segment ($-9.4 \pm 2.6\%$). Perpendicular reinforcement led to larger decreases in maximum perpendicular segment length ($-9.6 \pm 3.0\%$) than parallel segment length ($-5.1 \pm 7.0\%$), although the difference between the two directions was smaller than observed in the parallel patch condition. However, due to the small sample size ($n=6$) and substantial variability between animals, only the changes in perpendicular segment length due to the isotropic and perpendicular patches were significant.

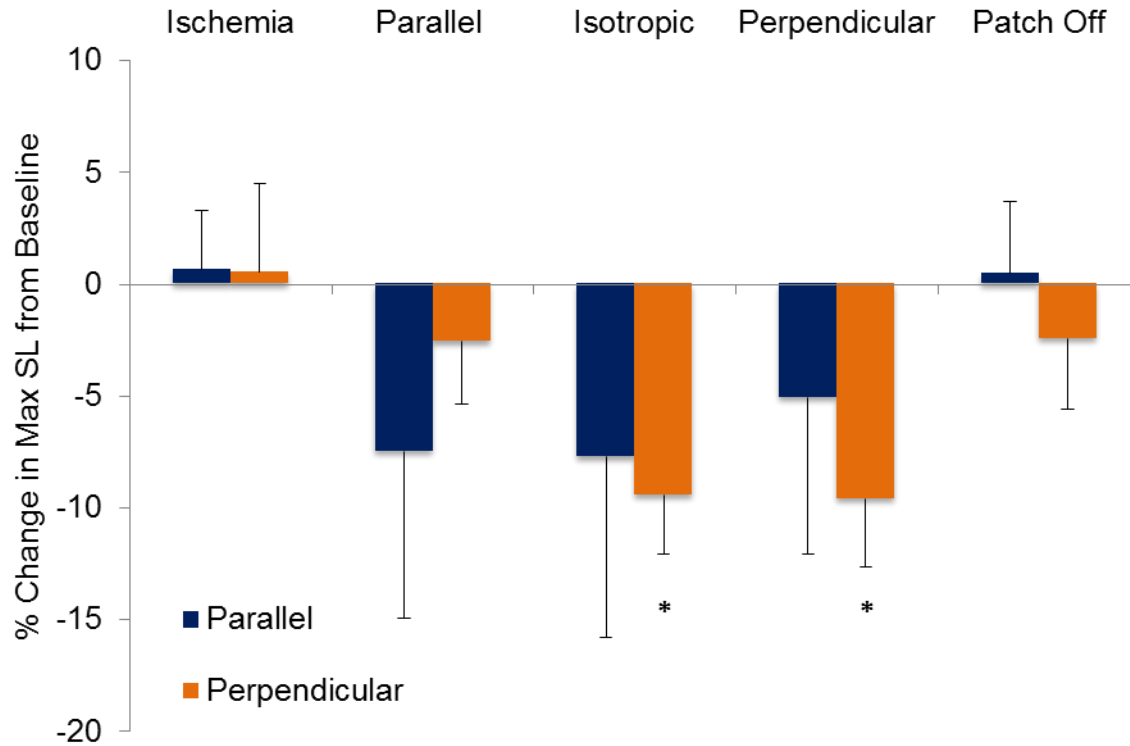


Figure 6.4 Average percent change in maximum segment lengths across states, relative to baseline. No significant changes were seen in the parallel segment, regardless of patch configuration, although changes in trends in this segment across states were as expected. Both isotropic and perpendicular reinforcement led to a significant reduction in the maximum perpendicular segment length. * $p < 0.01$ compared to ischemia.

Results: Global function

We quantified changes in right ventricular function by interpolating changes in stroke volume at a matched value of end-diastolic pressure (Figure 6.5). To minimize extrapolation when computing stroke volume at matched value of RV EDP, each animals' own EDP at baseline was chosen as the pressure value for interpolation of SV across states. Following ligation of branches of the right coronary artery, we observed a significant reduction in stroke volume between baseline and ischemia, from an average of 107.2ml to 76.4ml (-28.7 +/- 12.7%), respectively. None of the three patch reinforcement configurations (parallel to RVOT, isotropic, and perpendicular to RVOT) produced a significant change in stroke volume compared to ischemia, although we did observe an average trend toward worse SV with reinforcement, regardless of patch type. Removing the patch at the end of the study led to a shift toward an average SV similar to the ischemic value, suggesting that the changes in function observed with reinforcement were reversible and due to our mechanical interventions rather than deteriorating RV function during the course of the study.

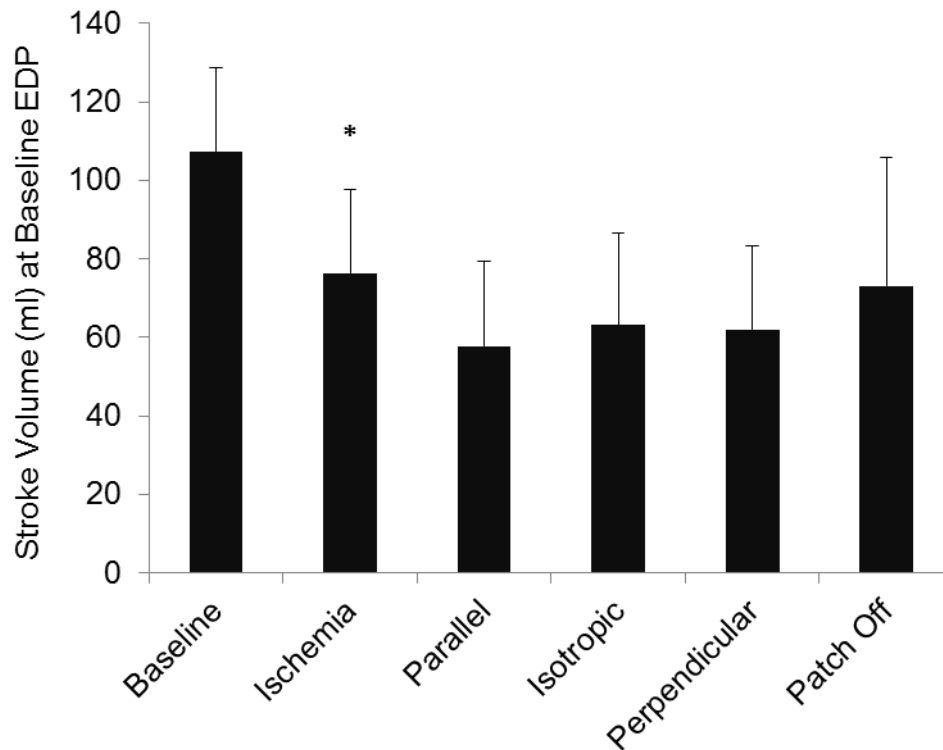


Figure 6.5 Stroke volume interpolated at the baseline EDP of each pig and averaged across animals. We observed a significant decrease in stroke volume between the baseline and ischemic states, although there were no significant differences between ischemia and any of the patch conditions. * $p < 0.01$ compared to baseline.

Discussion

In this study, we evaluated three types of mechanical restraint to determine their ability to improve function in acute right ventricular failure. In the preliminary group of six animals analyzed here, changes in local deformation with patch application generally confirmed imposition of the intended reinforcement, although some changes were not yet statistically significant at this sample size. Trends toward decreased parallel segment lengths were observed following isotropic and parallel reinforcement, while significant reductions in the perpendicular segment length were observed following isotropic and perpendicular patch reinforcement. We observed a significant decrease in RV stroke volume following ligation of RCA branches. However, none of the three patch configurations produced any significant changes in SV relative to ischemia, and trends in the average SV values actually suggested a slight decrease in SV with any type or reinforcement. Average stroke volume shifted back toward the ischemic value in the final "Patch Off" state, suggesting that changes in SV during each patch condition were not due to functional deterioration of the RV during the course of the open-chest study. Although this small group of animals only represents a fraction of the experiments conducted to date (6 out of 21), the preliminary data analyzed here suggest that none of the mechanical restraint approaches tested (isotropic, parallel to RVOT, perpendicular to RVOT) can produce significant improvements in acute RV function.

References

- Cevasco, M., Kwon, M., Fiedler, A., Lee, L. S., Shiao, J., Shah, R. V., ... Chen, F. Y. (2014). Right heart failure: An ischemic model and restraint therapy for treatment. *Annals of Thoracic Surgery*, 97(4), 1356–1362.
- Chen, J. M., Levin, H. R., Rose, E. a., Addonizio, L. J., Landry, D. W., Sestino, J. J., ... Oz, M. C. (1996). Experience with right ventricular assist devices for perioperative right-sided circulatory failure. *Annals of Thoracic Surgery*, 61(1), 305–310.
- Haddad, F., Couture, P., Tousignant, C., & Denault, A. Y. (2009). The right ventricle in cardiac surgery, a perioperative perspective: Ii. pathophysiology, clinical importance, and management. *Anesthesia and Analgesia*, 108(2), 423–433.
- Moazami, N., Pasque, M. K., Moon, M. R., Herren, R. L., Bailey, M. S., Lawton, J. S., & Damiano, R. J. (2004). Mechanical support for isolated right ventricular failure in patients after cardiectomy. *Journal of Heart and Lung Transplantation*, 23(12), 1371–1375.
- Nordhaug, D., Steensrud, T., Muller, S., Husnes, K. V., & Myrmet, T. (2004). Intraaortic balloon pumping improves hemodynamics and right ventricular efficiency in acute ischemic right ventricular failure. *The Annals of Thoracic Surgery*, 78(4), 1426–32.
- Reichert, C. L. A., Visser, C. A., Van den Brink, R. B. A., Koolen, J. J., Van Wezel, H. B., Mouljn, A. C., & Dunning, A. J. (1992). Prognostic value of biventricular function in hypotensive patients after cardiac surgery as assessed by transesophageal echocardiography. *Journal of Cardiothoracic and Vascular Anesthesia*, 6(4), 429–432.
- Spalding, M. B., Ala-Kokko, T. I., Kiviluoma, K., Alahuhta, S., & Juvonen, T. (2001). Inhaled nitric oxide effectively decreases right heart afterload following right heart infarct in pigs. *Scandinavian Cardiovascular Journal : SCJ*, 35(1), 45–9.

Chapter 7

Implications & Future Directions

Summary of main contributions

In this dissertation, anisotropic reinforcement was evaluated as a therapy to improve function and limit dilation following left ventricular infarction. We showed that local, longitudinal reinforcement of large, acute anterior infarcts dramatically improved post-MI left ventricular function. This was a novel finding, because multiple studies of various isotropic infarct reinforcement approaches have failed to show functional improvement with restraint. We pursued longitudinal reinforcement in a study of chronic infarct reinforcement, and were surprised to find no differences in chronic ventricular function or remodeling. We attributed the lack of benefit to mechanical unloading of our restraint therapy by substantial scar compaction, despite the common perception that infarcts expand. A new finite element model of the left ventricle was constructed to simulate the chronic effects of infarct restraint. The model incorporated the effects of infarct scar remodeling on restraint tension, and confirmed that scar

compaction was mechanically unloading the patch. This new model can be used for *in silico* evaluation of both the acute and chronic effects of any number of mechanical post-MI therapies. In a separate series of finite element models, we also explored the effects of sample heterogeneity on biaxially measured infarct material properties. Across several models of different scar size and distribution, we concluded that errors in stress and strain were minimal as long as a subset of markers (used to quantify specimen deformation) was located in a single island of scar comprising at least 10% of the sample volume. Overall, this work has provided new insight into the factors that determine the effectiveness of postinfarction mechanical restraint, as well as new models that can be useful in designing future therapies for myocardial infarction.

Interplay between scar compaction and restraint efficacy

After observing the substantial improvement in acute post-MI function with longitudinal infarct reinforcement, we hypothesized that the same restraint approach would also lead to improved chronic function and diminished left ventricular cavity dilation after several weeks of healing. However, we were surprised to observe no differences in LV function or volumes at 8 weeks post-MI. In conjunction, we observed dramatic scar compaction in both patch and control groups, with scars compacting to less than half of their 48hr volume over the course of the study. These results were also surprising, because the infarct healing literature typically focuses on infarct expansion – circumferential and longitudinal dilation plus radial thinning – rather than scar compaction. However, a recent review of studies that actually reported infarct dimensions suggests that expansion and compaction occur with similar frequency (Richardson & Holmes, 2013). Accordingly, different therapeutic approaches may have very different efficacy in different animal models or even in different patients. We would expect surgical restraint – as in our study – to be most effective for infarcts that

would normally expand if untreated. This might explain why studies that applied isotropic patches locally to prevent infarct expansion have produced more variable effects on LV remodeling than those that employed global restraint with cardiac support devices (Clarke, Ghanta, Ailawadi, & Holmes, 2014).

The finite element modeling results presented in Chapter 5 of this dissertation suggest that the lack of benefit observed in our chronic reinforcement study can be attributed to mechanical unloading of patch tension by scar compaction. If true, this hypothesis suggests that there is additional benefit to be derived from preserving longitudinal tension on the infarct throughout healing. This could be tested using dynamic restraint approaches, which can be adjusted to maintain constant tension on the scar as it remodels. Although local, adjustable restraint approaches have been used before to generate improvements in LV remodeling (Ghanta et al., 2008; Lee et al., 2012), previous studies have only explored isotropic approaches. Therefore, we hypothesize that adjustable, anisotropic restraint may limit LV dilation and also generate greater improvement in LV function than adjustable, isotropic therapies. Alternatively, static restraint could be explored in subpopulations or animal models exhibiting infarct expansion, where restraint will presumably confer the greatest benefit. However, effective clinical use of this strategy will require elucidation of the factors underlying infarct remodeling, in order to accurately predict whether a scar will compact or expand when selecting patients for restraint therapy.

Effect of mechanical environment on scar remodeling

Our finite element models and acute reinforcement experimental results emphasize the importance of infarct scar material properties in determining post-MI ventricular function. In addition, previous work in our lab has investigated the importance of

infarct mechanics in dictating the structure of the collagenous scar that forms. Across several animal models, patterns of stretch in the healing infarct correlated with the resulting scar structure, suggesting that mechanical guidance of scar formation is a key cue in dictating collagen organization. Therefore, we hypothesized that altering the stretch pattern in the acute infarct through longitudinal reinforcement would produce significant changes in either the amount, degree of alignment, or direction of alignment of collagen fibers constituting the scar. However, we were unable to detect any differences in transmural scar structure between reinforced and unreinforced scars after 8 weeks of healing. The similarity in final collagen structure can be used to generate several hypotheses to further elucidate the relationship between infarct mechanics and scar formation. One potential explanation for the lack of difference in scar structure is that fibroblasts are responding to a systolic stretch cue (difference in infarct dimensions between end diastole and end systole). In our acute reinforcement experiment, the primary reinforcement effects of the patch were measured as changes in remodeling strain (differences in infarct dimensions at end diastole), while longitudinal systolic strains were similar across the ischemic and patch states. Therefore, fibroblasts responding to changes in systolic strain would be unable to detect the differences in infarct mechanics imposed by our patch. This hypothesis could be tested by conducting another experiment in which the restraint imposes a significant change in longitudinal systolic strain without affecting the remodeling strain (e.g. not applied under longitudinal tension). However, this hypothesis is not supported by preliminary data from our lab, in which differences in infarct collagen volume were observed between reinforced and unreinforced rats at 6 weeks post-MI, as well as data from another study reporting reduced collagen content and organization in hemodynamically unloaded rat hearts (Zhou et al., 2011).

An alternative hypothesis is that there may have been differences in scar structure between the two groups at early time points, but that scar remodeling in both groups dominated scar formation at later time points and made any previous differences undetectable by 8 weeks. Our canine experimental scar compaction data and finite element simulation of reinforcement suggested that mechanical unloading of the patch had occurred substantially earlier than our final time point. An experimental time course of early post-MI infarct scar formation in both reinforced and unreinforced scars could be generated to examine the effects of restraint on scar formation. With more frequent measurements of collagen content and alignment, we hypothesize that there will be significant differences in the structures of reinforced and unreinforced scars at time points earlier than 8 weeks.

Finite element simulation of infarct remodeling

In Chapter 5, a new finite element model was constructed to allow simulation of acute and chronic infarct remodeling and predict the effects of mechanical post-MI therapies. There are several avenues for improvements to the current model, including simulating evolution of scar material properties during healing, inclusion of ventricular cavity remodeling, and employing alternate approaches to model scar compaction. In the current iteration, scar compaction is generated by prescribing a residual strain field in the infarct region. A pre-stretch is defined in infarct elements in the reference (undeformed) configuration, which leads to recoil and compression of those elements when the model is allowed to equilibrate. However, this approach was pursued as the most computationally convenient, and is likely not a physiologic representation of *in vivo* scar compaction. Although the exact processes governing scar remodeling remain to be elucidated, a reduction in infarct tissue volume due to large, necrotic myocytes being replaced by smaller collagen fibers may be a contributing factor. However,

implementing a volumetric loss approach in the model led to prediction of exclusive radial infarct thinning, with no compaction in the in-plane dimensions. Therefore, we hypothesize that active contractile forces of cells (fibroblasts) within the infarct may also play a role, and that a combination of both factors may be required to more accurately represent physiological scar compaction.

Despite these limitations, the current left ventricular model can be used to generate powerful predictions regarding the efficacy of the current restraint approach or any number of future iterations. From our chronic study results, we hypothesize that the lack of improvement in LV function or remodeling is due to mechanical unloading of the patch by scar compaction. This hypothesis could be easily tested using the model by simulating varying time points of restraint application. It is possible that applying the restraint at later time points (after significant compaction has already taken place) will result in chronic improvement, but it is also possible that applying the patch to a mature scar will have minimal effect because the scar is already extremely stiff. In a similar way, the model could be used to examine the effects of dynamic restraint devices, which could be implanted acutely post-MI and then adjusted to maintain tension on the infarct throughout healing.

Multiscale modeling of infarct healing

In addition to the utility of the LV finite element model in isolation, there is significant potential for model coupling to enhance the predictive power of the simulations. Firstly, coupling the FEM to a myocardial growth model to simulate changes in left ventricular remodeling will be critical in generating reliable predictions of the chronic effects of post-MI therapies. In addition, the FEM could be coupled to a circuit model of the circulation to generate more realistic, time-varying loading conditions and generate

full pressure-volume loops. Inclusion of an electrophysiology model would also allow prediction of how the infarct scar interferes with cardiac conduction pathways and optimization of potential combined mechanical and resynchronization therapies. On the cellular scale, coupling to an agent-based model of scar formation would allow feedback between pharmacologic interventions, infarct mechanics and resulting scar structure. Since pharmacologic therapy is the current standard of care to prevent post-MI dilated heart failure, coupling to cellular models that incorporate relevant signaling pathways would allow evaluation of the biological responses (inflammatory, metabolic) to implanted therapies, as well as examination of combined mechanical and pharmacologic therapies (such as a drug-eluting patch). Taken together, this multiscale model could be used to examine the effects of a post-MI therapy on inflammation, acute function, infarct mechanics, contractile dyssynchrony, scar formation and remodeling, and left ventricular remodeling. Such a model could be used to examine the acute and chronic effects of any number of static or dynamic mechanical restraint therapies, as well as combined (mechanical and pharmacologic, mechanical and electrical) therapies. This multiscale model simulating healing in the infarcted heart would be a critical tool for optimizing post-MI interventions and improving patient prognoses.

References

- Clarke, S. A., Ghanta, R. K., Ailawadi, G., & Holmes, J. W. (2014). Cardiac Restraint & Support Following Myocardial Infarction. In T. Franz (Ed.), *Cardiovascular and Cardiac Therapeutic Devices* (pp. 169–206). Springer Berlin Heidelberg.
- Ghanta, R. K., Lee, L. S., Umakanthan, R., Laurence, R. G., Fox, J. a, Bolman, R. M., ... Chen, F. Y. (2008). Real-time adjustment of ventricular restraint therapy in heart failure. *European Journal of Cardio-Thoracic Surgery : Official Journal of the European Association for Cardio-Thoracic Surgery*, 34(6), 1136–40.
- Lee, L. S., Ghanta, R. K., Mokashi, S. A., Coelho-Filho, O., Kwong, R. Y., Kwon, M., ... Chen, F. Y. (2012). Optimized ventricular restraint therapy: adjustable restraint is superior to standard restraint in an ovine model of ischemic cardiomyopathy. *The Journal of Thoracic and Cardiovascular Surgery*, 145(3), 824–31.
- Richardson, W. J., & Holmes, J. W. (2013). Do infarcts really expand or compact? Relationship between changing material properties and apparent infarct remodeling. *Presented at the ASME 2013 Summer Bioengineering Conference, June 26-29, 2013, Sunriver, Oregon.*
- Zhou, X., Yun, J., Han, Z., Gao, F., Li, H., Jiang, T., & Li, Y. (2011). Postinfarction healing dynamics in the mechanically unloaded rat left ventricle. *American Journal of Physiology. Heart and Circulatory Physiology*, 300(March), H1863–H1874.